University of Naples
"Federico II"

Polytechnic and basic sciences school
Educational area of mathematical,
physical and natural sciences

Physics Department

PhD in Physics, 32th cycle

Dark matter search: the Neutron Veto in the XENONnT Detector Upgrade

Advisor:
Prof. Michele Iacovacci

Candidate:
Bruno Cimmino

ACCADEMIC YEAR 2019-2020

Contents

Introduction

In the first decades of the last century it was understood that only a small part of our Universe consists of ordinary matter, or luminous and baryonic matter. Instead, most of it is composed of dark matter, or a type of matter that does not emit electromagnetic radiation and interacts with ordinary matter only gravitationally and possibly by means of weak interactions. The remaining part of the energy content of the Universe is named dark energy whose origin is still unknown. The possibility of dark matter existence was inferred by some experimental evidences, such as stars' rotation speeds around the galaxies, gravitational lensing, the "bullet cluster", the anisotropies of the cosmic background radiation. Dark energy existence was hypothesized when, at the end of the last century, it was discovered that the expansion of the Universe is accelerated, and therefore there must be a force that opposes gravity which, in absence of other forces, slows down the expansion. The present most accredited model of the Universe is the so-called "Flat Λ_{CDM}". According to this model, the amount of ordinary matter is about 4%, the amount of dark matter is to about 23% while the remaining 69% consists of dark energy. The experiments planned for the coming years should give us more answers. Chapter 1 illustrates this overview and the possible candidates for dark matter according to Particle Physics. The most plausible candidates are massive particles having a week interaction with ordinary matter, apart from gravitation, and for this reason named WIMP (Weak Interacting Massive Particles).
There are three different techniques to detect WIMPs: the production of WIMPs through collision of ordinary matter in accelerators, direct detection through the observation of WIMPs-nuclei scattering and indirect detection through the observation of ordinary matter particles produced by WIMPs' annihilation. The most revelant problem for direct detection is that WIMP-nuclei scattering events are very rare (about one event per tons per year, cross section $\sigma < 10^{-44} cm^2$) and therefore, to increase the probability to detect WIMPs, it is necessary to use large-mass detectors, while to minimize background events it is necessary to place the detectors in laboratories located

underground or under the sea, and furthermore to use additional techniques. Chapter 2 shows an overview of the three detection technique, focusing in particular on direct detection.
Among all dark matter direct detection experiments, of particular importance are experiments that use noble gases as detection medium, in particular Xenon. Noble liquids have many advantages: they are pure, chemically inert and excellent insulators. Among the other features, Xenon is a perfect choice for dark matter search thanks to its high atomic mass and density, which makes it a very efficient medium to stop penetrating radiation, reduce external background and increase the elastic WIMP-nucleus scattering cross section. The XENON project consists in a dark matter direct detector located at the Gran Sasso National Laboratories (LNGS), below 1.4 km of rock, providing about 3600 meters of water equivalent shielding that reduces the muon flux by a factor 10^6 . The experiment is based on a dual-phase (Liquid/Gaseous) Xenon Time Projection Chamber (LXeTPC). It exploits both scintillation and ionization signals to calculate the recoiling energy released by an impinging particle scattering off liquid Xenon target and to discriminate nuclear from electron recoil background. The detection principle of a direct dark matter experiment using a dual-phase TPC filled with Xenon is presented in first part of Chapter 3.
The first detector of the XENON project, XENON10, filled with 15 kg of Xenon, published in 2008 the best limits at the time for a WIMP-nucleon elastic scattering. The subsequent detector XENON100, 161 kg of target mass, ran from 2008 to 2016 and set in 2012 the limit for spin-independent elastic WIMP-nucleon scattering, with a minimum cross section of $2.0 \cdot 10^{-45} cm^2$ for a WIMP mass of 55 GeV/c^2, at 90% confidence level (C.L.). The next upgrade, XENON1T, with 3.2 tons of target mass, has been in operation from 2016 to 2018, setting the best limit for spin-independent WIMP-nucleon elastic scattering to $4.1 \cdot 10^{-47} cm^2$ cross section for a $30 GeV/c^2$ WIMP mass at 90% C.L. The last upgrade is called XENONnT. Its construction began in 2019 and it will be operative by the end of 2020, probably in October. In this upgrade the detector has a target mass of $\sim 8 tons$, in order to improve the sensitivity to the spin-independent WIMP-nucleon elastic scattering cross sections down to $1.6 \cdot 10^{-48} cm^2$ in a 20 $t \cdot y$ exposure. This "evolution" of the XENON project is illustrated in the second part of Chapter 3.
Chapter 4 describes the XENONnT detector and contains a discussion of the background sources. There are three main sources of background in XENONnT experiment. External background is due to cosmic rays and other particles from space. It is reduced thanks to the location of the experiment below 1400 meters of rock. Internal background consists of the gamma rays coming from the structural elements and in general from all the surrounding

materials and those contained in the detectors. The effect of this background source is mitigated by means of an accurate selection of materials with a low content of natural radioisotopes. The second, the intrinsic background, comes from the elements of ^{222}Rn (Radon) decay chain, that are part of the ^{238}U decay chain. In this case control goes through the choice of materials with a low content of U/Ra and whit low Radon emanation that will help to reduce this source of background. The Nuclear Recoil (NR) background from radiogenic neutrons starts to become relevant for the final sensitivity of XENON experiment and, in particular, for its potential to discover WIMPs. In order to reduce this background, the Neutron Veto was designed, with a solution of Gadolinium dissolved into water. The structure of the Neutron Veto and its performance are described in detail in the last part of the chapter.
In Chapter 5 my analysis work is illustrated. After an overview on photomultipliers physics, the characteristic of the PMTs used for nVeto are described. I have contributed by studying the signal features of theese PMTs. In the last section are illustrated the results of this analysis.

Chapter 1

The Dark Universe

The existence of gravitation effects that are not due to ordinary matter and the observation of the acceleration of the Universe expansion respectively bring to the hypothesis that Dark Matter and Dark Energy exist. Looking at the the composition of the Universe, 68.5% of dark energy, 26.6% of dark matter and just from 4.9% of ordinary matter, we can conclude that it is almost completely unknown.
Investigation on the Universe composition becomes, then, one of the most fascinating challenge for modern Cosmology, and for science in general.

1.1 Dark Matter and Dark Energy: experimental evidences

In this section the experimental evidences which led to hypothesize the existence of dark matter and dark energy will be described [4].

1.1.1 Galaxy rotation curves

Rotation speed of stars and galaxies gives an estimation of the amount of matter contained in the Universe [7].
Let consider a spiral galaxy with a matter density $\rho(r)$, its mass:

$$M(r) = 4\pi \int_0^r \rho(r) r^2 dr \tag{1.1}$$

can be obtained, starting from the measurement of the rotation speed $v(r)$, by using the Virial theorem:

$$< \frac{GM(r)}{r^2} >=< \frac{v^2(r)}{r} > \tag{1.2}$$

$$< v(r) >= \left(\frac{GM(r)}{< r >} \right)^{1/2} \tag{1.3}$$

where G is the gravitational constant.
Rotation curves of a spiral galaxy were measured for the first time by Vera Rubin in the mid-1970 and represent the speed of the stars contained in the galaxy as a function of their distance from the center of the galaxy. They are obtained by using the Doppler effect. When the galaxy disk moves away from the observer a red-shifted spectrum is emitted while, when it moves toward the observer, the emitted spectrum is blue-shifted.
Figure 1.1 shows the rotation curve of the dwarf spiral galaxy NGC6503 [9]. From this curve it possible to see that the central part of the galaxy rotates as a rigid body, while far away from the center the rotation speed is constant. The galaxy mass, as it has been discovered, increases with the distance from the center and its density scales with r^{-2}.
This effect can be only explained if one supposes the existence of a non-ordinary matter, the dark matter.
Rotation curve also provide a measurement of the dark matter density. Being $\rho(r) \propto r^{-2}$ at high distances and $\rho(r) \propto \rho_0$ at small distances; then, the dark matter density distribution can be parametrized as:

$$\rho(r) = \frac{\rho_0}{1 + (r/a)^2} \tag{1.4}$$

where ρ_0 and a represent the measured [10] local dark matter density and the size of the galactic center, respectively.
From this consideration one can suppose that Dark Matter has a spherical distribution around the galactic center and its local density is around ~ 0.3 GeV/cm^3.

1.1.2 Gravitational lensing

As a consequence of General Relativity, a big massive object changes the trajectory of light, acting as a refractive lens [7]. This effect, called gravitational lensing, is often used in astronomy to evaluate the intensity of gravitational fields due to galaxies.
The deflection angle of light $\Delta\Phi$, that has an impact parameter b on the gravitational source with mass M , is:

$$\Delta\Phi = \frac{4GM}{b} \tag{1.5}$$

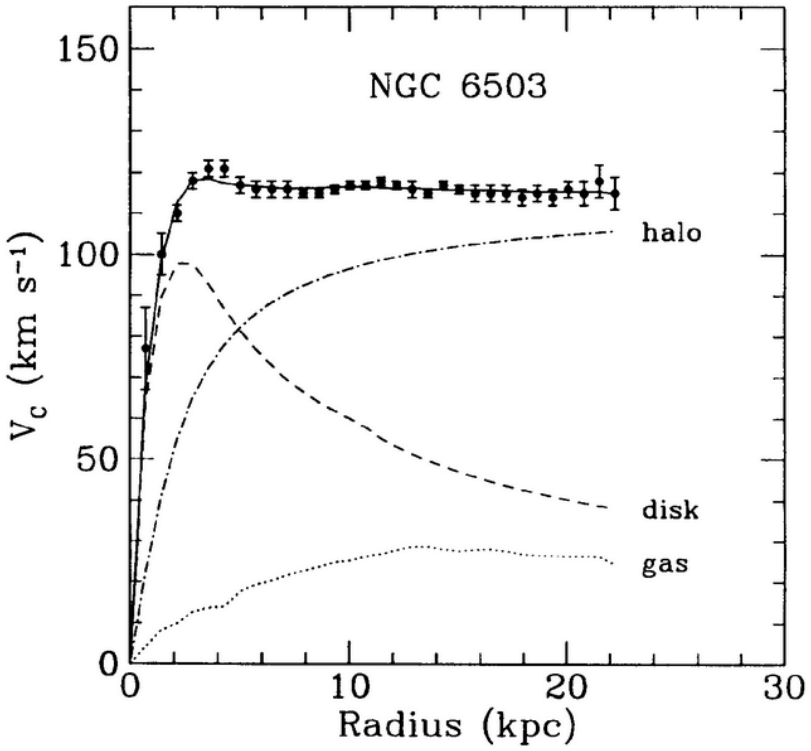

Figure 1.1: Rotation curve of the dwarf spiral galaxy NGC6503 [9]. The dashed line (disk) is the shape expected from theory, the fitted dots are the experimental results, while halo is the invisible mass required to match the experimental results

where G is the gravitational constant. Such effect has been observed for the first time by the astronomer Eddington in 1919 during a total solar eclipse [11].
A gravitational lensing phenomena due to a galaxy cluster was observed for the first time in 1979. A quasar that appears as two images from the gravitational lensing of the galaxy YGKOW G1, called Twin OSO, confirmed this effect as due to a galaxy [12]. Moreover, the gravitational lensing in galaxy clusters or quasars can be explained with a big amount of non luminuos mass interposed between the object and the Earth. The more the image of galaxy clusters or quasars is distorted, the higher is the amount of dark matter. Figure 1.2 shows the scheme of the gravitational lensing phenomena in the galaxy cluster Abell 2218 [13].

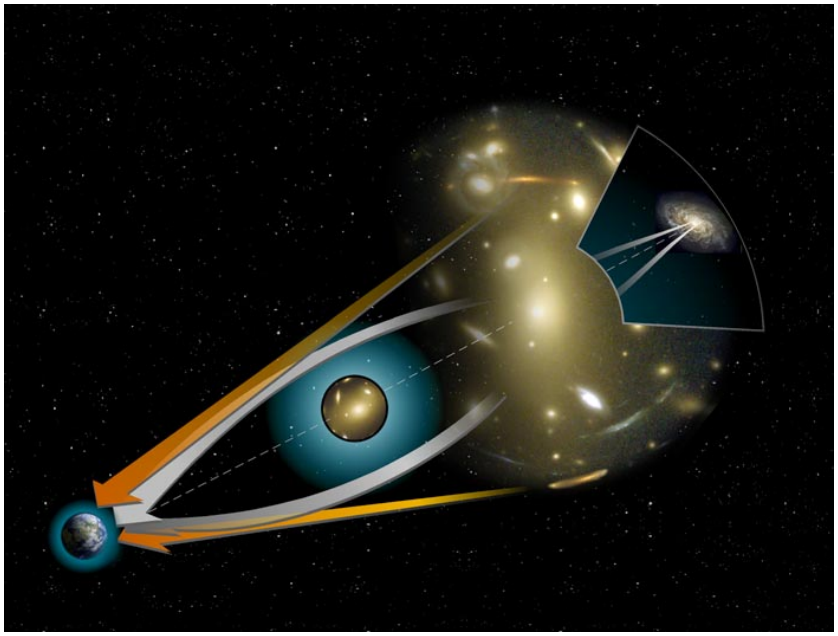

Figure 1.2: Scheme of gravitational lensing phenomena, where a big massive object bend the space-time changing the trajectory of the light

1.1.3 Bullet cluster

A collision of two galaxy clusters is called "bullet cluster" [7]. Since galaxies are made of stars and hot gasses, during this collision the gravitational field of the cluster decelerate the stellar component, while the two gaseous components behave as a collision particle fluid. Most of the baryonic matter is in form of hot gas, then, by mapping it by the emission of X-rays during the galaxy collision, it was possible to map the main baryonic component. Moreover, the distribution of the visible light obtained by the stars in the galaxies, matches that of gravitational potential from the lensing effect. However, due to their small mass, stars themselves cannot explain gravitational lensing; thus, there should be a non-luminous matter in these clusters with the distribution of mass similar to the distribution of stars.
In 2004, from the collision of the subcluster 1E 0657-558 [14], a discrepancy between the baryonic matter distribution was observed. It was measured from the X-ray emission and the gravitational field distribution obtained from lensing (Figures 1.2 and 1.3). The separation among the two areas can be explained by the fact that after the collision the hot gas still interact while the dark matter does not decelerate and just follow inertially its initial path. It would indicate us that DM has a non-collisional nature and is not in form

Figure 1.3: Distorted image of the galaxy cluster Abell-2218 [13]

of gas.

1.1.4 Dark energy

In the 1990s, two teams of astronomers pioneered a method to find and use distant supernovae as standard candles to probe the Universe [1]. What they found was very startling. A supernova **S1a** explosion is the final episode in the life of a binary pair of unequal mass stars. The more massive star in the pair will evolve faster than its companion, such that by the time it has evolved to become a white dwarf, its partner is in the red giant phase. The gravity of the white drarf will strip the red giant of its loosely bound outer layers, resulting in the increase of its own mass. This cannibalism will only cease when the mass of the white dwarf approaches the 'Chandrasekhar mass limit', which is $1.44 M_{SUN}$. Above this mass limit, the electron degeneracy particle pressure, which has been supporting the white dwarf until this point, will no longer be sufficient to prevent the gravitational collapse of the dwarf's core into a black hole. As this event always occurs at the same limiting

mass, the light emitted by this explosions has roughly the same total energy, or luminosity **L**. This is known as a 'standard candle'. If you can find an **SN1a**, you can measure the variation of its flux **f** over time and you can then calculate distances D_L of all the supernovae that you've detected:

$$f = \frac{L}{4\pi D_L^2} \tag{1.6}$$

An alternative method to determine distances to any object in the Universe is through the measurement of their redshift z, which is defined as:

$$z = \frac{\lambda_0 - \lambda_e}{\lambda_e} \tag{1.7}$$

where λ_e is the wavelenght emitted and λ_O observed.
On the other hand, Hubble's law states that there is a linear relationship between the redshift of the light emitted by galaxies and their distance D. The greater the distance of the galaxy, the greater its redshift:

$$z = \frac{H_0 \cdot D}{c} \tag{1.8}$$

where H_0 is the Hubble constant, whose currently estimated value is around $67.15 \frac{km}{s \cdot Mpc}$. So, the relationship between redshift and distance depends on the Hubble parameter H_0 that quantifies the rate of the expansion of the Universe, and on whether the expansion is accelerating or decelerating, quantified through the named 'deceleration parameter', **q**. For a decelerating Universe, which was the belief before the Supernova results, $q > 0$. The equation for the full distance - redshift relation is quite extensive, but for redshifts with $z < 1$, a good approximation is given by

$$D_L \approx \frac{c[z - (\frac{1+q}{2})z^2]}{H_0(1+z)} \tag{1.9}$$

In equation 1.6 we have a method to obtain direct measurements of distances in the Universe. In equation 1.9 we have a method to obtain an indirect measurement of distance that depends on the rate of expansion of the Universe. The supernova data shows that $q < 0$, and the expansion of the Universe is therefore accelerating. This discovery led to speculate the existence of the so-called dark energy. What is dark energy? While the astronomical community is united in postulating the existence of dark matter, the same cannot be said about dark energy. Observations that the expansion of Universe is accelerating are more easily explainded considering extra energy associated with the vacuum that permeates the Universe. According to quantum theory, empty space is filled with virtual particles with a wide range

of masses that can briefly pop in and out of existence. As mass and energy are equivalent, the growing vacuum within an expanding Universe acts like a bank of unlimited energy, inflating the whole Universe at an accelerated speed. Unfortunately, there is a problem. Particle and quantum physicists can make a theoretical estimate for the energy of a vacuum and they find that is roughly 60 orders of magnitude larger than the amount of dark energy determined by supernova result. This discrepancy has opened up a wide range of dark energy theories including exotic models such as a multiverse containing many realisations of different bubble universes. Perhaps our Universe is just one of those bubbles where the value of vacuum energy is unusually low. Or it could be that the Universe is experiencing a new period of inflation, akin to the rapid period of inflaction 10-30 s after the Big Bang, when it is thought that an almost instantaneous expansion created the cosmological scales in the Universe. Maybe a new fundamental force field has recently kicked into action, causing this new phase of accelerated expansion. Some cosmologists believe that the dark energy phenomenon indicates that we need to look beyond Einstein's theory of general relativity. By observing how dark matter structures change over cosmic time, we can investigate how dark energy evolves and test gravity for the first time on cosmological scales. Just as Einstein revolutionised our understanding of Newtonian gravity, so new observations of gravity on cosmological scales may bring about another revolution in our undertstanding of gravity.

1.2 Anisotropy in CMB spectrum and the cosmological parameters of the Universe

Another strong experimental evidence of dark matter and dark energy comes from the measurement of the spectrum of the Cosmic Microwawe Background (CMB) radiation obtained by means of radio telescopes [7].
The CMB is made of photons from the primordial Universe, when it became transparent to the radiation. This phenomena happened when the temperature dropped below 3000 K and electrons recombined with protons emitting photons that had not enough energy to ionize again hydrogen. Before the primordial nucleosynthesis, quantum fluctuations caused a matter distribution that wasn't uniform. In particular, it was hypothesized that in a first time dark matter was compressed by gravity, while baryonyc matter was decompressed by the the pressure of photons, but later, when the gravitational pressure became higher than the one of photons, the opposite happened. This process had an influence on the temperature of baryonic matter (increasing with its

compression), but not on dark matter, that does not interact with photons. The CMB, at the time of the recombination was in thermal equilibrium with matter, brings information on the anisotropies through the characteristic peak structure of its spectrum.
Figure 1.5 [15] illustrates the temperature angular power spectrum. The amplitude on the CMB do not fit the expectations if we take into account only the baryonic matter. Assuming that fluctuations in temperature started much earlier that the baryonic matter ones, inducing higher amplitudes in the spectrum at the recombination time, the experimental results would fit the expectations. Then, the hypothesis of the existence of dark matter is very strong. Moreover, from the size and the position of the peaks in the CMB power spectrum, it is possible to have information on the so-called "cosmological parameters". Cosmological parameters are the numbers required to describe the Universe when adopting a model called "flat Λ_{CDM}" model, that is, currently, the most accredited model for the dark Universe. "Flat" means that the global geometry of space-time is flat, "Λ" means that dark energy exists in the form of a 'cosmological constant' and 'CDM' implies that dark matter is 'cold' or 'non-relativistic' [1]. The most important cosmological parameters are:
• The baryonic matter density parameter: Ω_b
• The dark matter density parameter: Ω_{DM}
• The total matter density parameter: Ω_m
• The dark energy density parameter: Ω_Λ
• The Hubble parameter: $H_0 = 67.15 \frac{km}{s \cdot Mpc}$ (defined before)
In a flat Universe the total density of matter and energy is equal to the density that gives zero global curvature of space-time, or the 'critical density', ρ_{crit}, equivalent to six protons per cubic meter today. The total matter density parameter, Ω_m, is the ratio between the matter density ρ_m, and the critical density, $\Omega_m = \frac{\rho_m}{\rho_{crit}}$, and hence, for a flat Universe, the dark energy density parameter, $\Omega_\Lambda = 1 - \Omega_m$.
So, from observations of the fluctuations in density of the CMB it results that:

$$\Omega_b = 0,0480^{+0.0072}_{-0.0067} \tag{1.10}$$

$$\Omega_{DM} = 0.253^{+0.038}_{-0.036} \tag{1.11}$$

$$\Omega_m = 0.301^{+0.045}_{-0.042} \tag{1.12}$$

$$\Omega_\Lambda = 0.699^{+0.042}_{-0.045} \tag{1.13}$$

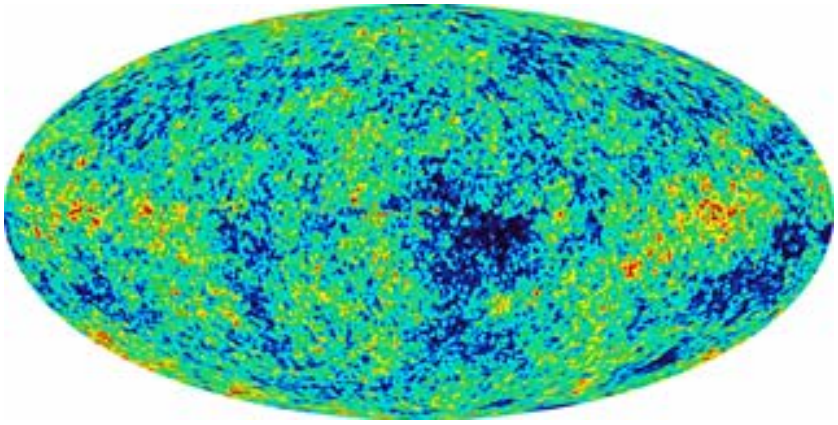

Figure 1.4: Map of the primordial universe, in which the variations of temperature was measured through the microwaves from CMB.

Thus dark energy constitute about 70% of the Universe while the majority of the matter content is in the form of dark matter.

1.3 Baryon acoustic oscillations

The acoustic oscillation battle in the early Universe, which causes the hot and cold spots in the CMB, also imprints a preferred distance scale in the distribution of ordinary matter. We can use this scale as a "standard ruler", using measurements of the distribution of galaxies at different epochs in time to track the accelerated expansion of the Universe [1].
To understand the origin of this ruler, picture the early Universe and focus in on an over-dense region in the plasma of photons and charged particles. The resulting increasing outward radiation pressure will eventually halt and reverse the gravitational collapse. The process can repeat, over and over again, setting up a local oscillator. These oscillations occur on many different scales throughout the Universe sending waves out into the plasma. This adds new fluctuations on top of the initial distributions of baryons that was seeded by the quantum fluctuations before inflation. The more cycles each oscillator passes through, the more damped these waves become. The biggest amplitude wave will therefore arise from the largest scale over-density to have undergone a single compression, sending a single pulse out into the plasma before recombination.
In the expanding Universe, the plasma density decreases, photons travel further before scattering off other particles, and athoms form. Having travelled far from their origin, the crest of all the sound waves become frozen in time

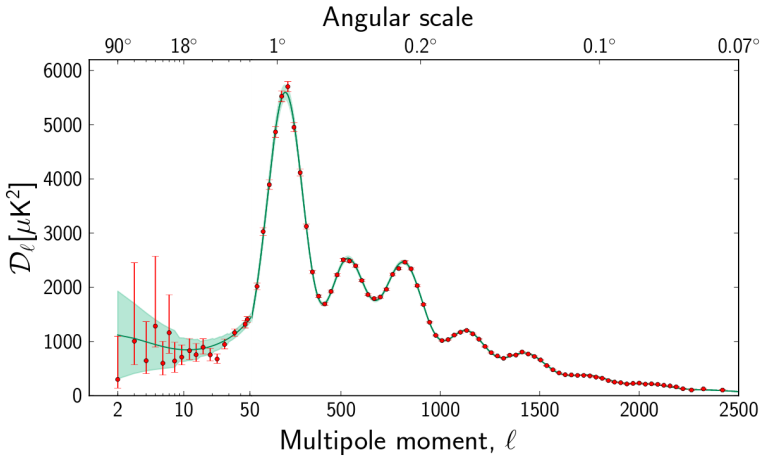

Figure 1.5: The 2013 Planck CMB temperature angular power spectrum [15].

because the fluid, which they have been travelling through, ceases to exist. For our largest amplitude wave, and other whose source has also been caught in the same instant of maximum collapse, their origin hosts a massive over-density of particles.
Given a cosmological model, the sound speed in the plasma can be calculated and it is found to be very fast, close to $c/\sqrt{3}$. As the collapse timescale is fixed by the age of the Universe at recombination, the position of the crest of our high-amplitude single pulse wave, relative to its origin, can then be determined.
Using CMB data, this is found to be in a spherical shell of radius $\sim 150 Mpc$. This fixed scale-lenghth from the early Universe provides the theoretical underpinning for our observational standard ruler in the present day.
Completely oblivious to the electromagnetic force battles going on around it, large-scale dark matter fluctuations will collapse under gravity. But the rapid, radiation-driven expansion, which occurs before recombination, prevents the growth in the density of dark matter structures that are smaller in size than the 'horizon', which is set by the furthest distance that light could have travelled at that moment in time.
Post-recombination, the Universe is transparent and the photons are free-streaming through the expanding Universe. A field of clumpy dark matter and baryonic particles remains. Forming deep potential wells, the growing dark matter clumps have been awaiting the epoch of recombination enabling the gravitational attraction of the baryonic particles. There is memory of the acoustic oscillations from the first 380000 years.
The Baryon Oscillation Spectroscopic Survey (BOSS) measured the redshift

and sky position of 1.2 milion of galaxies in the northern skies. Figure 1.6 shows the clustering of those galaxies as a function of their separation in the Universe, known as the galaxy correlation function. Specifically, it shows the numbers of galaxy pairs as a function of separation, relative to the number of pairs you would measure if they were distributed completely randomly. We expect galaxies to cluster together on small scales, as they live in the same dark matter haloes (clumps). As the distance between galaxies grows, we [expect to see the pair count tending towards the random pair count]. Until, that is, we hit the distance scale of the spherical shell that was frozen into the baryon distribution at recombination and has been expanding along with the growing Universe ever since. The presence of these shells can be clearly seen as an increase in the number of galaxy pairs separated by a 'comoving distance' of about 150 Mpc.
A comoving distance is defined as the distance between two objects that remains constant with time, if the two objects are moving with the Hubble flow, i.e. the global expansion of the Universe. It's therefore no surprise that BOSS finds the comoving distance to be the expected 150 Mpc, [in fact, it is by design]. In order to carry out this measurement of galaxy clustering, BOSS needs to assume a cosmological model, for example flat Λ_{CDM} and a set of cosmological parameters in order to turn the observed galaxy redshift and positions into distances. Theoretically, we know to expect a bump in the correlation function at the comoving distance 150 Mpc at all redshifts, and so the cosmological parameters from BOSS are in good agreement with those from the Plank CMB experiment.
This observational probe of cosmology has been called **Baryon Acoustic Oscillation (BAO)**. It is a powerful probe of the expansion rate of Universe, when used in combination with the CMB. All methods face some challenges, and for BAO it all depends on whether the galaxies trace the underlying matter distribution with sufficient accuracy to carry out this measurement; it is the total matter distribution not the galaxy distribution that carries the cosmological information. Given the large scales of the BAO signal, however, this is a fairly safe assumption to make given the current accurancy of the measurements.

1.4 Redshift space distorsion

In our expanding Universe, every galaxy is moving away from every other galaxy, following what is known as the 'Hubble flow'. Measuring the resulting redshift in the emission and absorption lines of galaxy specra then allows us to calculate distances to each galaxy, given a cosmological model. This

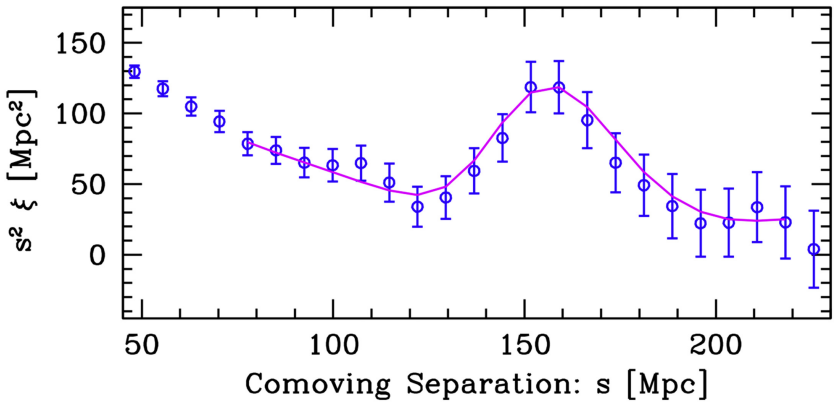

Figure 1.6: The baryon acoustic oscillation, as seen as a peak in the large-scale clustering from BOSS. The clustering statistic ζ measures the number of pairs that you would measure from a purely random distribution of galaxies. The pinh curve is the theoretical model assuming a flat Λ_{CDM} model, which provides an excellent fit to the BOSS data (blue dots). Data source: [2]

description is not the complete picture, however, as it misses the impact of local gravitational distortions that add 'peculiar' velocities. Take our nearest neighbour Andromeda as an example. It has a redshift of $z = -0.001$, which is actually a blueshift. Andromeda and the Milky Way are moving towards each other under the gravitational forces of a large-scale dark matter structure in which our whole Local Group of Galaxies is housed [1].
Figure 1.7 shows a computer simulation of a Λ_{CDM} cosmology. The observer is at the centre of the diagram looking out at a stripe across the sky. The quadrant on the left of the images shows the distribution of the galaxies that would be observed in terms of their true distance from the observer. Blue dots represents galaxies. You can see that the galaxies are tracing out the cosmic-web-like structure of the underlying dark matter, where the densest regions hosts the largest number of galaxies. The quadrant on the right shows the mirror image, but now plotted using the distances that you would have inferred from measurements of galaxy redshifts, using equation 1.4. In this case, we see that the web pattern is now stretched out along the 'line-of-sight' (i.e. the direction that the observer is looking in). We see this effect from the forwards (blue-shifted) and backwards (red-shifted) motion of galaxies hosted inside massive dark matter structures. The more massive the structure, i.e. the more dark matter there is, the faster the motion.
This observational probe has been called 'redshift space distorsion' or RDS. You then also measure the clustering for galaxies pairs that are relatively close to each along the line of sight, but are now separated by a certain distance

across the sky. If there were no peculiar velocities, you would expect to find the same clustering measurements out to scales of about 10 Mpc.
On larger scales, another interesting effect can be detected with RDS. Over long distances, galaxies are being gravitationally attracted and drawn towards over-dense structures. For galaxies housed in different haloes, this effect will tend to pull them towards each other. For pairs separated along the line of sight, this additional peculiar velocity will add to the redshift of one member of the pair, while the other will experience some opposing blueshift. For galaxy pairs that are separated across the sky, in other words, perpendicular to the line of sight, these pairs will still be attracted towards each other. The additional peculiar velocity will, however, be in a direction that is perpendicular to us as observers, thus making no change to the galaxy redshifts that we measure. The more massive structures there are in the Universe, the stronger the difference will be between the two-large scale RDS clustering measurements.
Members of the BOSS survey have found that their measurements are consistent with the expectation of the best fitting flat Λ_{CDM} model from the Plank CMB experiment. All methods face some challenges, and for RSD, just as with BAO, it all depends on whether the galaxies trace the underlying matter distribution in a manner sufficiently accurate to enable direct comparison between data and theory; it is the total matter distribution, not the galaxy distribution, that carries the cosmological information. Given the distance scales over which the RSD signal is measured, we don't yet know if it's save to assume a linear relationship between the galaxy distribution and dark matter distribution. This matter is often referred to as galaxy bias and is a potential limitation for obtaining accurate cosmology from RSD measurement. When used in combination with weak lensing measurements to calibrate the galaxy bias mapping between galaxies and dark matter, this cosmological probe holds significant promise.

1.5 Future prospects

Currently, we are in a very important phase for observational cosmology [1]. In the short-term there are lensing teams currently competing to be the first to reveal the next major leap in our understanding of the dark Universe. KiDS along with the Hyper-Suprime Camers survey are imaging 1500 square degrees of the cosmos, nearly 5% of the full-sky. The dark Energy Survey, will cover more then three times that area, and all three

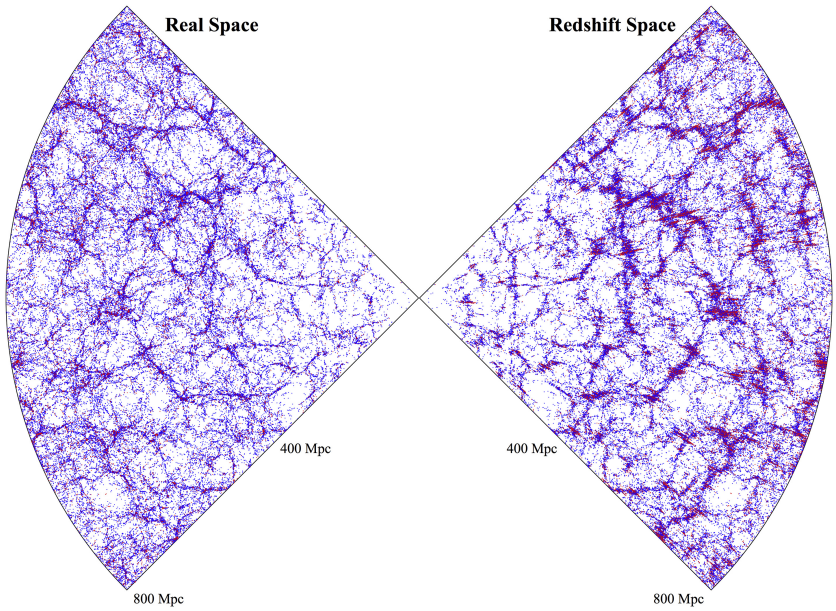

Figure 1.7: Illustrating redshift space distorsion using a mock galaxy catalogue of a Λ_{CDM} cosmology. On the left we see the 'real space' distribution. If we measured the redshifts for all these galaxies and used the redshifts for all these galaxies and used the redshifts to estimate a distance to each galaxy, we would infer that the galaxies were distributed as shown in the 'redshift space' mirror image universe on the right. In dense regions, the gravitation introduce additional peculiar velocities, distorting the true distribution of galaxies, hence the name "redshift space distorsion". Data source: [3]

surveys will conclude their observations over the next few years. Over the next decade, three new major international projects will work in tandem in the hopefully final stages of our quest to understand the dark side. The Euclid satellite [5] will be launched above the atmosphere, providing images as good as those taken with the Hubble Space Telescope across the whole sky and near infrared spectroscopy for millions of high redshift galaxies. Getting above the atmosphere gives us a much clearer view of the Universe, and the keen vision of the space telescope Euclid [5] will be extremely sensitive to the weak dark matter distorsion and the baryon acoustic oscillations that we are trying to detect. The Dark Energy Spectroscopy Instrument will also measure the spectra, and hence redshift and distance informations, of millions of galaxies with which to chart the expansion of the Universe and the growth of structures using both baryon acoustic oscillations and redshift space distorsions. The Large Synoptic Survey thus allow us to

chart the evolution of dark matter structures, but this telescope will also be able to detect killer rocks in our solar system that may one day obliterate planet Earth! Looking sliightly further into the future, the Wide Field Infra-Red Survey Telescope (WFIRST) will peer deep into the over a 1000 square degree patch, using weak lensing to resolve dark matter structures out of a redshift $z = 2$. The Square Kilometre Array, being built in South Africa and Australia, will provide high-resolution imaging in the radio part of the electromagnetic spectrum, with precision redshift and polarisation observations that will allow us to untangle the lensing alignment signature of dark matter from naturally arising alignments. In combination, these surveys will be able to use gravitational lensing to map dark matter and dark energy over the last 10 bilion years in the history of the Universe, testing gravity on the largest of scales in space and time. Experimenters hope to find out something truly ground-breacking and unexpected. Perhaps the current model of gravity is incomplete and when we finish this puzzle we will have turned our understanding of the Dark Universe. However, it may happen that they will not be found deviations from the default flat Λ_{CDM} model that Plank has already clearly shown to fully explain the Universe right after the Big Bang. The most solid theoretical reason why Λ_{CDM} should be so small could be based on a theory that predicts an almost infinite number of multiple universes. Each of these bubble universes presents a different realization of the constant that determines the amplitudes of the fundamental forces. We imagine that our Universe is the only reality, but perhaps the reason why we exist at all it is because in our realization the fundamental constants, including Λ_{CDM}, are well-tuned for life. As an observer, this is a hard concept to accept as it cannot be directly tested. However, further results are expected from the next generation of CMB experiments [6]scheduled for the next decades before reaching this conclusion of the multiverse.
In conclusion, all the proposed theories will have to be rigorously compared based on future experimental results

1.6 The nature of dark matter: possible explanation and candidates

A plausible solution to describe some of the astronomical measurements mentioned before is a modification of gravitation laws to accomodate the observations [24]. Such modified Newtonian dynamic models like MOND [39] or its relativistic extension TeVeS [40] can, for instance, succesfully describe rotational velocities measured in galaxies. However, MOND fails or needs

unrealistics parameters to fit observations on larger scales such as structure formations or the CMB structure and violates fundamental laws such as momentum conservation and the cosmological principle [41]. While TeVeS can solve some of conceptual problems of MOND, the required parameters seem to generate an unstable Universe [42] or fails to simultaneously fit lensing and rotation curves [43].

Massive astrophysical compact halo objects (MACHOs) have also been considered as a possible explanation for large mass to light ratios detected in the astronomical observations described in the previous section. These objects could be neutron stars, blac holes, brown dwarfs or unassociated planets that would emit very little to no radiation. Searches for such objects using gravitational microlensing [44] towards the Large Magellanic Cloud have been preformed [45]. Extrapolations to the Galactic dark matter halo showed that MACHOs can make up about 20% of the dark matter in our galaxy and that a model with MACHOs accounting entirely for the dark matter halo is ruled out at 95% of confidence level (34). The baryonic nature of dark matter is actually also ruled out by Big-Bang nucleosynthesis (BNN). The abundance of light elements predicted by BNN depends on the baryon density to a value of $\Omega_b = 0.04$ [46] close to the value derived from CMB. An example of baryonic dark matter, which is not affected by the BNN and CMB constraints mentioned above, are primordial black holes [47] [48]. Even though a large part of the viable parameter space is already excluded, for some black hole masses this explanation is still possible.

A more common ansats is to assume that dark matter is made out of massive neutral particles featuring a weak interaction. From the known particles in the standard model, only the neutrino could be considered. Due to its relativistic velocity in the early Universe, the neutrino would constitute a hot dark matter candidate. Cosmological simulations have shown, however, that a Universe dominate by neutrinos would not be in agreement with the observed dark-matter density in halos [49] [50]. Sterile neutrinos are hypotetical particles which were originally introduced to explain the smallness of the neutrino masses [51]. Additionally, they provide a viable dark matter candidate [52] [54]. Possible masses, which are not yet constrained by X-ray measurements or the analysis of dwarfts spheroidal galaxies, range from 1 keV to tens of keV. Given this very low mass, and the low interactions strenght, the existence of sterile neutrinos is not tested by direct detection experiments. An indication could, for example, arise from the X-ray measurements of the sterile neutrino decay via the radiative channel $N \rightarrow N\nu\gamma$ (N = Nucleus) [55] .

Models beyond the Standard Model of particle physics suggest the existence of new particles which could account for the dark matter. If such hypoytetical

particles would be stable, neutral and have a mass from below GeV/c^2 to several TeV/c^2, they could be the weakly interacting massive particles (WIMP). The standard production mechanism for WIMPs assumes that in the early Universe these particles were in equilibrium with the thermal plasma [56]. At this freeze-out temperature, when the WIMP annihilation rate was smaller than the Hubble expansion rate, the dark matter relic density was estabilished. The cross section necessary to observe the current dark matter density is of the order of weak interaction scale, It appears as a great coincidence that a particle interacting via the weak force would produce the right relic abundance and, therefore, the WIMP is a theoretically well motivated dark matter candidate. This hypothesis is being throughly tested experimentally with no unambiguous signal appearing. If the absence of signals remainss in the upcoming generation of experiments, the WIMP paradigm might be challenged [57] [58].
Supersymmetry models [59] are proposed as extensions of the Standard Model of particle physics to solve the hierarchy problem as well as unification of weak, strong and electromagnetic interactions. In this model, a whole new set of particles are postulated such that for each particle in the Standard Model there is a supersymmetric partner. Each particle differs from its partner by 1/2 in spin and, consequently, bosons are related to fermions and vice versa. The neutralino, the lighest neutral particle which appears as a superposition of the partners of the Standard Model bosons, constitutes an example of a new particle fulfilling the properties of WIMP. The typical masses predicted for the neutralino range from fev GeV/c^2 to several TeV/c^2.
A WIMP candidate appears also in models with extra-dimensions. In such models N spatial dimensions are added to the (3+1) space time classical ones. They appeared already around 1920 to unify electromagnetism with gravity. The lightest stable particle is called 'lightest Kaluza particle' and costitutes also a good WIMP candidate [60] [61].
Among the non-WIMP candidates, 'superheavy dark matter' or 'WIMPzillas' are postulated to explain the origin of ultra-high energy cosmic rays [62]. At energies close to $10^{20}eV$, cosmic protons can interact with cosmic microwave background and, thus, their mean free path is reduced resulting in a suppressed measured flux [63] [64]. Experimental results include, however, the detection of a few events above the expected cut-off, motivating a superheavy dark matter candidate. Decays of these non-thermally-produced [65] superheavy particles with masses of $10^{12}-10^{16}GeV/c^2$ could account for the observations, being at the same time responsible for the dark matter in the Universe.
Finally, a very motivated particle and dark matter candidate is the axion. In the Standard Model of particle physics, there is no fundamental reasons why QCD should conserve P and CP. However, from the experimental bound

of the neutron electric dipole moment [66], very small values of P and CP violation can be derived. In order to solve this so-called 'strong CP-problem' [67], a new simmetry was postulated (56)in 1977. When this simmetry is spontaneously broken, a massive particle, the axion, appears. The axion mass and the coupling strenght to ordinary matter are inversely proportional to the breaking scale which was originally associated to the electroweak scale. This original axion model is ruled out by laboratory experiments [69]. Cosmological and astrophisical results provide as well very strong bounds on the axion hypothesis [67]. There exist, however, further 'invisible' axions models in which the breaking scale is a free parameter, KSVZ [70] [71] and DFSZ [72] [73], and still provide a solution to the CP-problem. Invisible axions or axion-like particles, would have been produced no-thermally in the early Universe by mechanism like the so called "vacuum realignment" (vacuum realignement consists in a modify of the structure of the QCD vacuum) [74] [75] for example, giving the right dark matter abundance. The resulting free path lenght would be small and, therefore, these axions are a 'cold' candidate. For certain parameters, axions could account for the complete missing matter [76].
Sterile neutrinos, WIMPs, superheavy particles and axions are not the only particle candidate proposed. The candidates mentioned above arise from models that were proposed originally with a different motivation and not to explain dark matter. The fact that the models are motivated by different unresolved observations strengthen the relevance of the predicted dark matter candidate. A more comprehensive review on dark matter candidates can be found for exemple in [77].
Finally, the most accredited dark matter particle is supposed to be a Majorana particle, i.e. a particle that coincides with its antiparticle [7]. The DM particle, like other particles in the early universe, would have found itself in a thermal equilibrium through the processes of creation and annihilation. As the Universe expanded as it cooled, the temperature of the particles dropped below their creation energy (in the case of WIMPs $T \sim \frac{1}{20} m_{WIMP}$), so the particles were not produced anymore. At some point, during the expansion the annihilation rate of a particle is also suppressed and the abundance of relics is fixed ($freeze - out$) to

$$\Omega \approx \frac{G^{(3/2)} T_0^3}{H_0^2 < \sigma v >} = \frac{3 \cdot 10^{-27} cm^3/s}{< \sigma v >} \tag{1.14}$$

where $< \sigma v >$ is the average self-annihilation cross section multiplied by the velocity of the particle (for WIMP $< \sigma v > \sim \alpha^2 / 8\pi m_{WIMP}^2$). In order to accomodate the correct abundance of dark matter Ω_{DM} in the Universe, it should have a cross section in the electroweak scale and a mass in the range of

GeV and TeV. Those are exactly the aspects required by a WIMP particle. Some Standard Model's extensions predict the existence of particles that could be dark matter, but there are no experimental result that confirm their existence. One of these theories, called Supersymmetry (SUSY) [16], tries to unify the electromagnetic, weak and strong fundamental forces at high energies. As mentioned in the previous section, the lightest Supersymmetric Particle (LSP) in several SUSY models is called neutralino, and it would have a mass in GeV-TeV range, or the same mass and interaction scale expected for dark matter.

Chapter 2

Dark matter direct detection experiments

2.1 Search for dark matter particles

The particle dark matter hypothesis can be tested through three methods: their production at particle accelerators, indirect search for signals from annihilation products and direct search from scattering on target nuclei. Figure 2.1 illustrates a representation of the possible couplings between a dark matter particle χ and an ordinary matter particle P. While the annihilation of dark matter particles (downwards direction) could give pairs of standard model particles, the collision of electrons or protons at colliders could produce pairs of dark matter particles.

2.1.1 Search of dark matter through their production at particle accelerators

Since the start of Large Hadron Collider (LHC) at CERN in 2008, CMS [78] and ATLAS [79] have searched for new particles in proton-proton collisions up to a center-of-mass energy of 13 TeV [24]. Besides the discovery of the Higgs particle [80] [81], these experiments have studied a number of new particle signatures by scanning the parameter space of different supersymmetric and extra-dimension models. The presence of a dark matter particle would only be inferred by observing events with missing transferred momentum and energy. Therefore, events with, e.g, an energetic jet and an imbalanced momentum transfert are selected for analysis. Reactions like this:

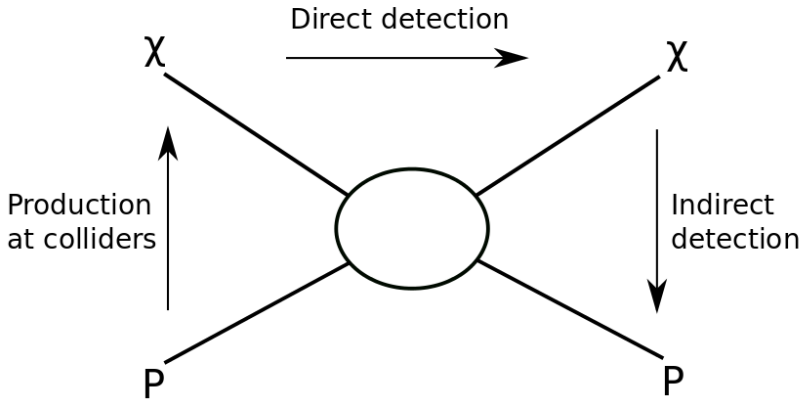

Figure 2.1: Schematic showing the possible dark matter channels

$$pp \rightarrow \chi\chi + X \tag{2.1}$$

are probed, where X is a hadronic jet, a photon or a leptonically decaying Z or W boson. The results obtained so far are consistent with the expectations of Standard Model (see for exemple [82] [83] [84]) but in next years further searches will be performed. The derived bounds can be translated into limits on the cross-section for a given particle mass. Bounds arising from accelerator searches are mostly constraining below $\sim$ 5 GeV and $\sim$ a few hundreds of GeV for spin-independent and spin-dependent (proton, neutron coupling) interaction, respectively. However, a direct comparison of these experimental results to other detection methods is, in general, model dependent.

2.1.2 Dark matter indirect detection

Dark matter particles can gravitationally accumulate in astrophisical objects such as stars and galaxies [24]. The most favoured sources to search for indirect signals are the galactic centre and halo, close galaxy clusters of dwarf galaxies, the so called "dwarf spheroidal". The latter are very popular locations due to their large measured mass to light ratio and their small background. Due to the increased dark-matter density, an enhanced self-annihilation, scattering or decay into standard model particles could produce a measurable particle flux (see [85] for a detailed discussion). This method based on the detection of these secondary particles is called "indirect detection". A second method of trying to detect dark matter particles is to look for ordinary matter particles generated by their decay. Two examples of indirect detection are given by the ecxess of gammas from the galactic center and the

excess of positrons detected by Pamela [32] and AMS-02 [33]. In contrast to annihilation processes, where the production rate shows a quadratic dependence on the dark matter density, decay of dark matter scales linearly. Furthermore, dark matter particles might be gravitationally captured inside the Sun, and then the annihilation of captured dark-matter particles can produce neutrinos which can propagate out of the Sun and might be detectable with Earth-based neutrino telescopes. The total number of captured particles is less affected by uncertainties of the dark matter halo because this process lasts for billions of years and dark matter density variations are averaged out [86].
Charged particles, or cosmic rays produced by annihilation between two dark matter particles, are deflected in the interstellar magnetic fields loosing the information on their origin. Due to their charge neutrality, γ-rays can be affected by absorption in the interstellar medium.
Imaging atmospheric Cherenkov telescopes for TeV γ-rays detection can look specifically in the direction of objects where a large amount of dark matter is expected to be. Either a γ-flux from dwarf galaxies or galaxy cluster (as hypothesizes by Fritz Zwicky in 1933), or mono-energetic line signatures are searched for.
The energy scale of indirect DM signals depends on the DM mass [25]. On largely model-independent grounds, the DM mass is constrained from below by quantum effects having to exist on scales smaller than the size of the smallest gravitationally collapsed objects, and from above from the requirement that macroscopic DM particles not disrupt the stability of long-lived structures in the Universe, such as globular clusters and galactic disks. As a result, the landscape of possible DM masses ranges over more than 90 orders of magnitude, from approximately 10^{-22} eV up to 10^{70} eV.
At the lowest mass scale, "fuzzy" or "wave" dark matter has spawned numerous exciting new ideas both in the experiments then in observations of emission lines. While strong constraints exist from observations of the 21 cm line, the experimental landscape now includes a number of novel setups as ABRACADABRA [26], LC resonators, HAYSTAC [27] and MW cavities.
Observations of an unidentified X-ray line at 3.5 keV in the spectrum of individual and stacked clusters of galaxies as well as in the Galactic center has spurred much interest, as it could arise from the decay of an approximately 7 keV sterile neutrino to an active neutrino and a photon. Sterile neutrinos are viable dark matter candidates possibly connected with ordinary neutrinos via both baryogenesis and leptogenesis. While the 3.5 keV might arise from a previously unaccounted for de-excitation line of K XVIII (a He-like potassium ion), observations of Draco with XMM strongly disfavors a sterile neutrino decay origin. New astrophysical solutions, such as charge-exchange processes, and new theoretical ideas, including "fluorescent" dark matter and axion-

like particle conversions have been proposed. A replacement to the Hitomi satellite [34], or a X-ray astronomy satellite commissionated by the Japan Aerospace Exploration Agency (JAXA) for studying extremely energetic process in the Universe, promises to clarify the observational situation with significantly improved energy resolution.
There is a new frontier for indirect detection in the MeV range, where eASTROGAM [28] and ComPair [29] are new instruments that would revolutionize existing observations. Furthermore, a interesting theoretical question arises on what the annihilation of MeV DM particles would look like, and how to evade CMB constraints. Production of photons can also be due to radiative processes of charged particles, for exemple the decay of hadrons. A new code, Hazma [30], allows for the matching of UV complete theories onto hadrons via chiral perturbation theory. A UV complete theory is one whose correlation functions or amplitudes may be calculated and yield unambiguously finite results for arbitrarily high energies. Constraints from cosmology strongly limit the possible ranges for the scattering cross section of MeV and sub-MeV DM with electrons, and so they strongly limit the new experiments proposed.
There is an excess of gamma-ray from the Galactic center that seems to persist despite it continues to rely on probably primitive models for the diffuse gamma radiation in the Galaxy. It was shown that supposing that a fraction of the cosmic-ray source are placed in regions of star formation makes the excess largely disappear. It is interesting to note that there is a similar excess in the Andromeda galaxy (M31), but in that system cosmic rays are a possible explanation for the production of gamma rays. There is also an additional excess in the globular cluster Omega Centauri, although again other sources, such as millisecond pulsars, are perfectly reasonable counterparts.
Overall, the prospects of establishing a conclusive DM signal from gamma-ray observations remain weak, although a conclusive detection, for instance of a gamma-ray line at MeV or TeV energies, remains a distinct possibility.
Furthermore, a startling signal is a rising positron fraction, measured by HEAT [31], Pamela [32], Fermi [35] and most recently by AMS-02 [33]. Nearby, mature pulsars appear to be likely counterparts, although a recent observational result from the HAWC telescope [36] has brought this possibility into question: specifically, the observation of TeV halos from inverse Compton scattering of CMB photons in the nebulae surrounding two nearby pulsars, Monogem and Geminga, often invoked as the source of the anomalous positrons, has shown that diffusion within PWNs is highly inefficient. In this scenario, positrons of high energy could not travel from those pulsars to Earth, if diffusion is inefficient throughout. However, the likely responsible is inhomogeneous diffusion, a possibility that is currently being tested.

While no excess seems to be present in the spectrum of antiprotons, AMS-02 [33] has reported the possible detection of massive antinuclei such as anti-Helium-3 and anti-Helium-4. If this is indeed confirmed, DM annihilation might be invoked as a solution, despite at the expense of stretching the coalescence picturw that leads to the prediction of the formation of heavy antinuclei from DM-produced antinucleons.
The detection of gravitational waves led to hypothesize primordial black holes (PBH) as possible DM candidates. The black holes detected by LIGO and VIRGO [37] [38] can actually be of primordial origin, as the low measured spins for most of the recently reported events suggest, although super-radiance could also be responsible for the low observed spin. The concept of super-radiance was introduced by R.H. Dicke (1954) to indicate the spontaneous and coherent emission of radiation, whose power is proportional to the square of the number N of emitting atoms (or molecules), which however must be large; the decay time constant is inversely proportional to N. CMB limits are currently being re-evaluated, but a conclusive evidence for a primordial origin might lie with the detection of a sub-Chandrasekhar mass merging BH. The mass of Chandrasekhar is about 1.44 solar masses and it is the maximum limit for the mass of a star so that at the end of its life it becomes a white dwarf. Above this mass it will instead become a neutron star. It was recently been discovered that finite-sized source effects could ease the microlensing constraints resulting from star observation in the M31 galaxy with the SUBARU HSC camera. This observation effectively reopened the possibility of mass PBHs of asteroids as possible contributions to the 100% of DM in the Universe. PBH with much lighter masses, around 1 ton, could have evaporated to both dark matter and right-handed neutrinos, a possibility dubbed melanogenesis. Much lighter objects, around the Planck scale, or the reference scale that defines the applicability limit of current physical laws, quantum mechanics and relativity (all the quantities of the Plank scale, or Plank mass, Plank energy, Plank length,etc. refer to the Plank constant which is $6,626 \cdot 10^{-34}$) $J \cdot s$ might be stable because of quantum gravity or extremality, and be stuck with a relic electric charge. In this case, large neutrino detectors and also the so-called paleo-detectors could soon probe this possible class of ultra-heavy particle DM candidates.

2.2 Principles of WIMP direct detection

In order to develop experiments capable of directly testing the nature of dark matter particles, considerable work has been done [24]. The goal is to identify nuclear recoils produced by collisions between new particles and the

target nuclei of a detector. The elastic scattering of WIMPs with masses of $(10 - 1000)\ GeV/c^2$ would produce nuclear recoils in the range of $(1 - 100)$ keV [117].To identify such low-energy interactions unambiguously, detailed knowledge of signal signatures, particle physics aspects and nuclear physics modeling is mandatory. Furthermore, for the calculation of event rates in direct detection experiments, the dark matter density and the halo velocity distribution in the Milky Way are required.

2.2.1 Experimental signatures of dark matter

The signature of dark matter in a direct detection experiment consists of a recoil spectrum of single scattering events. Given the low interaction strenght expected for the dark matter particle, the probability of multiple collisions within a detector is negligible. In case of a WIMP, a nuclear recoil is expected [118]. The differential recoil spectrum resulting from dark matter interaction can be written, following [117], as:

$$\frac{dR}{dE} = \frac{\rho_0}{m_\chi \cdot m_a} \cdot \int v \cdot f(v,t) \cdot \frac{d\sigma}{dE}(E.v) d^3v \tag{2.2}$$

where m_X is the dark matter mass and $\frac{d\sigma}{dE}$ its differential cross section. The WIMP cross-section σ and m_X are the two observables of a dark matter experiment. The dark matter velocity v is defined in the rest frame of the detector and m_A is the nucleus mass. Equation 2.2 shows explicitly the astrophisical parameters, the local dark matter density ρ_0 and f(v,t), which accounts for the WIMP velocity distribution in the detector reference frame. This velocity distribution is time dependent due to the revolution of the Earth around the Sun. Based on equation 2.2, detection strategies can exploit the energy, time or direction dependencies of the signal.
The most common approach in direct detection experiments is the attempt to measure the energy dependence of dark matter interactions. According to [117] equation 2.2 can be approximated by

$$\frac{dR}{dE}(E) \approx \frac{dR}{dE}_0 \cdot F^2(E) exp(-\frac{E}{E_0}) \tag{2.3}$$

where $(dR/dE)_0$ denotes the event rate at zero momentum transfer and E_0 is a constant parametrizing a characteristic energy scale which depends on the dark matter mass and target nucleus [117]. Hence, the signal is dominated at low recoil energies by the exponential function. $F^2(E)$ is the form-factor correction which will be described in more detail in the next section.
Another possible dark matter signature is the so-called "annual modulation". As a consequence of the Earth rotation around the Sun, the speed of the

dark matter particles in the Milky Way halo relative to the Earth is maximal in June 2nd and minimal in December 2nd. Consequently, the amount of particles able to produce nuclear recoils above the detectors' energy thresold is also largest in June [119]. As the amplitude of the variation is expected to be small, the temporal variation of the differential event rate can be written, following [120] as

$$\frac{dR}{dE}(E,t) \approx S_0(E) + S_m(E) \cdot cos(\frac{2\pi(t-t_0)}{T}) \tag{2.4}$$

where t_0 is the phase which is expected at about 150 days and T is the expected period of one year. The time-averaged event rate is denoted by S_0, whereas the modulation amplitudes is given by S_m. A rate modulation would, in principle, enhance the ability to discriminate against background and help to confirm a dark matter detection.
Directionality is another dark-matter signature which can be exploited for detection as the direction of the nuclear recoils resulting from WIMP interactions has a strong angular dependance (cfr. equation 2.5) [121]. This dependence can be seen in the differential rate equation when it is explicitly written as a function of the angle γ, defined by the direction of the nuclear recoil relative to the mean direction of the solar motion

$$\frac{dR}{dEdcos\gamma} \propto exp\frac{-[(v_E + v_{SUN})cos\gamma - v_{min}]^2}{v_c^2} \tag{2.5}$$

In equation 2.5, v_E represents the Earth's rotation motions around the Sun, v_{SUN} the velocity of the Sun around the galactic centre, v_{min} the minimum WIMP velocity that can produce a nuclear recoil of an energy E and v_c the halo circular velocity $v_c = \sqrt{\frac{3}{2}v_{SUN}}$. The integrated rate of events scattering in the forward direction will, therefore, exceded the rate for backwards scattering events by an order of magnitude [121]. An oscillation of the mean direction of recoils over a sidereal day is also expected due to the rotation of the Earth and if the detector is placed at an appropriate latitude. This directional signature allows to discriminate potential backgrounds [122]. A detector able to determine the direction of the WIMP-induced nuclear recoil would provide a powerful tool to confirm the measurement of dark matter particles.

2.2.2 Cross-sections and nuclear physics aspects

To interpret the data of the dark matter experiments, it is necessary to make further hypotheses on the specific model of particle physics and on the physics processes involved. This subsection summarizes the most significant possible

interactions between dark matter particles and target nucleons. However, interactions with electrons are also possible. The latter are very important for checking low-energies dark matter models.
For spin-independent WIMP interactions, it is assumed that, due to the conservation of the isospin, neutrons and protons contribute with the same weight to the scattering process. For a sufficiently low momentum transfer q, the scattering amplitude of each nucleon adds up in phase and results in a coherent process. For spin-dependent interactions, only umpaired nucleons contribute to scattering. Therefore, only nuclei with an odd number of protons or neutrons are sensitive to these interactions. In this case, the cross section is dependent on the spin content of the nucleon quark with components coming from both proton and neutron couplings.
When the momentum transfer is such that the particle wavelenght is no longer large compared to the nuclear radius, the cross section decreases with increasing q. The form factor F accounts for this effects and the cross section can be expressed as $\sigma \propto \sigma_0 \cdot F^2$, where σ_0 is the cross-section at zero momentum transfer. In general, the differential WIMP-nucleus cross section, $d\sigma/dE$ shown in the equation 2.2, can be written as the sum of a spin-indipendent (SI) contribution and and a spin-dependent (SD) one.
The form factor for SI interaction is calculated assuming the distribution of scattering centres to be the same as the charge distribution derived from electron, scattering experiments [117]. Commonly, the Helm parametrisation [124] is used to describe the form factor. Recent shell-model calculations [125] show that the derived structure factors are in good agreement with the classical parametrizations.
For spin-dependent interactions, the form factor is written in terms of the spin structure function whose terms are determined from nuclear shell model calculations.
In the physical processes illustrated in this section dark matter particles scatter the target nucleus producing nuclear recoils. Other types of interactions are possible, but we won't talk about them.

2.2.3 Distribution of dark matter in the Milky Way

The dark matter density in the Milky Way at the position of the Earth and its velocity distribution are astrophysical input parameters, needed to interpret the results of direct detection experiments. In this subsection are illustrated: the parameters of the standard halo model used to derive the properties of dark matter interactions, their uncertainties and the differences in modelling

the dark-matter halo itself.
In most cases we assume a local dark matter density of $0.3 GeV/cm^3$ which results from mass modelling of the Milky Way, using parameters in agreement with observational data [126]. However, depending on the profile model used for the halo, a density range from $(0.2 - 0.6) GeV/cm^3$ can be derived (see [127] for a review on this topic).
The profile of dark matter velocity is commonly described by an isotropic Maxwell-Boltzmann distribution

$$f(v) = \frac{1}{\sqrt{2\pi\sigma}} \cdot e^{-\frac{|v|^2}{2\sigma^2}} \tag{2.6}$$

truncated at velocities exceeding the escape velocity and where $\sigma = \sqrt{\frac{3}{2}}\, v_c$. A standard value $v_c = 220\ km/s$ is used for the local circular speed. This value results from an average of values found in different analyses. More recent studies using additional data and/or different methods, find velocities ranging from $(200 \pm 20)\ km/s$ to $(279 \pm 33\ km/s$ [126]. Finally, the escape velocity defines a cut-off in the description of the standard halo profile. The commonly used value of 544 km/s is the likelihood median calculated using data from the RAVE survey. RAVE survey is a spectroscopic astronomical survey of the stars in the Milky Way using the 1-2 meters UK Schmidt Telescope of the Australian Astronomical Observatoty (AAO) [129]. The 90% confidence interval contains velocities from 498 km/s to 608 km/s. These large ranges of possible values for the dark matter density, circular speed and escape velocity illustrate that the uncertainties in the halo modelling are significant [130]. Modelling the halo itself show uncertains, too
The dark matter density profile can only be indirectly observed (e.g. rotation velocities of stars), therefore, numerical simulations have been performed in order to understand the structure of halos. These simulations contained, traditionally, only dark matter [135] [136] [137] [138] and showed triaxial velocity distributions [134]. The resulting haloes feature, however, cusped profiles with steeper density variations towards the centre of halo, while observations favoured flatter cored-profiles. Moreover, the simulations predict a large amount of substructure, i.e. large number of subhaloes, in contradiction with the few haloes present in the Milky Way. These issues, currently under investigation, might challenge the validity of the ΛCDM model and different possible solutions are discussed. One solution could be related to the nature of dark matter or its properties [139]. A warm dark matter candidate with a larger free-steaming length could, for instance, modify the halo density profile

resulting in the observer cored-type profile and suppressing the formation of small structures. Another possibility is to consider candidates with weak interaction with matter but strong self-interaction [140]. The elastic scattering of these particles in the dense central region could modify the energy and momentum distribution resulting in cored dark matter profiles. Probably, the solution could be related to the absence of baryonic matter in the simulations. Nevertheless even with large simulations containing baryons, uncertaines in the dark matter halo remain and, thus, direct detection experiments generally use the common assumption of an isotropic Maxwell-Boltzmann distribution using values for astrophisical parameters as introduced before.

2.3 Background sourced and reduction techniques

In order to identify unambiguosly interactions from dark matter particles, ultra-low background experimental conditionns are required. This section illustrated the various contributions to background in direct dark matter experiments: external radiation by γ-rays, neutrons and neutrinos (common for all experiments) and internal backgrounds (solid-state and liquid detectors). The main strategies to suppress these backgrounds are also discussed.

2.3.1 Environmental gamma-ray radiation

Radiation from gamma-decays originates mainly from natural uranium and thorium decay chains and from decays of isotopes e.g ^{40}K, ^{60}Co and ^{137}Cs present in the surrounding materials. The uranium (^{238}U) and thorium (^{232}Th) chains, have a series of alpha and beta decays accompanied by the emission of several gamma rays with energies from tens of keV up to 2.6 MeV (highest γ-energy from the thorium chain). The interaction of γ-rays with matter include the photoelectric effect, Compton scattering and e^+e^- pair production [142]. While the photoelectric effect has the highest cross-section at energies up to few hundreds keV, the cross-section for pair production dominates above several MeV. For the energy in between, the Compton scattering is the most probable process. All these reactions results in the emission of an electron (or electron and positron for the pair production) which can deposit its energy in the target medium. Such energy depositions can be at energies of a few keV affecting the sensitivity of the experiments because this is the energy region of interest for dark matter searches.
Gamma radiation close to the sensitive volume of the detector, that is the volume of the detector in which the interactions can be detected, and the fiducial volume, that is the region whose "noise", or the number of expected

spurious events, is comparable to the number of signal events, can be reduced by selecting materials with low radioactive traces. Gamma-specrtometry using high purity germanium detectors is a powerful tecnique to select radiopure materials. Other techniques are also used [143].
Analysis tools can be used to further reduce the rate of background interactions. Given the low probability of dark matter particles to interact, the removal of multiple simultaneous hits in the target volume can be, for instance, used for background-event suppression.
Finally, detectors able to distinguish electronic recoils from nuclear recoils can reduce the background by exploiting the corresponding separation parameter. In Chapter 3 we'll talk in detail about how this technique is exploited in the XENON experiment.

2.3.2 Cosmogenic and radiogenic neutron radiation

Neutron can interact with nuclei in the detector target through elastic scattering producing nuclear recoils. In most cases, there is also a gamma emission which can be used to tag these events. Cosmogenic neutrons, with energy up to several GeV, are produced through spallation reactions of muons on nuclei [145] and are moderated by the detector surrounding materials. Radiogenic neutrons are instead emitted in (α,n) and spontaneous fission reaction from natural radioactivity [146]) and they have lower energies of around a few MeV.
Dark matter experiments are typically placed at underground laboratories in order to suppress as much as possible the cosmic rays and background connected to them, such as neutrons originated by muons spallation, and gammas. The deeper the location of the experiment, the lower the muon flux. Figure 2.2 shows the muon flux as a function of depth for different laboratories hosting dark matter experiments. The effective depth is calculated using the parametrisation which is represented by the black line in the figure. The muon flux for each underground location is taken from the corresponding reference of the list below.

- Waste Isolation Pilot Plant (WIPP) [147] in USA
- Laboratoire Souterrain a' Bras Bruit (LSBB) [148] in France
- Kamioka observatory [145] in Japan
- Soudan Underground Laboratory in USA
- Yang Yang Underground Lab (Y2L) [149] in Corea
- Boulby Underground Laboratory [145] in UK
- Laboratori Nazionali del Gran Sasso (LNGS) [145] in Italy
- Laboratoire Souterrain de Modane (LSM) in France

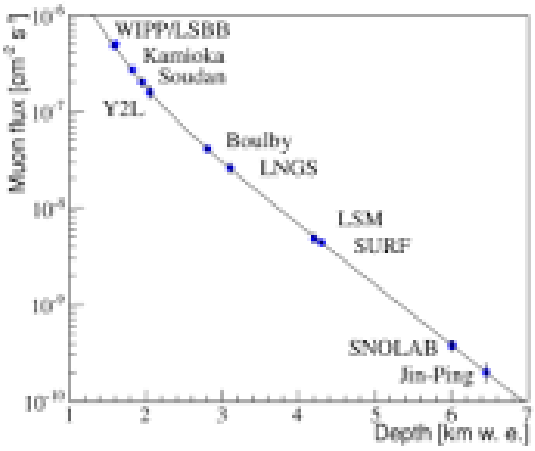

Figure 2.2: Muon flux as function of depth in kilometres water equivalent (km w.e.) for various underground laboratories hosting dark matter experiments. The effective depth is calculated using the parametrisation curve (thin line) from [145].

- Sanford Underground Research Facility (SURF) in USA
- SNOLAB [145] in Canada
- Jin-Ping laboratory [151] in China

The background particles from radiogenic unstable elements can be reduced by means of selection of detector material. Materials with low uranium and thorium content give lower α- and spontaneous fission rates. Detector shielding can also be used to reduce the external neutron flux [152]. Active vetoes are used to record interactions of muons. In chapter 4 we'll talk in details about how this is realized in the XENON experiment. The data acquired in the inner detector simultaneously to the muon event is discarded in order to reduce the muon-induced neutron background. Plastic scintillator plates are, for example, used for this purpose [144] [153]. This can be improved further by the use of water Cerenkov detectors [154] [155] as they provide a high muon tagging efficiency (full coverage), are efficient in stopping neutrons and, for sufficiently large tickness, the external gamma activity is also reduced. To tag directly the interactions of neutrons, shielding using liquid scintillators can be used [156].
Finally, the analysis techniques described in the previous sections can also be

applied to reduce the neutron background. The multiple scattering tagging is, for instance, particularly effective with growing size of targets. The fiducial volume selection can also be used, however, it has a smaller effect in the reduction of background for neutrons than for gamma interactions because of the larger mean free path of neutrons.

2.3.3 Neutrino background

With increasing target mass approaching hundreds of kilograms to tons, direct dark-matter detectors with sensitivity to keV energies start being sensitive to neutrino interactions. Neutrinons will become, therefore, a significant background contributing both to electronic and nuclear recoils. Solar neutrinos do elastic scattering with electrons: νe through interaction of charged current and neutral current, other neutrino flavours only through the interaction of neutral current [157]. Due to their larger fluxes, pp-and ^7Be-neutrinos would be the first neutrinos which could be detected. The resulting signal is a recoiling electron in contrast to the nuclear recoil resulting from WIMP interactions. Therefore, neutrino-electron scattering is an important background mainly for experiments which are not able to distinguish between nuclear and electronic recoil. Here, we consider neutrino-induced reactions as background but the measurement is interesting on itself as it can confirm the recent pp-neutrino measurement by the Borexino experiment [158], testing in real time the main energy production mechanism inside the Sun.
Neutrinos can also undergo coherent neutrino-nucleus elastic scattering producing nuclear recoils with energy up to few keV [159]. Although this process has not been measured yet, it is expected to be accessible in the experiments planed to run in the next couple of years. Dark matter detectors could be, hereby, the first to measure this process. Coherent scattering of solar neutrinos would limit the sensitivity of dark matter experiment for low WIMP masses, the coherent scattering of atmospheric neutrinos would limit dark matter searches at $\approx 10^{-49}\ cm^2$ [160] [161] [162]. In case of a positive signal at these cross-sections, in principle, the modulation of the signal along the year could be considered in order to distinguish WIMPs from neutrinos. While the WIMP rate should peak around June 2nd, the rate of solar neutrinos should peack around January 3rd due to the large solid angle during the perihelion. The rate of atmospheric neutrinos also peaks around January due to the chanages in atmospheric density resulting from seasonal temperature variations.

2.3.4 Internal and surface backgrounds

Unlike external background which is common to all types of detectors, internal background depends on the target state.
Crystalline detectors as germanium or scintillators are grown from high purity powders or melts. During this process remaining impurities are rejected. In this way, their ionic radius does not necessarily match the space in the crystalline grid. So, the crystal growing process itself reduces internal contaminations, for instance with radium, uranium or thorium (in figure 2.3 are illustrated three examples of radioactive chain that involve these nuclei) [164] [165] [166] [167]. A common problem is that the surface is contaminate with radon decay products. Either α-, β-decays or nuclear recoils associated to the latter can enter the crystals depositing part of its energy. The incomplete collection of the signal results in events close to the region of interest, where nuclear recoils from WIMP interactions are expected. To identify events happening close to the surface, new detector designs have been developed over last years.
Furthermore, cosmic activation of the target or detector surrounding materials before the detector is placed underground must be considered. One of the most important processes in the production of long-lived isotopes is the spallation of nuclei by high energy protons and neutrons. As the absorption of protons in the atmosphere is very efficient neutrons dominate the activation at the Earth's surface for energies below GeV [171]. Exposure time, height above sea level and latitude affect the yield of isotopes, therefore, by minimising the time at surface and avoiding transportation via airplane, the isotope creation can be reduced. Since these precautions can not always be taken, tools of studies targeted to quantify the background due to cosmogenic activation are required (see for exemple [171] [172] [173] [174]).
For noble gases, a contribution to the internal background originates from cosmogenic-activated radioactive isotopes generated in the material. For argon (ex. DarkSide experiment [175]), ^{39}Ar with an endpoint energy, or the maximum energy that these nuclei can reach, at 565 keV has a large contribution to the internal background originated from cosmic-ray activiation at a level of 1 Bq/kg in natural argon. In order to reduce it, argon from underground sources is extracted. In this way, the activity is reduced by a factor of 1/400 [176]. In Xenon, cosmic activation produces also radioactive isotopes, all rather short-lived. ^{127}Xe has the longest lifetime with 36 d which is still short enough to decay within the start of the experiment [177]. Xenon also contains a double beta decaying isotope, ^{136}Xe, however its lifetime is so large, $2.2 \cdot 10^{21}$ y [178], that it doesn't contribute to the background for detectors up to few tons mass. If necessary, this isotope can be removed relatively easily by centrifugation. In addition, decays from

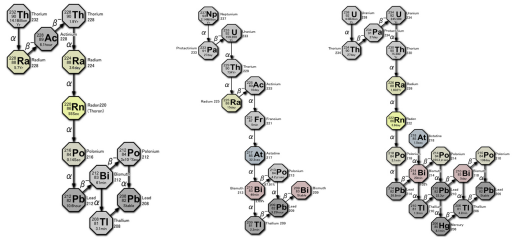

Figure 2.3: Three possible radioactive chains that involve Uranium, Thorium and Radium

the contamination of the target with krypton and the radon emanation from the detector materials contribute to the internal background. The β-decaying isotope ^{85}Kr is produced in nuclear fission and it is released to the atmosphere by nuclear fuel reprocessing plants and in tests nuclear weapons. Krypton can be removed from xenon either by cryogenic distillation [179] or using chromatographic separation. Both methods have been proved to work at the XMASS/XENON and LUX experiments [180] [181], respectively. Besides the reduction of krypton in the target, techniques to determine the remaining krypton contamination are necessary in order to precisely quantify its contribution the remaining contamination. Recently, detections in the ppq (parts per quadrilion) regime of natural Kr in Xe have been achieved [182]. Another possible method is the use of an atom-trap trace-analysis system [183]. Radon is emanated from all detector materials containing traces of uranium ot thorium. Once radon is produced in these decay chains, it slowly diffuses througout the material and can be then dissolved in the liquid target. An approach to reduce radon is to use materials with low radon emanation [184] [185]. Furthermore, methods to continuosly remove the emanated radon are being investigated [186] [187] [188].
For both solids and liquids, the characteristics of the surface are very important. For exemple, radium accumulated at the surfaces of the target or in the materials in contact with the liquid can contribute to the background i.e. surfaces background and radon emanation. Surface treatment with acid cleaning and electropolishing have been proven to be effective in removing radioactive contaminants at the surfaces [189].

Chapter 3

XENON experiment at LNGS

Among the various experimental strategies for direct detection of WIMPs, detectors using liquid Xenon are currently the most sensitive. This is the case of the experiments realized by the XENON collaboration [190].
Initilally the aim was the realization of a two-phase detector with liquid and gaseous Xenon, on the kg scale [192]. However the results obtained in 2007 favored the design of a larger detector, XENON100 [193], with the same operating principle. Both detectors were placed in the interferometric tunnel at the Gran Sasso National Laboratories (LNGS) under a 1400 m layer of rock. The following phase of the project was XENON1T [194] [195], which redueced significantly the background noise and with a target mass 30 times greater. To further improve sensitivity and possibly confirm the results, the collaboration is working on a new phase of the project: XENONnT [213]. The construction of this new detector began in 2019 and is expected to be completed by the fall of 2020. The first test runs are expected to start before the end of this year, probably in October. This experiment is the main topic of this thesis work, in particular the Neutron Veto, which will be discussed in detail in chapters 4 and 5.

3.1 Xenon properties

Detectors of XENON project are made with a double phase Time Projection Chamber (TPC), containing Xenon in both the liquid phase (LXe) and in Gaseous one (GXe) [190]. The choice of LXe as an active target for direct detection of Dark Matter presents many advantages such as:

• Emission of $5{\cdot}10^4$ photons with $\lambda = 177.6$ nm and creation of $6{\cdot}10^4$ electron-ion pairs per MeV "trasmitted" to Xenon nuclei by scattering with other

particles. The experiment mainly exploit this property by simultaneously measuring the ionization and scintillation signals from elastic interactions, and from these it identifies the nature of the particle, discriminating between WIMP and background events.

• Transparence to its own scintillation light and high mobility of ionization electrons in the medium, so it is possible their drift and the measurement of all the charge signal when an external electric field is applied [7]

• Shielding from external noise sources thanks to the large athomic number (Z = 54) and the high density ($\rho \approx 2.86\ g/cm^3$), so the outer regions of the xenon volume absorb much of the external γ radiation, leaving the inner volume with a strongly reduced background [7].

• Optimization of the interaction rate thanks to the dependence of the cross section from A^2

• Presence of predominantly stable isotopes and isotopes with non-zero spin which allows studying the cross section dependence on spin

• Higher condensing temperature than other noble gases

• Scalability, thanks to which the expected WIMP interaction rate increases linearly with the target mass and there is a reduction of the run time required to achieve a given sensitivity

Natural Xenon has nine stable isotopes and two of them (^{129}Xe and ^{131}Xe) have odd spin component. A summary of the various isotopes of Xenon, their abundances and their half-lives is shown in Table 3.1 [17] [18]. Thanks to this property it is possible to detect spin-dependent interactions of dark matter particles. Furthermore, Xenon is the second element (the first is Tin) with most stable isotopes and has no long-lived radioisotopes, besides ^{136}Xe, which undergoes double beta decay (half life of $2.17 \cdot 10^{21} y$) [19]. The second longest-lived radioisotope is ^{127}Xe with a half-life of 36.3 d. The absence of intrinsic radioactivity from xenon isotopes is one of the properties that makes this noble gas the best choice as a detection medium for rare events experiments.
Figure 3.1 illustrates the phase diagram of Xenon.

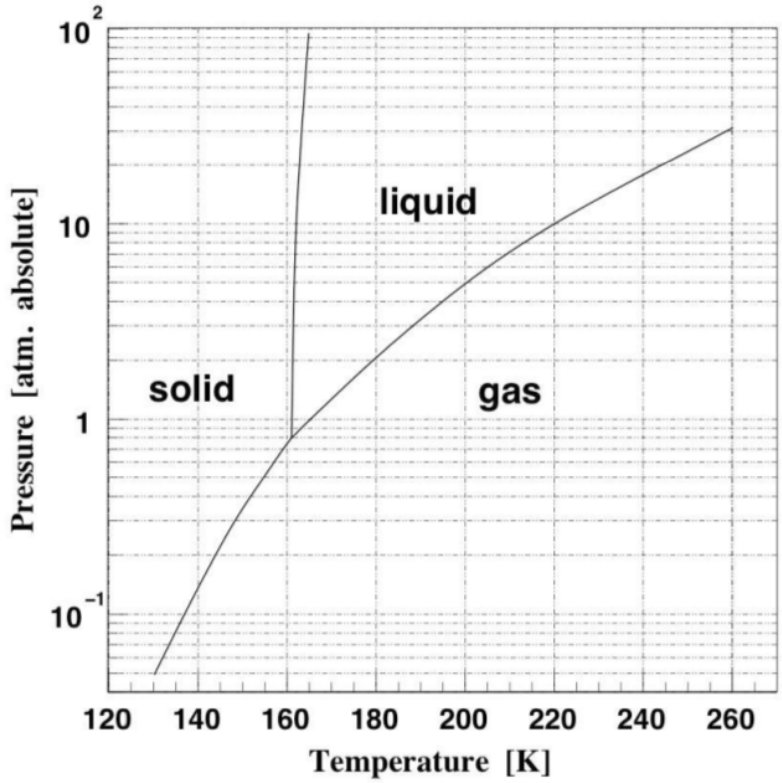

Figure 3.1: Phase diagram of the Xenon element

Isotope	Natural abundance	Half-life
^{124}Xe	0.10 %	$1.8 \cdot 10^{22}$ years
^{125}Xe	synthetic	16.9 hours
^{126}Xe	0.09 %	36.4 days
^{127}Xe	synthetic	stable
^{128}Xe	1.91 %	stable
^{129}Xe	26.4 %	stable
^{130}Xe	4.08 %	stable
^{131}Xe	21.2 %	stable
^{132}Xe	26.9 %	stable
^{133}Xe	synthetic	5.24 days
^{134}Xe	10.4 %	stable
^{135}Xe	synthetic	9.10 hours
^{136}Xe	8.9 %	$2.36 \cdot 10^{21}$ years

Table 3.1: Natural abundances and half-lives of Xenon isotopes

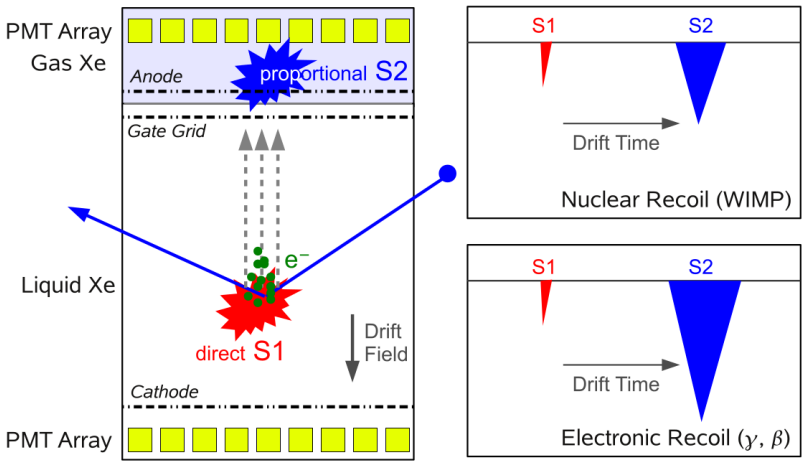

Figure 3.2: Left: working principle of a dual phase TPC. Right: waveform of a NR event (top) and ER event (bottom), whose S2/S1 ratio is the basis for event tipology separation. This separation can also be useful for the rejection of background events.

3.2 The dual phase Time Projection Chamber (TPC)

For a dark matter direct search detector an essential feature is the presence of a dual-phase TPC (liquid and gaseous phase), mostly filled by noble liquids, in this case Xenon, and a smaller layer of noble gas in the top part. In Figure 3.2 is illustrated a schematic view of the Xenon dual phase TPC.
A particle can interact with the liquid Xenon (LXe) target in two ways: through scattering off the Xenon nuclei (neutrons or WIMP particles), also called nuclear recoil NR, or off the atomic electrons (γ rays or electrons), also called electron recoil ER. The recoils produce excitation and ionization of the nucleus (with the possibility of subsequent recombination), in case of NR part of the energy goes into heat; the partition into different channels depends on the type of the recoil and so it is possible to discriminate between nuclear and electron recoil. The resulting scintillation signal from excitation and recombination is called direct, or primary signal (S1). An electric field is applied across the LXe volume, drifting the ionization electrons surviving the recombination away from the interaction site. Electrons which reach the liquid-gas interface are extracted into the Xenon gas, where a stronger electric field of $\geq$ 10.3 kV/cm is generated between the gate at ground potential and the positively biased anode and cause an avalanche of several

hundred electrons. Then, at lower strength of the electric field, the multiplied electrons that collide with xenon nuclei excite the atoms, and consequently there is an emission of linear electroluminescence (linear means that there is a linear dependence between the number of de-excited electrons and the number of photons emitted) with a gain factor of approximately 5 photons per electron. The produced scintillation light is called secondary, or proportional scintillation signal (S2).
In both the signals, S1 and S2, the scintillation light comes from the de-excitation of Xe_2^* dimers. A detailed description of the Xe_2 molecule and its energy levels is given in [20]. The TPC is arranged by a top and a bottom array of PMTs, in direct contact with GXe and LXe, respectively. LXe has a higher index of refraction than GXe (n = 1.69 [21]), so it happens that the direct scintillation will undergo total internal reflection at the liquid-gas interface, then it is mostly detected by the bottom PMT array.
The vertex of the interaction can be 3-dimensionally reconstructed. The (x - y) position is reconstructed by the pattern distribution of the proportional scintillation in the PMT array. Since the S2 signal is generated at a well defined spot in the liquid-gas interface, very close to the top PMT array, the light is collected here by few PMTs while it is more homogeneously distributed over the bottom PMT array; then, in order to improve the position resolution to some millimeters, it is preferable to consider the signal from the bottom array only, that we call S2b . The z coordinate (along the drift field) is obtained from the time difference between the signals S1 and S2, provided the electron drift velocity in the liquids is known with about an uncertain of few %.

3.3 The problem of background signal

Background events are the main problem in direct detection of Dark Matter [190]. To obtain precise measurement for the cross section of the WIMP-Nuclei interaction it is necessary to reduce and, where possible, eliminate all possible sources of background signals. There are essentially three types of background [7]:

• **internal background** : this background is caused by the radioactivity contained in the materials used for building the detector; it mostly induces ER. It essentially consists of γ rays by ^{238}U, ^{232}Th, ^{40}K and ^{60}Co decay chains. It is reduced by suitably choosing the materials used for the construction of the TPC, or by choosing materials with a low content of radiative components of the type mentioned. Steel is mainly chosen. Furthermore, most of the

materials which are in contact with the Xenon, namely all component of the TPC, the inner vessel of the cryostat and the connection pipes, the cryogenic and purification system were additionally selected for a low ^{222}Rn emanation rate. Screening facilities [22] are used to measure the intrinsic background and predict the overall rate.

• **intrinsic background** : is caused by Xenon contamination from the radioactive ^{85}Kr. In fact, Krypton has an isotropical abundance of $^{85}Kr/^{nat}Kr \sim 10^{-11}$ and decays via beta-decay with an endpoint of 687 keV and with a half-life of 10.76 y. Commercial xenon gas is caracterized by a concentration of ^{nat}Kr at the ppm level. As an example, for the ^{85}Kr induced background to be subdominant it was necessary to reach a concentration in XENON1T of $^{nat}Kr/Xe \sim 0.36 \pm 0.06$ ppt (part per trillion) [23]. The Kr concentration in xenon is reduced by using a distillation system that takes advantage of the different boiling temperature of xenon and krypton (respectively 165 k and 120 K at 1 atm). The volatile Kr is collected at the top of the distillation column, while the Kr-depleted xenon at the bottom.
In conclusion, considered as background, ^{85}Kr is source of ER events.

• **external background** : is caused by the radioactivity coming from the rock and the muon-induced neutrons; they mostly induce NR. A shield of water can be used to suppress the neutron and gamma flux coming from the rock radioactivity.

XENON1T experiment boasts the achievement of the lowest noise level; with the XENONnT upgrade we want to achieve the required background reduction. While it is possible keep under control the background due to ER events, the background due to neutrons (NR events) is not negligible also when the fiducial volume is increased. In fact, there are some neutrons, called sneaky neutrons, which scatter only once near the surface and then leave the TPC. To further increase sensitivity it is necessary to identify them. For this purpose a Neutron Veto is introduced in parallel with the Muon Veto. Anyway, thanks to the Muon Veto, within a fiducial mass of 1 ton of LXe, it was obtained a background of 0.01 events per year from muon-induced neutrons (as results from Monte Carlo estimates).

3.4 Phases of the project before XENONnT

In this Section are briefly described the detectors gradually implemented in the XENON experiment, with their achieved performance and their reached

background levels. The solutions to increase performance and reduce background are also described. Table 3.2 shows the fiducial mass of the detector and the background level for each phase of the experiment.

Experiment	Fiducial mass (kg)	Background level (events/year)
XENON10	5.4	
XENON100	20	
XENON1T	1000	2.08
XENONnT	4000	1.15

Table 3.2 Fiducial mass of the detector and background level for each phase of XENON experiment.

3.4.1 XENON10

The XENON 10 experiment constituted the first prototype and it was installed in 2005, being active until 2007. It was designed to test the XENON performances and verify achievable energy threshold, background rejection power and sensitivity. The TPC dimensions were 20 cm in diameter and 15 cm in heigh and contained 15 kg of Xenon for a fiducial mass of 5.4 kg. From the analysis of the data collected between October 2006 and February 2007, the upper limit of the WIMP-Nuclei cross section indipendent from spin $8.8 \cdot 10^{-44} cm^2$ was found to be at 90% of the confidence level for WIMP mass of 100 GeV/c^2 and $4.5 \cdot 10^{-44}$ for a mass of 30 GeV/c^2 [192].

3.4.2 XENON100

The second phase of the project, XENON100, began in 2008. Compared to the previous one, the XENON100 detector was made up of 161 kg of LXe for a fiducial mass of 65 kg. The sensitivity was increased by two orders of magnitude with respect to XENON10 thanks to the choice of appropriate materials and to an increase in the shielding LXe. In fact, liquid Xenon has shielding power thanks to its high density, about 3 g/cm^3, or 3 times greater than the density of water. The cryostat consists of two shells: the inner one, where the LXe and TPC are housed, and the outer shell. The two are separated by an insulation vacuum and a super-insulation blanket. The external one acts as a shield for the internal one. Thanks to these improvements, a lower limit was obtained for the cross section of elastic interactions, indipendent of spin, WIMP-nucleus for WIMP mass 50 GeV/c^2 equal to $1.1 \cdot 10^{-45}$ cm^2 (90% of confidence level). For the spin dependent case, it was obtained a minimum of $2.0 \cdot 10^{-40}$ cm^2 in the neutron case and $53 \cdot 10^{-40}$ cm^2 for a WIMP mass of 50 GeV/c^2 in proton case (90% of cconfidence) [193]

Figure 3.3: Representation of XENON1T TPC inside the cryostat (left) and of the XENON1T experimental area in Hall B of the Gran Sasso National Laboratories

3.4.3 XENON1T

XENON1T represents the third phase of the project and was active until January 2019. The detector uses a mass of 3500 kg, of which 2000 kg constitute the active mass. From the Monte Carlo simulations carried out under these conditions, a lower limit was envisaged for the cross section of $1.6 \cdot 10^{-47}\ cm^2$, achievable thanks to a reduction of background events of two orders of magnitude compared to the previous configuration. Another fundamental characteristic acquired in this project is a muon detector (Muon Veto) which consists of a cylindrical structure filled with water and equipped with photomultipliers (PMT). The final results of the XENON1T experiment were presented in 2018. The result did not highlight the presence of events linked to WIMP interaction; nevertheless allowed to set the limit, for the cross section of WIMP-nuclei interactions indipendent from the spin, with minimum at $4.1 \cdot 10^{-47}\ cm^2$ for a WIMP mass of 30 GeV/c^2 at 90% of confidence level. [194] [195]. The characteristics of XENON1T detector are illustrated in Section 4.1

3.5 XENONnT phase

As underlined by the rapid success in the area of direct DM experiments [219] [222] [220] [218] [226], [221] and as mentioned in the previous sections of this chapter, dual-phase LXe TPCs is one of the best performing technologies to

cover the parameter space still unexplored, especially for massive WIMPs. LXe is intrinsically radio-pure, is capable of powerful self-shielding, and is sensitive to low-energy NRs with good energy resolution. The simultaneous detection of both ionization signals even from single electrons together with scintillation signals down to a few keV, enables dual-phase TPCs with 3D position sensitivity making possible the reconstruction of the event position, and so the selection of events taking place on the edge from those happening in the core of fiducial volume (fiducialization). Given the redundant information for each event, surface events and detector artifacts can be eliminated in offine analysis [223]. Particularly attractive is the scalability of a LXe TPC to contain a homogeneous target of several thousand of kilograms. For such large detectors, even neutrons are distinguishable from WIMP-induced NRs due to their interaction multiplicity. This makes LXe TPCs unique in that they potentially allow a positive identification of dark matter-induced signals or, if not, to approach the "plateau" in the parameter space represented by the irreducible neutrino background.

In both cases, an experiment with sensitivity of another order of magnitude higher was necessary to extend the accessible parameter space. XENON1T was built with the ability to increase its sensitive target, further reducing the background from intrinsic sources. With XENON1T working as designed, the Collaboration decided to pursue this detector upgrade, called XENONnT [213]. XENONnT started by mid-2019, ahead of other experiments at similar scale [217]. The expected XENONnT sensitivity is shown in Figure 3.4. XENONnT has a solid potential to be the first DM experiment to detect NRs from coherent neutrino-nucleus scattering [215]. Although an interesting signal in its own right, these events represent an irreducible background to the DM search because this signal is indistinguishable from a signal eventually produced by the DM scattering. Neverthless, as shown in Figure 3.4, these background should limit the sensitivity to very light WIMPs and do not impede the potential of XENONnT to probe the most relevant WIMP-mass range.

XENONnT was designed with the vision to enable a new inner detector meaningfully larger than the previous ones, in the same water shield and serviced by the same systems and infrastructures. The increased target mass, together with a further reduction in intrinsic background, mainly achieved by active Rn-removal, improved detector/veto design and more efficient self-shielding, will allow an order of magnitude improvement in sensitivity, expanding the physics reach and discovery potential of the XENON program, ahead of competition.

The XENONnT detector support structure was built for a heavier TPC to be placed in the same cryostat, replacing just the inner vessel. Similarly,

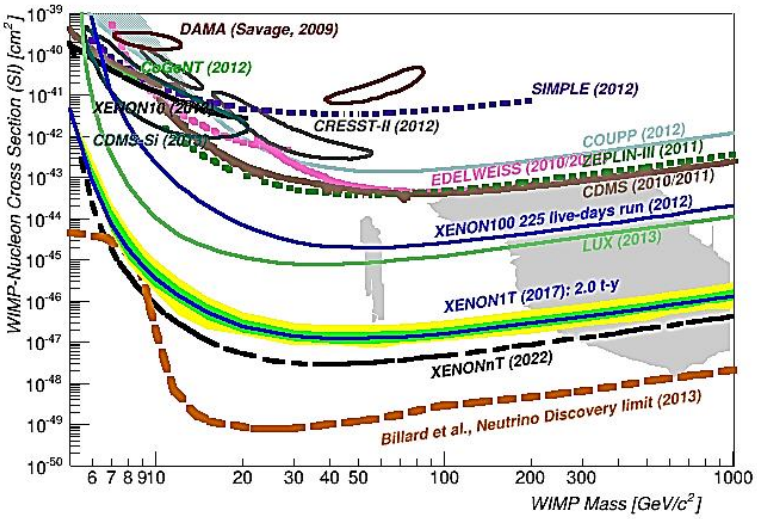

Figure 3.4: The expected sensitivity of XENONnT for spin-independent WIMP-nucleon interactions is shown, together with the finally results from XENON1T (2.0 t·y) [226] and other experiments.

the Xenon cryogenics and purification systems as well as the recovery system were designed to handle a target mass scale-up to about 8 tons of LXe of which 6.0 tons are active. The design of XENONnT follow closely that of the old one, with a modest 0.4 scale-up in diameter and drift lenght. The new TPC is described in subsection 4.2.2.
Three new systems are installed to achieve the required background reduction compared to XENON1T. The first is an online Rn removal system, which is based on XENON ground-breaking distillation technology as for removing the krypton from Xenon, but in a "reverse mode". The achievable reduction in the Rn concentration due to the sources inside the cryostat depends essentially only on the purification cycle time with respect to the Rn lifetime, that is, on being able to remove the Rn faster than it can decay. It is therefore highly beneficial to have an online Rn removal system installed on a fast purification loop such as that of the cryogenic LXe purification system. The structure of the cryostat and the cryogenic purification system will be discussed in more detail in Chapter 4.
The second new system is a veto detector to tag neutrons which first scatter inside then exit the TPC, so producing a single-scatter nuclear recoil signal. The Neutron Veto is realized using water doped with gadolinium and is equipped with 120 additional photomultipliers placed 1 meter from the cryostat on an approximately cylindrical surface, with reflective foils of TPFE that

optically limit the light collection region, placed behind the PMTs. The details of the design and performance are discussed in Chapter 4.
A third new system is an additional storage system for the large amount of Xenon used in XENONnT physics program. This system has been operative since mid 2019, after a period of intergation and commissioning of about 6 months. The fast-paced schedule, outlined in detail in Chapter 4, is based on our expereience with XENONnT phase.
The fast upgrade to XENONnT allow the XENON program to lead the direct detection field in the next few years with a sensitivity to dark matter cross sections down to 10^{-48} cm^2. Figure 3.4 shows, as function of calendar year, the projected sensitivities to spin-indipendent WIMP-nucleon interactions for a $50GeV/c^2$ WIMP. The time scale assumes an 80% livetime fraction for all experiments. For XENONnT, we refer to the schedule described in details in Chapter 4.
For XENONnT and LZ [214], it is reported in Table 3.3 the values assumed for the various parameters. The dominant background comes from internal sources ^{85}Kr and ^{222}Rn. For XENONnT, levels of ^{222}Rn and ^{85}Kr of $1\mu Bq/kg$ and 0.02 ppt of $^{nat}Kr/Xe$ are required. The ^{222}Rd requirements is achieved by the online radon reduction tecnique and by improving the cleanroom used for assembly, to reduce contributions from particulates. Combined with the emanation studies performed in-situ (before filling the TPC) and dedicated studies, XENON collaboration has identified strategies to further reduce the impact of radon (see Chapter 4). As far as ^{85}Kr is concerned, operations of distillation of the column has demonstrated the capability to efficiently reduce krypton down to $^{nat}Kr/Xe < 48$ ppq (parts-per-quadrilion, 10^{-15}) at 90% confidence level. [228].

	XENONnT	LZ
Fiducial volume (tons)	4	5.6
Exposure (ton · year)	20	15
Livetime fraction	80%	80%
WIMP E_{range} (keV_{nr})	4-50	6-30
NR Acceptance	40%	50%
ER rejection	99.75%	99.5%
Bkg rate (evt/year)	1.15	2.35

Table 3.3: Assumptions for the projected sensitivity to spin-independent interaction shown in Figure 3.4. The background rate is defined as the rate of NR and ER falling into the defined WIMP search box, after having accounted for acceptance and rejection, respectively. Numbers for LZ are the "goal" values extracted from [231].

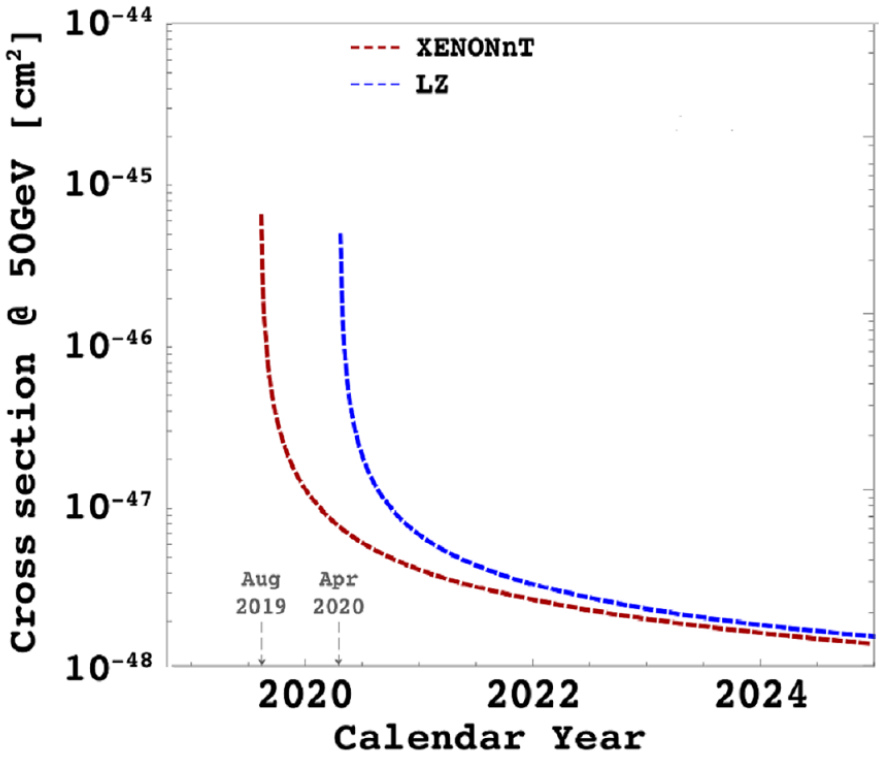

Figure 3.5: A comparison, as function of calendar year, of the projected sensitivity to spin independent WIMP-nucleon interactions for a $50 GeV/c^2$ WIMP for XENONnT (4 ton fiducial mass), and LZ (5.6 ton fiducial mass). Curves in this plot have been calculated using the official values that each experiment has estimated for WIMP energy range, NR acceptance, ER rejection and background. See text for comments on the comparison of the various curves.

Chapter 4

The detector

This chapter describes the detector in detail. We start from the descrition of the cryostat and the TPC, at first we described as they were structured in XENON1T and then the improvements made to them in XENONnT are discussed. Then, we briefly described the Muon Veto, which has not undergone essentially changes in the upgrade from XENON1T to XENONnT, and finally we described the Neutron Veto, absent in XENON1T and introduced only in XENONnT.

4.1 Cryostat and TPC in XENON1T

The XENON1T dual phase TPC was installed inside a double-walled vacuum cryostat, in the center of a large water tank. The water tank served a passive shield as well as a Cerenkov muon veto. A three-floor building accomodated all auxiliary systems (see next subsections for details) [195]

4.1.1 Time projection chamber

This subsection describes the design of XENON1T TPC, the photomultipliers (PMTs) and the systems that handle the $\sim$ 3.2 t of xenon in double-phase form. All materials and components constituting the TPC were selected for a low intrinsic radioactivity.
The cylindrical TPC was 97 cm in lenght and 96 cm in diameter and contained an active LXe target of 2.0 t, in which the light and the charge signals from each interaction were detected, see figure 4.1. There were 24 interlocking and light-tight PTFE (polytetrafluoroethilene, Teflon) panels which enclose TPC; their surfaces were treated with diamond tools in order to optimize the reflectivity for vacuum ultraviolet (VUV) light [198]. Thanks to the rather

large linear thermal expansion coefficient of PTFE, its length was reduced by about 1.5% at -96 °C, the operation temperature. An interlocking design allowed the radial dimension to remain constant while the vertical lenght was reduced.
To ensure the omogeneity of drift field, the TPC was surrounded by 74 field shaping electrodes, connected by two redundant chains of 5 $G\Omega$ resistors that connected each chain to the cathode. The resistor settings, as well as the electrical transparency of the TPC electrodes (gate, anode and screening electrode on top, and cathode and screening electrode on bottom), were optimized by means of electrostatic simulations, using finite element (COMSOL Multiphysics [199]) and boundary element methods (KEMField [200]). Figure 4.1 shows the high voltage configuration realized during science run 0. As already mentioned in Chapter3, there are two types of signals, S1 and S2, produced the first in the liquid phase of the Xenon, the second in the gaseous one. Most S1 light is detected by the photosensors below the target. The electrodes were thus designed for S1 light collection by optimizing the optical transparency of the gate, the cathode and the bottom screening electrodes. The details are summarized in table 4.1. The circular stainless-steel frames supporting the electrodes were electropolished and optimized for high-voltage operation. The etched meshes were spot-welded to the frames, while the single wires were pre-stretched on an external structure and fixed by wedging them between the upper and lower parts of the frames. Gold-plated wires were used to increase the work function of the metal.
The cathode was negatively biased using a Heinzinger PNC150000-1NEG high-voltage supply via a custom-made high-voltage feedthrough. The latter consists of a conducting stainless-steel rod inside an ultrahigh molecular weight (UHMW) polyethylene insulator cryofitted into a 25.4 mm diameter stainless-steel tube to make it vacuum tight. Before installation, the feedthrough was successfully tested to voltages exceeding $\sim 100kV$. The total length of the feedthrough was about 1.5 m, out of which 1.2 m were located inside the cryostat. This ensures that the connection point to the PTFE insulated metal rod, which supplies the voltage to the cathode frame, is covered by LXe. The anode was positively biased by a CAEN A1526P unit via a commercial Kapton-insulated cable (Accuglass 26AWG, TYP22-15). The gate electrode was kept at ground potential and the screening electrodes were biased to minimize the field in front of the PMT photocathodes.
A "diving bell" made of stainless steel, directly pressurized by a controlled gas flow, was used to maintain a stable liquid-gas interface between the gate and anode electrodes. It enclosed the top PMT array. The height of the liquid level inside the bell was controlled via a vertically adjustable gas-exhaust tube. Possible tilts of the TPC are measured by means of four custom-made

parallel-plate capacitive level meters installed inside the diving bell. They cover a dynamic range of 10 mm and have a precision of $\sim 30\mu m$. Two cylindrical level meters of 1360 mm length measure the LXe level during filling and recovery from below the cathode to above the bell, with 2 mm precision.

TPC electrode	Type	Material	Wire diameter
Top screen	hex etched	stainless steel	178 μm
Anode	hex etched	stainless steel	178 μm
Gate	hex etched	stainless steel	127 μm
Cathode	parallel wires	Au plated stainless steel	216 μm
Bottom screen	parallel wires	Au plated stainless steel	216 μm

TPC electrode	PichCell opening	Transparency	Position
Top screen	10.2 mm	96.5 %	63 mm
Anode	3.5 mm	89.8 %	5 mm
Gate	3.5 mm	92.7 %	0 mm
Cathode	7.75 mm	97.2 %	-969 mm
Bottom screen	7.75 mm	97.2 %	-1017 mm

Table 4.1 : Specifications of the five TPC electrodes. The bottom screening electrode featured a single wire installed perpendicularly mid-way to all others to minimize elastic deformation of the frame. The last column indicates the vertical position of the electrodes inside the TPC. The distance between the top (bottom) screen to the top (bottom) PMTs was 11 mm (12 mm).

4.1.2 Photomultipliers

A total of 248 Hamamatsu R11410-21PMTs of 76.2 mm diameter were used to record the signals from the TPC. They were radially installed in the top array (127PMTs) to facilitate radial position reconstruction, and packed as tightly as possible in the bottom array (121PMTs) to maximize scintillation-light collection efficiency. They had an average quantum efficiency of 34.5% at room temperature and at 178 nm (bialkali-LT photocathode) [201], a high photoelectron collection efficiency of 90% and were designed to operate stably in gaseous and liquid Xenon at cryogenic temperature [202] [203]. The low-radioactivity PMT version was jointly developed by Hamamatsu and the XENON collaboration [204]. Six 25.4 mm square-window Hamamatsu R8520 PMTs, were installed in the LXe region outside of the TPC, next to the upmost field-shaping electrodes, for detector calibration studies [205].

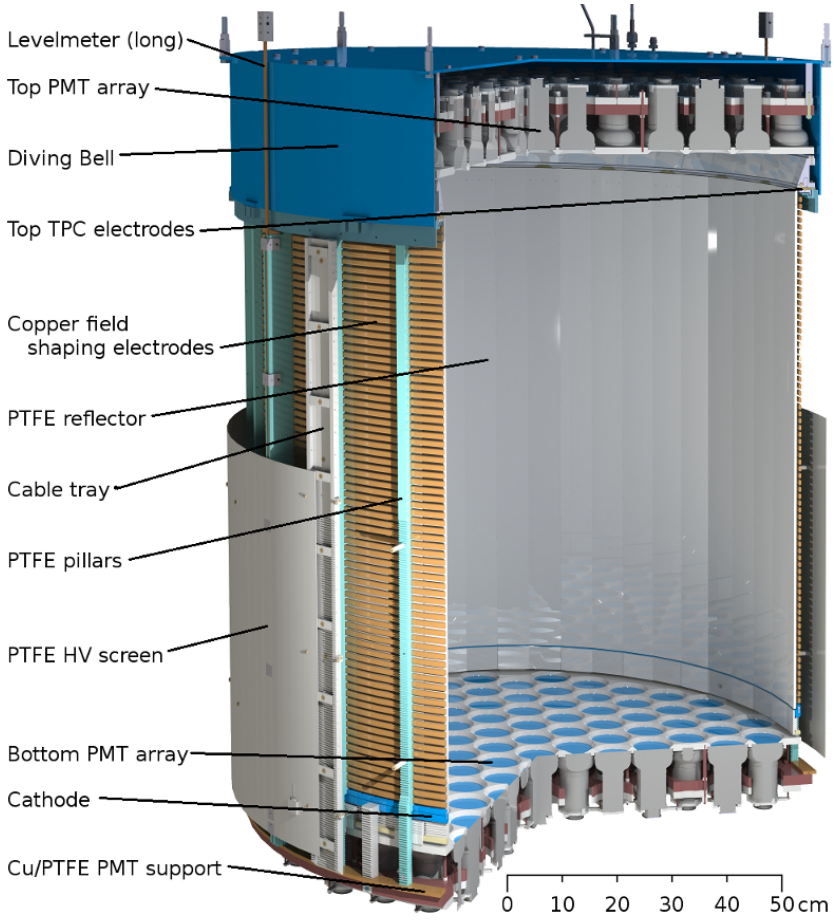

Figure 4.1: Illustration of the XENON1T TPC. It was built from materials selected for their low radioactivity, e.g., OFHC copper, stainless steel and PTFE. The top and bottom PMT arrays were instrumented with 127 and 121 Hamamatsu R11410-21 PMTs, respectively

All installed R11410-21 PMTs were screened for their intrinsic radioactivity levels in batches of typically 15 tubes [204] and tested at room temperature and under gaseous nitrogen atmosphere at $\sim 100C$. All PMTs were subject to at least two cooling cycles prior to installation. A subset of 44 tubes was additionally tested in LXe (2-3 cooling cycles). The PMTs feature a peak-to-valley ratio of ~ 3, a single photoelectron resolution of 27% for gains above $3 \cdot 106$ and a transit time spread (TTS) of 9.1 ± 1.3 ns [201].
Based on the measured performance and the specifications provided by the manufacturer, the PMTs were placed in the two arrays. Both arrays consist of a massive OFHC copper support plate with circular cut-outs for the PMTs. A single PTFE plate holded the individual PMTs and a PTFE reflector-

plate covered the areas between the PMT windows.Both PTFE plates were attached to the copper support in a self-centering way to ensure that all PMTs moved radially inward upon cool-down to LXe temperatures while the support plate, which was connected to the remaining TPC structure, stays in place.

4.1.3 Cryostat and support frame

This subsection describes the XENON1T cryostat, which contained the TPC with the LXe target,and the cryogenic system for gas liquefaction and compensating for heat losses.
The TPC was installed inside a double-walled, cylindrical stainless-steel cryostat made of low-radioactivity material [208].The inner vessel was 1960 mm high and 1100 mm in diameter. Its inner surface, in direct contact with the liquid xenon, was electro-polished in order to reduce the emanation of radon. It was enclosed by an outer vessel of 2490 mm height and 1620 mm diameter, large enough to accomodate the detector of the upgrade stage XENONnT as well. The inner vessel was metal-sealed (Helicoflex) and thermally decoupled from the outer one by polyamid-imid (Torlon) spacers. Thirty layers of superinsulation (RUAG Space Austria) reduced static thermal losses to $\sim 75W$. The cryostat was installed in the center of the water Cherenkov detector (see figure 4.2). The connections to the outside were made through a double-walled cryogenic pipe (406 mm external diameter; 254 mm inner diameter) enclosing all the connections to the cryogenic system (cooling, purification, fast emergency recovery, diving bell pressurization) and the cables for the PMTs and auxiliary sensors. A separate, single-walled pipe carried the high voltage cable to the TPC cathode feed through.

4.1.4 Cooling

XENON1T followed the "remote cooling" which allows for installation of the cryogenic system far away from the TPC, along with maintenance while the detector is in operation. The Xenon gas inside the XENON1T cryostat was liquefied and kept at its operating temperature $T_0 = -96$ °C thanks to a pair of redundant pulse-tube refrigerators (PTRs [209], Iwatani PC-150), each of which provided $\sim 250W$ of cooling power at T_0. Each PTR was connected to a copper cold finger reaching into the xenon volume such that the PTR could be removed without exposing the inner vessel. The PTR insulation volumes were separated such that one PTR could be serviced while the other was in

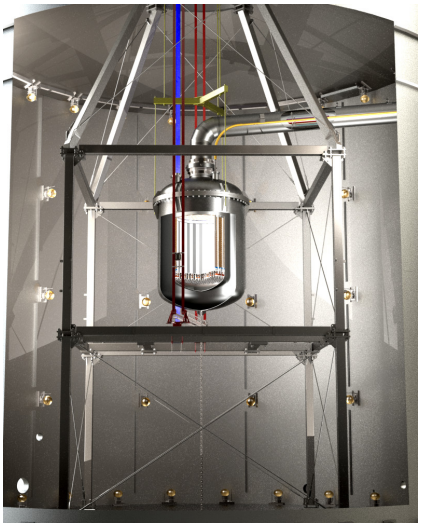

Figure 4.2: The stainless-steel cryostat of XENON1T containing the LXe TPC was installed inside a 740 m^3 water shield equipped with 84 PMTs deployed on the lateral walls. The cryostat was freely suspended (dark yellow) on a stainless-steel support frame, which could be converted into a cleanroom around the cryostat. The cryostat was connected to the outside by means of two pipes. The large, vacuum-insulated cryogenic pipe carried all gas/LXe pipes and cables. A small pipe (yellow) was used for the cathode high-voltage. Also shown is the system for calibrating XENON1T with external sources installed in movable collimators attached to belts (blue, red).

operation. The measured total heat load of the system was 150 W, hence one PTR was sufficient to operate the detector. The xenon pressure inside the cryostat was kept constant by controlling the temperature of the active PTR cold finger using resistive heaters. A proportional integral-derivative (PID) controller (Lakeshore 340) read the temperature at the cold finger and controls the power supplied to the heaters.
The cryogenic system was interfaced with the cryostat through the vacuum-insulated cryogenic pipe. Xenon gas from the inner cryostat vessel streams to the cryogenic system, was liquefied by the PTR, collected in a funnel and flows back to the cryostat vessel, driven by gravity, in a pipe that runs inside the cryogenic tube. Another pipe carried LXe out of the cryostat, evaporated it in a heat changer, and was fed sit to the Xenon purification system. The purified xenon gas was liquefied in the same heat exchanger and flows back to the cryostat. The pipe that carried the purified LXe back to the cryostat was also used during the cryostat filling operation. Figure 4.3 shows a view of the

different components of the XENON1T cryogenic system and its interfaces to other systems.

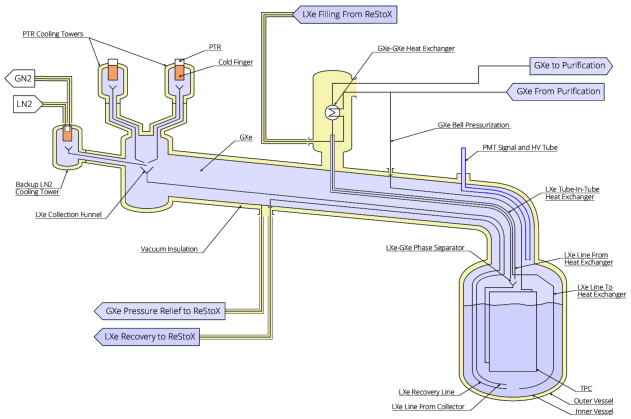

Figure 4.3: The cryogenic system of XENON1T: cooling was provided by means of three redundant cold heads (two pulse-tube refrigerators (PTR),1 LN_2, installed on individual cooling towers located outside of the water shield. The liquefied xenon run back to the main cryostat in a 6 m long vacuum-insulated cryogenic pipe, through which all connections to the TPC were made with the exception of the cathode bias voltage which is not shown in the figure. The connections to the systems for xenon purification and storage (ReStoX) are also shown. Figure not to scale

4.1.5 Xenon purification

While the TPC enclosed a LXe target of 2.0 t, a total of 3.2 t was required to operate the detector. The additional Xenon load was contained in the 60 mm layer between the cathode electrode and the bottom PMTs, in the 58 mm layer between the TPC field-shaping electrodes and the cryostat wall, in between and below the bottom PMTs, in the gas phase and in the gas purification and storage systems described below.
The total Xenon inventory included research-grade gas with a low concentration of impurities, especially natural Kr. The impurity level was measured in sets of four gas bottles by gas chromatography [210]. In case a higher level than specified was detected, the bottles were purified using the distillation system before adding the gas to the storage system.
Electronegative impurities, such as water or oxygen, absorb scintillation light and reduce the number of ionization electrons by capture in electron drift time dependent fashion. These impurities were constantly outgassing

into the xenon from all detector components. Therefore, the gas must be continuously purified to reduce the impurities to the 10^{-9} O_2-equivalent level (ppb). Driven by gas transfer pumps, LXe was extracted from the cryostat its bottom, next to the LXe condensate inlet from the cryogenic system. The LXe was evaporated in a heat exchanger system, made from a concentric tube in combination with a plate heat exchanger, which also cools the return gas from the purification system [211]. It was 96% efficient and reduced the heat input into the cryostat to only 0.39 $W/slpm$ (standard liters per minute).

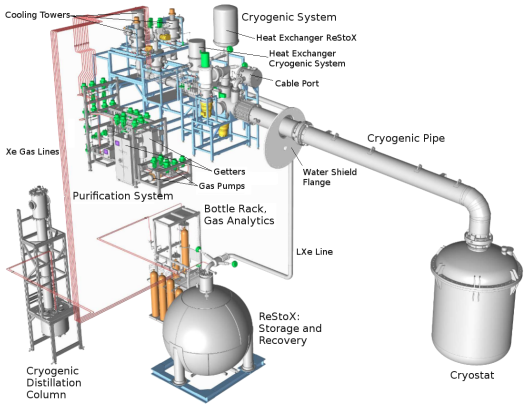

Figure 4.4: The gas-handling system of XENON1T consisted of the cryogenic system (cooling), the purification system (online removal of electronegative impurities), the cryogenic distillation column (natural Kr removal), ReStoX (LXe storage, filling and recovery), the gas bottle rack (injection of gas into the system) and gas analytics station (gas chromatograph). The cryostat inside the water shield accomodated the TPC.

4.1.6 Background Source and suppression

The science goals of XENON1T required an unprecendented low background level [197]. The main background sources are summarized in table 4.2, divided into ER and NR (see Chapter 3). The latter are most significant for the WIMP search, as single-scatter NR signatures from neutrons or neutrinos are indistinguishable from WIMP signals.
Besides background suppression by shielding, material selection and active removal of radioactive isotopes, backgrounds were effectively reduced in the data analysis: multiple scatter signatures are rejected based on the number of S2 peaks, ER-like events were identified based on the events S2/S1 ratio, and external backgrounds, e.g., from radioactive decays in the detector construction

materials or from muon-induced cosmogenic neutrons, were reduced by fiducialization, i.e., the selection of an inner detector region. However, fiducialization was not effective for target-intrinsic sources, such as the noble gases ^{222}Rn and ^{85}Kr, or the two-neutrino double-beta decay ($2\nu\beta\beta$) of ^{136}Xe $T_{1/2} = 2.17 \cdot 10^{21}y$ [212] with a 8.9% abundance in ^{nat}Xe). It is also not effective for solar neutrino-induced backgrounds.

Background Source	Type	Rate	Mitigation Approach
^{222}Rn (10 $\mu Bq/kg$)	ER	620	m.s from Rn-emanation - ER rej.
solar pp and ^{7}Be νs	ER	36	ER rej.
^{85}Kr (0.2 ppt of ^{nat}Kr)	31	4-50	cryogenic distillation; ER rej.
2 $\nu\beta\beta$ of ^{136}Xe	ER	9	mat sel., ER m.scat. rej., fiducialization
Radiogenic ν	NR	0.55	mat.sel., m.scat. rej., fiducialization
CNNS (mainly solar ^{8}B-ν)	NR	0.6	-
Muon-induced neutrons	NR	< 0.01	act.Cerenkov veto; m.scat. rej., fid.

Table 4.2: Summary of the sources contributing to the background of XENON1T in a fiducial target of 1.0 t and a NR energy region from 4 to 50 keV (corresponding to 1 to 12 keV ER equivalent). The expected rates are taken from the Monte Carlo simulation-based study [197] and assume no ER rejection. CNNS stands for "coherent neutrino nucleus scattering"

4.2 Cryostat and TPC upgrades in XENONnT

4.2.1 Cryostat

In XENONnT, TPC was dimensioned to use the XENON1T outer cryostat vessel 30 cm higher compared to its XENON1T version, in order to allow for a fast upgrade of the detector and maximize the use of systems already built and operative [213]. In particular, the cryogenics pipe connecting the detector to the subsystems (e.g., cryogenics, purification, DAQ) in the XENON building, remain in place. The new inner cryostat vessel hosts a total Xenon mass of about 8 t, with an active, instrumented mass of about 6 t. Figure 4.5 shows the design of the new inner vessel. It has a height of 1.87 m and a 1.46 m inner diameter. It has been attached to the already existing outer-vessel dome through three dedicated support wings. These are designed to maximize the inner vessel's diameter. To minimize background, the wall is made of 5 mm thick, low-radioactivity stainless steel (SS). Samples of steel from various suppliers were screened. As in XENON1T, a HELICOFLEX [232] spring-energized seal is used and ensure vacuum integrity.

The cryostat's inner and outer vessels feature a vacuum-insulated liquid Xenon feedthrough that serve as a liquid connection to the cryogenic LXe purification system to be located on the ground floor next to the XENON building, through a vacuum-insulated pipe that bring the LXe out of the water shield. The addition of this extra port represents the only modification on the existing outer vessel. The dome of the inner vessel is equipped with several flanges corresponding to those already present on the flange of the outer vessel. These are dedicated to liquid filling from ReStoX, gaseous Xe purification, signal and high voltage cable routing, and for the high voltage feedthrough. While the signal and high voltage cables for about 150 additional PMTs have been installed in the cryogenic pipe already, the cables for another $\sim$ 100 channels have been then added for XENONnT. A 40 mm diameter single-wall pipe has been added to one unused flange on the cryostat, to route the extra cables to the XENON building. The pipe has been mechanically decoupled from the existing system thanks to flexible bellows and will run in parallel to the cryogenics pipe.
The structure installed in the water shield which was supporting the XENON1T cryostat support also the XENONnT detector and thus does not require any modification. In order to allow for leveling the TPC the cryostat is suspended on three threaded rods, whose diameter have been increased from M20 to M24.

4.2.2 Time projection chamber

The design of the XENONnT TPC, shown in Fig. 4.6, follows the XENON1T one and implements a few new technical solutions aiming to address some of the issues observed during the XENON1T operations [230]. It maintains a similar aspect ratio as the XENON1T TPC which has proven to be optimal for light collection efficiency. The active volume is laterally defined by thin PTFE panels, arranged in an interlocking polygonal geometry to compensate for thermal contraction. The lateral PTFE walls form a cylinder with approximately 1340 mm in diameter. The active volume of 6.0 t of LXe is instrumented with 476 R11410-21 Hamamatsu 3" PMTs, assembled in two arrays of 223 (top) and 253 (bottom), to detect both primary and secondary Xe scintillation light. The cathode grid and gate mesh delimit a 1500 mm long drift region, surrounded by copper field shaping rings placed behind the PTFE reflector to ensure a uniform electric drift field. As in XENON1T, electron extraction and electroluminescence are achieved by means of an anode electrode, located 5 mm above the gate electrode and 2.5 mm above the liquid/gas interface. Additional TPC electrodes are located in front of the two PMT arrays to screen them from the electric field. Twenty-four vertical pillars, made of

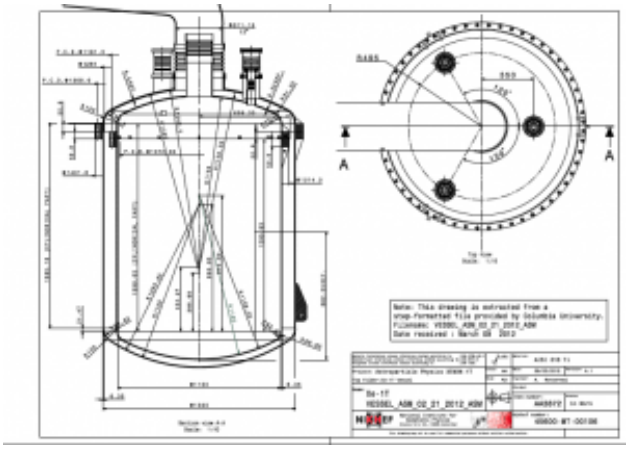

Figure 4.5: Technical drawing of the two-vessel cryostat system. The outer vessel has been reused from the XENON1T phase, the inner one has been constructed for XENONnT. The flange "HV Xenon1T" is used for the new single-wall cable pipe to route extra PMT cables to the counting room.

non-conduting material such as Torlon (PAI) or PEEK, are used to provide structural stability and to interlock the various components of the TPC. The liquid level between gate and anode is kept at a constant and well-definde level by means of a diving bell that, as in XENON1T, encloses the top PMT array.
In order to guarantee full electron extraction at the liquid/gas interface, the anode and the gate electrodes are maintained at +5 kV and ground, respectively. The cathode will be negatively biased to operate the TPC at a nominal electric field of a few hundred V/cm. Successfull operation of XENON1T indicated that the "typical" field requirements could be relaxed, allowing to bias the cathode at about -30 kV to achieve an electric field of about 200 V/cm. The optimization of the TPC's high voltage divider chain for lower (and easier achievable) bias voltages reduce the effects of fiels distorsion as already observed in XENON1T [230]. The same high voltage (HV) feedthrough developed for XENON1T, with low-radioactivity SS tubing and ultra-high-moleculat-weight polyethilene, is re-used fot XENONnT.
For the TPC electrodes for XENONnT, we follow the succesful implementation of the XENON1T ones. Due to the larger diameter of the electrodes and thus more stringent mechanicals requirements, the design of electrode support frames with wires or meshes has been optimized before manufacturing. In order to achieve a higher cathode voltage performance of different combinations of wires and treatments (e.g. electro-polishing, surface treatments) is studied in dedicated Lxe setups to minimize the risk of discharges.

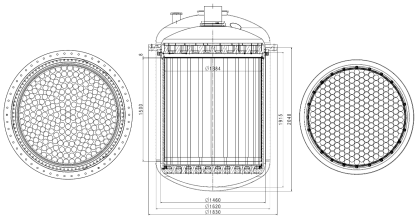

Figure 4.6: Technical drawing of the XENONnT TPC, installed inside the new inner cryostat vessel. It largely follows the successful XENON1T design and improves the known shortcomings. The primary and secondary scintillation signals are observed by a total of 476 Hamamatsu R11410-21 PMTs, installed in arrays above (left) and below (right) the active target.

4.2.3 Material Selection and cleanliness

The material selection and screening campaign has started using the collaboration's HPGe spectrometers operated at three underground locations (LNGS, Vue-des-Alpes at 620 m.w.e. and in a shallow depth lab at MPIK Heidelberg). The overall γ-screening capacity has been enlarged compared to XENON1T. First groups of materials suitable for the construction of the TPC and the inner cryostat have been identified and the campaign to screen PMTs and to find more low-background materials is ongoing. Our capacity for Rn-emanation measurements has been increased considerably with the development of the Auto-Ema at MPIK, which allows for an automated emanation measurement and features two new emanation vessels. All γ-screening and Rn-emanation activities, together with the efforts to reduce material outgassing, Rn-mitigation, surface cleaning and offline analytics (RGMS, GC, APIX, etc.) have been pursued within the newly established Cleanliness working group.
The XENON cleanrooms for TPC construction, assembly and installation have also been upgraded in order to achieve the stringent background requirements. The already existing (class ISO6) cleanroom, installed aboveground in Lab2, remain essential to clean all components according to the specifications, using solvents, acids, detegents etc. The removable $4.5 \cdot 4.5\ m^2$ cleanroom around the cryostat in the water shield has been upgraded with hard walls and a proper cleanroom floor, to improve its performance. A new cleanroom is required underground, next to the XENON water shield door, to assemble the new TPC. It features a Rn-abatement system to minimize plate-out for ^{222}Rn progenies on the TPC walls. The same system also supply Rn-free air to the cleanroom inside the water shield. Using well-established procedures from XENON1T, the TPC has been transported safely, protected by a Rn-tight enclosure and kept under N_2 atmosphere.

4.2.4 Purification system upgrade

The time required for removing impurities from the LXe is increased due to the larger volume of LXe to be purified. In order to reduce the time scale to achieve the required electron lifetime of at least 1 ms, two upgrades have been made to the purification system: 1) replacement of the gas circulation pumps and associated components to enable higher gas flow; 2) implementation of a liquid purification system.

Gas-phase purification

The QDrive pumps on the already existing gas purification system have been replaced with pumps with more stable long term performance and lower radon emanation. These magnetic piston pumps are custom-built based on the successful design used in the EXO-200 experiment [233]. The pumps use a permanent magnet welded in an ultra-pure stainless steel cylinder to serve as a piston, driven by an external ring-magnet outside of the cylinder. Only very clean materials are in contact with the Xenon gas, allowing for a low radon emanation, and the motion is very simple, resulting in a stable performance with maintenance intervals longer than a year. For XENONnT, a scaled-up version of the pump is needed to reach the pressure and flow requirements. In collaboration with nEXO members at Stanford, two prototypes were developed and tested. Recent tests have validated the new pump performance, achieving the required differential pressure of 1.3 bar at a flow rate of 120 Standard Liter Per Minute (SLPM) with an inlet pressure of 1.4 bar. In addition, the tubing and the valves in the main flow path of the purification system have been upgraded to a larger diameter, and to models with larger orifices in the case of the valves, to reduce the flow resistance and increase the maximum achievable purification speed.

Liquid-phase purification

In order to purify the $\sim$ 8 t of Xenon in a reasonable time, the gas-phase purification may not be sufficient. A preliminary analysis of the time evolution of the concentration of electronegative impurities in XENON1T indicated that the majority of impurities are being released directly in the liquid phase, while the gaseous volume above the liquid can be cleaned relatively much faster. At a time much longer than the purification cycle time, the impurity concentration in the active liquid volume is proportional to the rate

of release of impurities and inversely proportional to the purification speed. The much larger density of LXe compared to that of gaseous Xe, by a factor of about 200, means that we can dramatically increase the purification speed by adopting a liquid circulation system, employing an appropriate cryogenic filtering technology. This yield a much shorter initial purification time to reach nominal operating conditions.

The cryogenic liquid purification system was designed to operate in parallel with the gas one. It is installed outside of the water shield on the ground floor next to the XENON building (see Fig. 4.7, and is composed of a cryogenic liquid pump and two custom-made redundant filter units, installed in independent vacuum-insulated enclosures to allow in-situ regeneration or replacement of one unit while the other is operational (see Fig. 4.8. Fig. **??** shows the entire cryogenic system in its final version. The cryogenic liquid pump selected is commercially available [234], satisfies the multiple requirements of the experiment: cleanliness, efficiency, low heat influx, and liquid flow rate of several liters per minute; and has been used by large volume liquid argon and liquid Xenon experiments [235] [236] A single vacuum insulated tube provides liquid flow from the cryostat to the cryogenic purification system while an existing tube in the cryostat cryopipe is used for the liquid return path. Specifically, the XENON1T LXe recovery tube between the cryostat and ReStoX is re-purposed as a liquid return to the cryostat, minimizing the modifications required on the existing cryogenic infrastructure and simplifying the new cryostat design. This design choice also has the added benefut of simplifying the XENONnT LXe recovery procedure compared to that of XENON1T.

ReStox is an original cryogenic system designed for experiments that make use of high quantities of liquid Xenon. It allows to store the total amount of Xenon in gaseous or liquid phase and to fill into the detector vessel under high purity conditions. This system will be described in more detail in next section.

Several materials capable of trapping electronegative impurities at cryogenic temperatures [237] [236] [238] have been tested in a dedicated purity monitor and cryogenic liquid Xenon purification test facility at Columbia University. One technology (see e.g., [238], [239]) that appears promising for a low background experiment to permanently capture oxygen, by far the most prevalent electronegative impurity in LXe detectors, is based on the oxidation reaction $2Cu + O_2 \rightarrow 2CuO$. Using copper as a filter material allows regeneration through the reduction reaction $CuO+H_2 \rightarrow Cu+H_2O$, typically by flowing an Argon/Hydrogen mixture through the filter. Some tests have been carried out for the optimization of the filter geometry, filter material, filter mass and other parameters for the final XENONnT system.

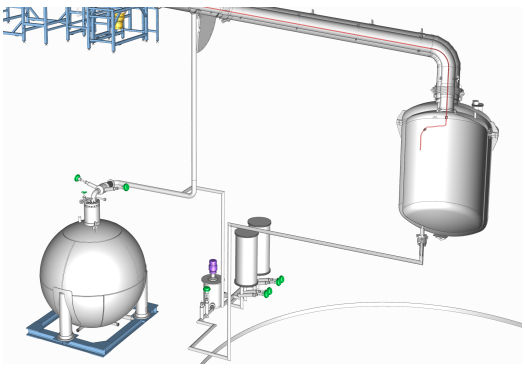

Figure 4.7: Integration of the cryogenic liquid purification system (bottom, center) with the existing cryogenic infrastructure: cryostat (right), ReStoX (left), cryogenic system (top)

4.2.5 Radon Mitigation Strategies

The background induced by dissolved ^{222}Rn in XENONnT is reduced by a factor 10 with respect to XENON1T. This is achieved by a combination of several complementary ^{222}Rn mitigation strategies.

Radon Sources and possibility for Radon Removal

The best strategy to reduce ^{222}Rn-induced background is to avoid ^{222}Rn sources as much as possible. This can only be achieved by a thorough screening of all materials in contact with the liquid xenon. For this purpose, the radon screening facilities at MPIK were significantly upgraded. Two new large-volume emanation vessels were purchased to enhance our ability to measure several samples simultaneously. More importantly, we developed a fully automated emanation system (Auto-Ema) able to extract, purify and concentrate radon from samples completely self-acting. Auto-Ema allows more samples to be processed in a given time and the reproducibility of the results is also improved. The effort to avoid ^{222}Rn sources right from the beginning is accompanied by measures to reduce surface contaminations as much as possible. This does not only imply working in a dust-free environment, but also the application of dedicated surface cleaning procedures and more sophisticated approaches like surface coating with a clean ^{222}Rn barrier.

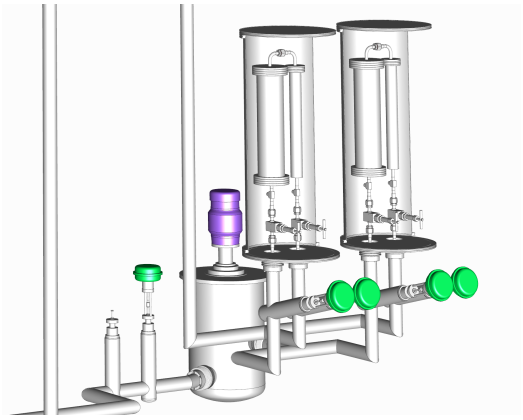

Figure 4.8: Design of the cryogenic liquid purification system. A cryogenic liquid pump (motor shown in purple) circulates the LXe from the cryostat through a pair of redundant cryogenic filters in independent vacuum-insulated enclosures (section), isolated with cryogenic actuated valves (green).

Detailed ^{222}Rn emanation studies were carried out in XENON1T and a thorough understanding of the location and distribution of all ^{222}Rn sources achieved. Fig. 4.6 shows that the dominant contribution to the ^{222}Rn budget comes from the QDrive recirculation pumps (in purple). In XENONnT, we have replaced those either by commercial ultra-high-speed compressors or by magnetically coupled piston pumps developed within our collaboration (see Section 4.3). First ^{222}Rn emanation tests suggested that both solutions would dramatically reduce the ^{222}Rn emanation rate making the remaining fraction less important.
All green sources in Fig. **??** are in contact with gaseous (warm) Xenon. By a smart way of extracting gaseous xenon simultaneously from several ports, we have merged these contributions to an overall xenon flow of not more than 5 SLPM. When the cryogenic distillation column [228] built for XENON1T have removed the $85Kr$ contamination to the required level, this distillation column would no longer be needed for ^{85}Kr removal. It has then been switched to "reverse mode" in order to remove ^{222}Rn out of this special gaseous Xenon stream continuously. We demonstrated with XENON1T that such an "online distillation" reduces the ^{222}Rn emanating out of the cables and the cryogenic pipe. The possible cryogenic distillation column flow is large enough for this special task. Thus, a technical solution for the removal of the green colored fraction in the ^{222}Rn pie chart also exists.
Most problematic are the sources located in the inner vessel and in the TPC as they emanate directly into the liquid xenon. The only chance to

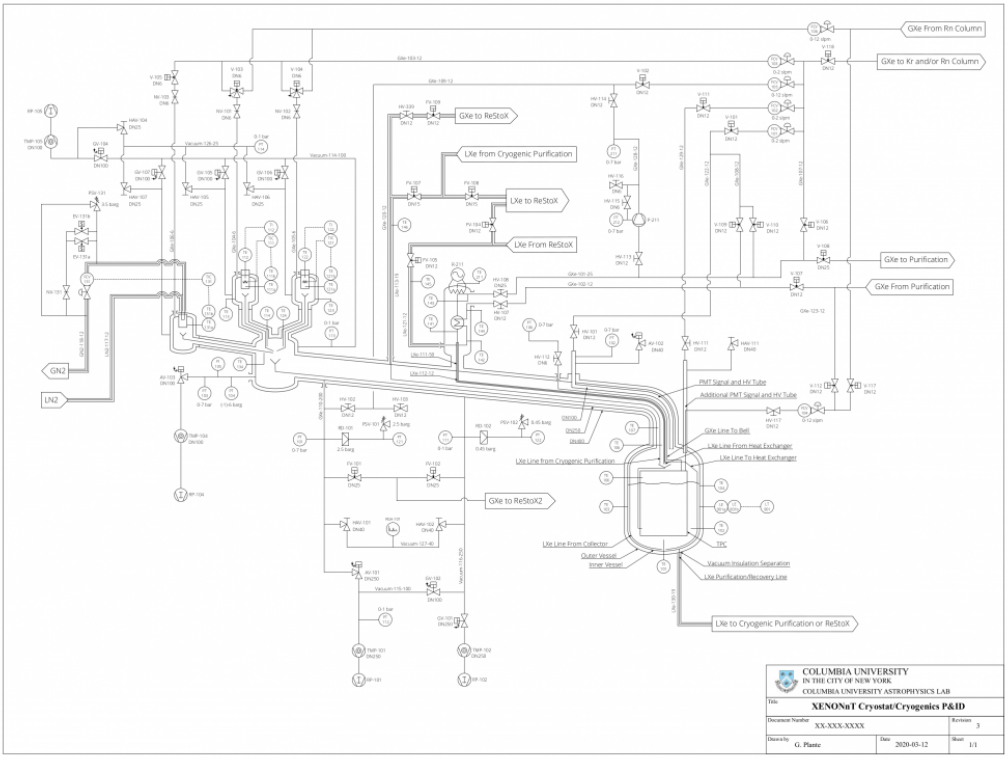

Figure 4.9: The entire cryogenic system in its final version

purify them before they contribute to the background is to extract them on a timescale shorter than the ^{222}Rn mean life ($\tau_{222Rn} = 5.5$ d). This can only be achieved by an enhanced Xenon recirculation speed or a reduced Xenon recirculation time τ_{circ} yielding a reduction factor k [226] of

$$k = 1 + \frac{\tau_{222Rn}}{\tau_{circ}} \tag{4.1}$$

At the same time, the high Xenon gas flow rate demands a dedicated highflow ^{222}Rn removal system based on cryogenic distillation. As shown below, we believed that such a column could be built. It has reduced the sources from TPC and moreover has provided a safety margin for the other sources which have also be reduced by the high-flow column. The combination of all the discussed mitigation strategies guaranteed that the desired ^{222}Rn concentration in XENONnT of $< 1\mu Bq/kg$ has been achieved (see Fig. 4.10)

Subsystem	XENON1T emanation [mBq]	Expected XENONnT 222Rn emanation [mBq]	Speculation about 222Rn in XENONnT [mBq]	Comment	Suggestion Michael/Denny	
	from 222Rn emanation paper	BEFORE distillation	AFTER DISTILLATION [1]		AFTER DST (partial LXe flow)	AFTER DST (full LXe flow)
Cryostat	2.0 ± 0.3	2.0 ± 0.2	~1	Measurement at Costruzioni Generali	~1 [8]	~1 [8]
Cryogenic system	2.4 ± 0.3	2.4 ± 0.3	~2	Measurement at LNGS	~2 [15]	~2 [15]
Cryogenic pipes	9.2 ± 1.0	9.2 ± 1.0	~6	Subtraction of 2 measurements done at LNGS	~6 [15]	~6 [15]
Old cable pipe with cables	2.7 ± 0.2	2.7 ± 0.2	~0	Measurement at LNGS	~0	~0
Old feethrough vessel (porcupine)	1.9 ± 0.2	1.9 ± 0.2	~0	Measurement at LNGS	~0	~0
TPC	4.5 ± 2.2	~7 [2]	~5	Estimation	~3.5 [8]	~3.5 [8]
New cable pipe with cables	—	1.0 ± 0.1	~0	Measurement at LNGS	~0	~0
New feedthrough vessel (hedgehog)	—	~1	~0	Estimation	~0	~0
SAES getters	1.5 ± 0.1	1.5 ± 0.1	~0	Measurement at MPIK	1.5 ± 0.1 [9]	1.5 ± 0.1 [9]
Recirculation pumps	11.0 ± 1.7	0.6 ± 0.1 [3]	~0	Measurement at Muenster University	~0.3 (~0.6) [9,10]	~0.3 (0.6) [9,10]
Rn distillation column	—	~2 [4]	~0	Estimation based on measurement of column packs at MPIK	~0	~0
4 MAG compressors after Rn column	—	1.2 ± 0.1 [5]	1.2 ± 0.1	Measurement at Muenster University	~1.2[11]	~1.2[11]
Liquid xenon purification system	—	~4 [6]	~4	Estimation based on measurement of O2 absorber at MPIK	~3.5[12]	~0[13]
Expected sum	**35.2 ± 3.0 [7]**	**~37**	**~19**		**~19 (~19.3)**	**~15.5 (~15.8)**
Expected concentration [microBq/kg]	**11.0 ± 1.0 [7] (3.2t Xe)**	**~4.3 (8.5t Xe)**	**~2.2 (8.5t Xe)**		**~2.2 (2.3) (8.5t Xe)**	**~1.8 (1.9) (8.5t Xe)[14]**

- 1) It is very hard to predict the reduction due to the Rn distillation column. So this is only a very rough estimate.
- 2) Taking into account that the XENONnT TPC is larger than the XENON1T TPC.
- 3) Assuming 2 MAG pumps with a 222Rn emanation rate as measured here.
- 4) Assuming 8 stainless steel distillation packages, each emanating ~0.25 mBq.
- 5) Assuming that each compressor emanates as much as a MAG pump.
- 6) Assuming 20g of O2 absorber (0.150mBq/g) plus contribution from valves+piping.
- 7) For XENON1T we did an integral measurement of cryostat, cryo pipes, cable pipe, cryogenic system and porcupine and found only 14.5 mBq instead of the expected 18.2 mBq. Therefore, we would have expected only 31.4mBq instead of the given 35.2mBq. Here, we ignore this discrepancy.

Figure 4.10: The different contributions to the overall ^{222}Rn budget in the XENONnT experiment

Design parameters of the dedicated Radon Removal System

We aimed at $\tau_{circ} < \tau_{222Rn}$ to gain a reduction factor $k > 2$ for the ^{222}Rn directly emanating into the LXe target. Therefore we needed a minimal throughput of 200 SLPM or 72 kg/h. We have integrated this system into the LXe purification circuit, receiving the Xenon feed and put out Xenon in the liquid phase. This requires vacuum insulated lines as well as a location near the liquid purification system. Although the radon removal system did not need to achieve a large ^{222}Rn reduction factor it required at least 6 distillation stages (see Fig. 4.11) to make use of our novel method to accumulate the Radon at very high concentrations in the reboiler section of the distillation column where the Radon gets stored and decays. This design required a package column of 1.5 m height and 20 cm diameter. On the other hand, such a Radon removal system could operate with a moderate reflux ratio of $r = 0.5$. This required a cooling power of 1000 W inside the distillation column at the condenser and another 2000 W cooling power to liquefy the Xenon at the output. Both numbers are valid for the envisaged flux of 200 SLPM. An industrial cooling machine provide a cooling power of 2000 W inside the distillation column whereas a heat exchanger inside the reboiler provide most of the cooling for the liquefaction of the Xenon at the output. This provides enough contingency to allow for a reduction of the

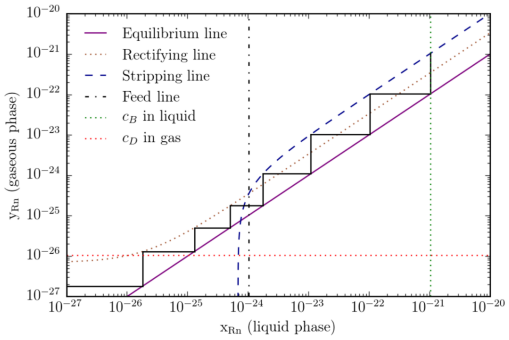

Figure 4.11: Design of the Radon removal system based on cryogenic distillation following the McCabe Thiele method. The input, output and storage concentrations are chosen exemplary to be $10\mu Bq/kg$, $0.1\mu Bq/kg$ and $10\mu Bq/kg$. The throughput is $72kg/h$ and the reflux ratio is set to r = 0.5.

^{222}Rn sources emanating directly into the active LXe target with $k > 2$. A possible improvement is to use a dedicated Clausius Rankine cooling machine to pump the heat from both the condenser and a liquefaction station at the output to the reboiler. Fig. **??** shows a sketch of the system.

4.3 Muon Veto System

The residual muon flux reaching the experimental hall is $(3.31 \pm 0.03) \cdot 10^{-8}$ $\mu/(cm^2 s)$ with an average energy of $\sim 270\ GeV$. Figure 4.13 is the result of a simulation showing the absorption of neutrons and γ from rock radioactivity and of muon-induced neutrons as a function of the water shield thickness. A few meters of water constitute an effective shield against gammas and neutrons produced by rock radioactivity. The only residual background after 4 meters of water is given by muon-induced neutrons, which are produced through direct muon spallation of nuclei or through electromagnetic and hadronic cascades generated by muons. A conservative estimate of the muon-induced neutron flux in the LNGS cavern is $\sim 7.3 \cdot 10^{-10}\ n/(cm^2 s)$ for $E_n > 10MeV$, that is about 3 orders of magnitude lower than that of neutrons from concrete radioactivity, but their energy spectrum extends up to tens of GeV. They may constitute a dangerous background since they can cross the water shield and scatter elastically off the target nuclei leaving a WIMP-like signal. This fact motivated instrumenting the water tank (WT) as an active muon-veto to detect the Cherenkov light that charged particles produce as they cross the water. The aim is to identify events in which a

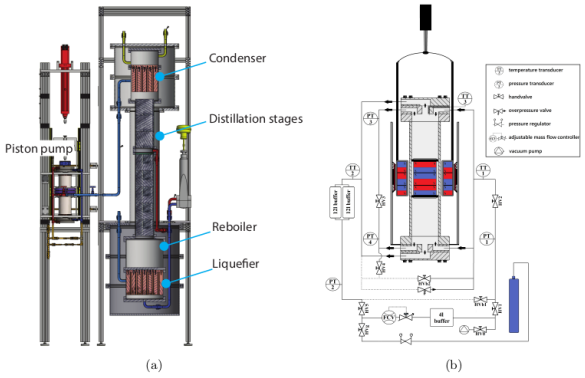

Figure 4.12: (a) Sketch of the Radon removal system based on cryogenic distillation with an enhanced throughput of 200 SLPM. The total height of the column is around 3 m. To have enough reserve both heat exchangers (condenser and liquefier) will be enlarged in transversal directions. (b) Schematics for the custom made magnetically coupled piston pump

muon directly crosses the WT, and also events in which a muon is outside but the particles constituting the electromagnetic or hadronic cascade enter the WT.

4.3.1 Muon Veto design

The "ingredients" of the XENON1T water Cherenkov Muon Veto are the WT, $\sim$ 10 m heigh and $\sim$ 10 m in diameter, a certain number of PMTs, with a certain geometrical arrangement and working with an appropriate trigger condition, and a reflective foil [241].
The selected PMT is the high quantum efficiency (HQE) 8" Hamamatsu R5912ASSY, already provided with a water-proof enclosure. These PMTs have a bialkali photocathode and borosilicate glass window. Ten dynodes provide a typical gain of 10^7 at a working voltage of $\sim$ 1500 V. The quantum efficiency is about 30%, averaged over the Cherenkov light wavelength distribution, in the range [300-600] nm (see figure 4.14), and the collection efficiency is 85%, as declared by the manufacturer [242].
The reflective foil chosen is DF2000MA by 3M, which provides a very good reflectivity (more than 99% between $\sim$ 400 and $\sim$ 1000 nm, as declared by the manufacturer [243] and consistent with what obtained with dedicated

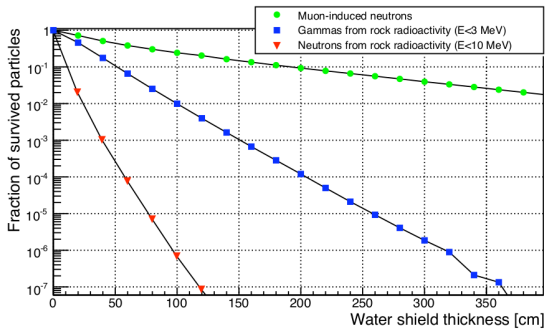

Figure 4.13: Fraction of survived particles as a function of the thickness of the water shield surrounding the detector. Circular dots for the muon-induced neutrons, squared dots for the gammas from rock radioactivity and triangular dots for neutrons from rock radioactivity.

experimental measurements, as shown in Fig. 4.15), and allows for a shift in the wavelength of the UV Cherenkov photons toward the blue region in order to better match with the PMTs wavelength sensitivity. A similar study was carried out in the GERDA experiment, using the same reflective foil by 3M [244].

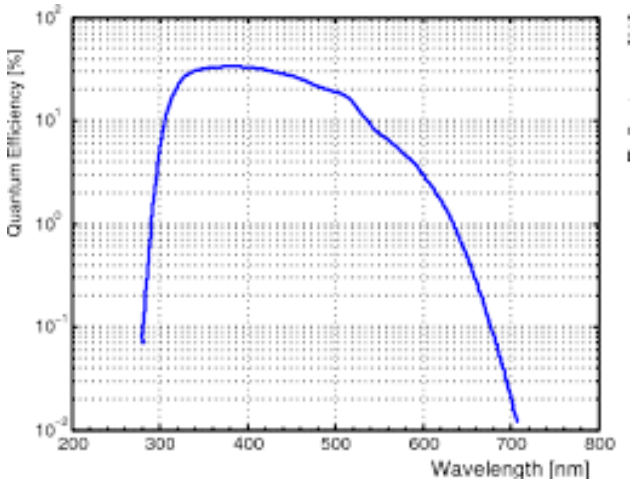

Figure 4.14: Quantum efficiency of one of the HQE Hamamatsu PMTs R5912ASSY

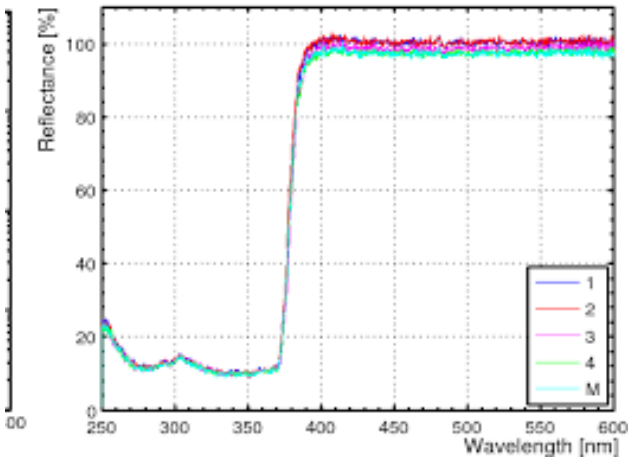

Figure 4.15: Specular reflectivity measurements of DF2000MA in different positions on the surface of a square shaped foil sample

4.4 Other subsystems

The fast and ambitious realization of XENONnT relies on the fact that a large number of subsystems can be re-used [213]. This does not only reduce the time and efforts required for their design and construction, but also greatly speeds up the commissioning phase of the new detector. In this section we quickly summarize which systems will be kept (almost) unchanged from XENON1T, for details see [230].

4.4.1 Water shield, Building

The water tank was installed in Hall B of LNGS acts both as an active Muon Veto (see Section 4.3) and as a passive shield. This system are re-used for the XENONnT phase. The same holds for the XENON building installed next to it.

4.4.2 Cryogenic System. ResStox-1 and ReStox-2

As mentioned above, the outer cryostat as well as the large-diameter cryogenic pipe connecting the cryostat to the XENON building are also used for XENONnT. Especially the pipe with its complicated inner structure and the delicate connection to the cryogenic system remained in place during the transition period and for XENONnT. The cryogenics system cools down the Xenon gas by means of two redundant coldheads using pulse-tube-refridgerators (PTRs) and an additional LN_2-based coldhead. The system provides sufficient cooling

power also for XENONnT.
A Xenon-storage system, ReStoX-1, based on a new concept, was developed for XENON1T in order to increase the recovery speed of LXe compared to previous systems based on bottles.
ReStoX-1 is a 2.1 m diameter sphere made of stainless-steel. With a volume of 5 m^3 , it can store up to 8 t of LXe. The minimized thermal contact between the outer and the inner cryostat spheres reduces the external heat-load to 50 W. The sphere is cooled with 16 LN_2 lines welded to the inner sphere. In normal operation, while storing Xenon in liquid state, a condenser/heater system, mounted at the center of the vessel, controls the pressure precisely and ensures that the pipe where LXe flows does not get blocked by frozen Xenon. ReStoX-1 is connected to the detector for filling and fast recovery and to the purification system via an independent heat exchanger.
This system has worked very well during the entire phase of XENON1T and it will be in operation as part of the new liquid circulation loop for XENONnT. Given the larger size of the XENONnT detector, a bigger storage system is necessary. The new system, which is complementary to ReStoX-1, is called ReStoX-2 and has a capacity of 10 t.
Just like its predecessor, ReStoX-2 has been designed to withstand pressures from vacuum up to 70 bar. This allows for keeping the whole Xenon inventory safe even at ambient temperature, thanks to 33 mm thick stainless steel walls and dedicated cryogenic gate valves. ReStoX-2 is a cylindrical vessel with 1.45 m diameter and 5.5 m height. It has an LN_2-based inner cooling system made of a parallel-plate heat exchanger. While the ReStoX-1 cooling principle was to cool down Xenon efficiently but without freezing it, the ReStoX-2 approach is more aggressive: Xenon is recovered by crystallization, with a target recuperation flow of one ton per hour.
The installation of ReStoX-2 started at the beginning of spring 2018, when it was connected to ReStoX-1, the detector cryostat and the rest of the cryogenic systems through a piping system (see Fig. 4.16). The filling of the cryostat from ReStoX-2 was done by passing through ReStoX-1, which has a sophisticated system that regulates the pressure at high precision.
The recovery from the cryostat to ReStoX-2 works directly and can be done both in a controlled mode, with a dedicated gate valve, and in emergency mode, with a rupture disk regulated at the cryostat pressure of 2.5 bar to prevent Xenon losses from any possible accident of the cryostat. Such fast recovery is triggered also in case of vacuum losses of the cryostat insulation, ensuring prompt reaction and extra safety.

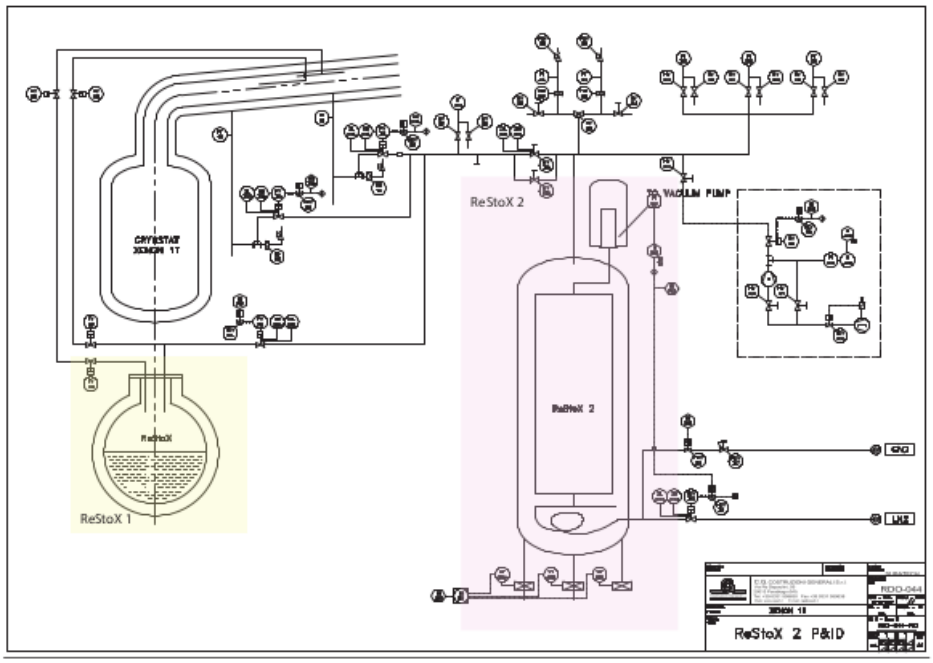

Figure 4.16: Diagram of the new ReStox-2 storage system and how it integrated into the existing XENON1T cryogenics

4.4.3 Cryogenic distillation Column

Radioactive ^{85}Kr is removed from the Xenon gas via cryogenic distillation. The 5 m-tall distillation column designed and constructed for XENON1T has already demonstrated a separation factor above $6 \cdot 10^5$ and a $^{nat}Kr/Xe$ concentration of < 0.026 ppt [228]. This is sufficient for XENONnT.

4.4.4 Calibration System

We mostly re-use the existing infrastructure for the calibration of XENONnT. A deuterium-deuterium (DD) neutron generator and an AmBe source are used for the nuclear recoil calibration. $m^{83}Kr$ are used for detector uniformity and energy calibration. A ^{220}Rn source, developed for XENON1T [226], are used for electronic recoil band calibration. PMT gains are calibrated with the LEDs in a similar way as done in XENON1T [230]. Other external γ-sources are used to validate high energy response and position reconstruction performance near the edge of detector.

4.4.5 Slow control system

The XENON1T slow control system was based on General Electric (GE) industry standard components. It monitored a large number of operation parameters, controls the cryogenics and purification systems, and was used to send automated alarm notifications in case parameters fall out of their pre-defined range. The slow control system of XENON1T has been updated in order to integrate the new detector XENONnT performances.

4.4.6 Data acquisition (DAQ)

The DAQ system was designed in a modular and parallel fashion [230]. This allows inclusion of the additional TPC channels easily without affecting the readout speed. The trigger decision for the TPC is taken in software; to ensure its performance given the increased number of channels, we have upgraded the event-builder machines running the code. The Muon Veto is already read using the same programs and the new Neutron Veto system can be implemented.
XENONnT directly benefit from the well-established raw data processing, data analysis and signal simulations platforms already developed for XENON1T

4.4.7 Computing

For XENON1T, the collaboration has opted for a flexible, distributed computing model, using different sites including GRID resources; for XENONnT more sites have easily been added once they become available. The expected increased data rate (mainly caused by the increased number of TPC and nVeto channels) is partly compensated by using dedicated data reduction strategies, e.g., by deleting the raw data of non-interesting events outside the region of interest in calibration runs. We have planned to cope with a total of 1.5 PB/y for a duration of 5 years. Connection to the LHCOne network has been required to cope with the XENONnT data volume.

4.5 Neutron Veto System

Once the background from Rn is reduced by a factor 10 with respect to XENON1T using the techniques described in section 4.2, the NR background from radiogenic neutrons (from α, n reactions and spontaneous fission) starts to become relevant for the final sensitivity of the experiment and, in particular, for its potential to discover WIMPs [213]. The expected neutron background in the new TPC, predicted through a full Monte Carlo simulation as described

in [225], is ~ 5.5 events in a 4 t fiducial volume for the nominal 20 $t{\cdot}y$ exposure required to reach the XENONnT sensitivity goal.
With the goal of reducing the radiogenic neutron background and maximize the liquid Xenon fiducial volume in XENONnT, it is under constrution, almost completed, a Neutron Veto (nVeto) surrounding the outer cryostat as closely as possible. Since the most dangerous neutrons are the so called "sneaky" neutrons, those which scatter just once into the LXe and then leave the cryostat, the nVeto has to watch for neutrons just around the cryostat. A solution with Gadolinium directly dissolved into the water of the Muon Veto (but optically separated from it), where also the cryostat is immersed, has been adopted (see Figure 4.17). Thanks to the isotopes ^{157}Gd and ^{155}Gd, Gadolinium has the highest n-capture cross section of all stable elements. Neutrons are thermalized in the wather and eventually captured on gadolinium, releasing a γ-ray cascade with a total of $\approx$ 8 MeV. More details about this detection process are illustrated in next Subsection.
The γ-s from the neutron capture will be detected by 120 photomultipliers (PMT) supported by a stainless steel cylindrical structure, where they are organized in 15 columns and 8 rows around the cryostat, at about 1 m distance from it. Reflector foils wrapped around the cryostat and put behind the PMT support structure, with a reflectivity of about 99%, will enclose the nVeto region, which results in a cylindrical corona of inner radius 1 m, outer radius 2 m and hight of 5 m [247].

4.5.1 Neutron detection with Gd

Isotope	Abundance (%)	σ (b)
^{152}Gd	0.2	735
^{154}Gd	2.18	85
^{155}Gd	14.8	$60.9 \cdot 10^3$
^{156}Gd	20.47	1.8
^{157}Gd	15.65	$25.4 \cdot 10^4$
^{158}Gd	24.84	2.2
^{160}Gd	21.86	1.4

Table 4.4 : Thermal neutron capture cross sections of the various Gd isotopes that can be found in nature. Their abundance in ^{nat}Gd is also reported. The two isotopes which are exploited for their high (n, γ) cross section are the ^{155}Gd and ^{157}Gd

Gadolinium ($^{A}_{64}Gd$) is a rare element on Earth [254]. Its natural composition consists of 7 isotopes. Their abundance ratio and the corresponding neutron

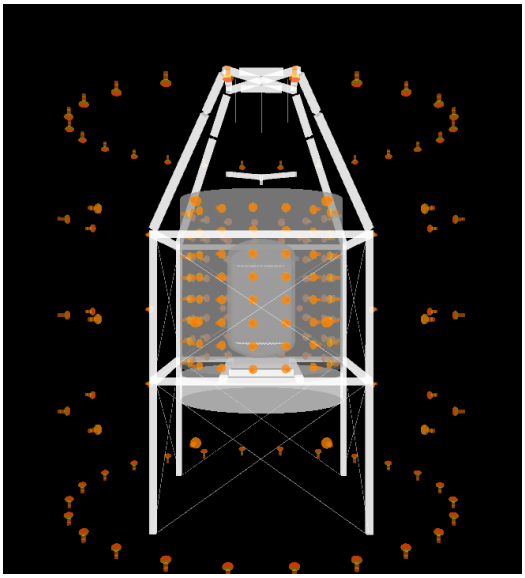

Figure 4.17: Schematic view of nVeto. Gd-water is loaded in the whole volume of the Muon Veto tank. Optical separators installed in the backside of the nVeto-PMTs are shown in light gray.

capture cross sections are shown in Tab. 4.4. The Gd, in particular the ^{155}Gd and the ^{157}Gd isotopes, has a resonance state in the thermal energy region in the neutron capture reaction (Fig. 4.18). The capture process is resolved in the excitation of the Gd, which returns to the ground state emitting approximately 3-4 γ [255]. The process for the ^{155}Gd reads:

$$n +^{155} Gd \rightarrow^{156} Gd^{*} \rightarrow^{156} Gd + \gamma's \tag{4.2}$$

Thus the γ-ray energy can be calculated via mass difference (in natural units, c=1):

$$E_{\gamma} = M(^{155}Gd) + M_n - M(^{156}Gd) = 8.54MeV \tag{4.3}$$

where M_n is the neutron mass, while M(^{155}Gd) and M (^{156}Gd) are the mass of ^{155}Gd and 156 ^{156}Gd, respectively. Similarly, for the process involving the ^{157}Gd isotope, the γ energy is 7.94 MeV.
The techinique of adding Gd to the water to tag neutrons, was first proposed by Beacom and Vagins [256] for use in the Super-Kamiokande (SK) water Cherenkov detector which was very successful in observing solar, atmospheric, and accelerator neutrinos. Their proposal aimed at increasing the detector sensitivity to inverse beta events by delayed coincident detection of fast Cherenkov signal and neutron capture on Gd [247]. The required water

purification technology was developed and proven at the EGADS experiment (Japan), which maintained excellent Gd-water quality over more than two years of stable operation without loosing Gd.
In the XENONnT nVeto, Gadolinium is added in water by dissolving Gd ultrapure salts like GdCl 3, $Gd(NO_3)_3$ and $Gd_2(SO_4)_3$. Since the chlorine in $GdCl_3$ causes unwanted corrosion and the nitrate in the $Gd(NO_3)_3$ tends to absorb part of the Cherenkov light spectrum, the Gd-sulphate $Gd_{12}(SO_4)_3$ results to be the best candidate when it is octahydrate ($Gd_2(SO_4)_3 \cdot 8H_2O$), to enhance its solubility. It is used a concentration of $Gd_2(SO_4)_3$ of 0.48% which corresponds to about 0.2% concentration in mass of Gd. Figure 4.19 shows the fraction of neutron capture on Gd as a function of the concentration of gadolinium sulphate [257]. With a 0.2% concentration, the $\approx$ 90% of the neutrons are captured by the Gd, while the remaining part relies on the capture in water.
The XENONnT nVeto will employ that concentration of Gd sulphate in order to reduce the NR background rate coming from the detector materials as shown in Fig. 4.20. In addition to a sufficiently high concentration of gadolinium, which is necessary for the detection and capture of neutrons, is required to reach a neutron tagging efficiency $\geq 85\%$, which can be obtained by requiring a 10-fold PMT coincidence (Fig. 4.21).
The amount of background induced by the materials that make up the nVeto was obtained from MC simulations and these studies are illustrated in more details in next Subsections.

4.5.2 Overview of Gd-loaded water nVeto systems

Parameter	
Density	1,01 g/cm^2
pH	2.9
Radiopurity mBq/kg $(Gd_2(SO_4)_3)$ See also Fig. 4.22 and Fig. 4.23	^{238}U a few ^{232}Th a few $^{235}U < 1$

Table 4.5 : Characteristics of 0.6% weight $Gd_(S0_4)_3 + 8H_2O$ solution planned for Super-Kamiokande Gd project

The Gd-loaded water for the Super-Kamiokande Gd project has been studied by the Super-Kamiokande collaboration for many years on the physics of the n-tagging, operation including water purifications, impacts on detectors and environment, etc. By borrowing the results of this work, it was possible to propose for XENONnT a realistic approach to use 0.2% wt gadolinium,

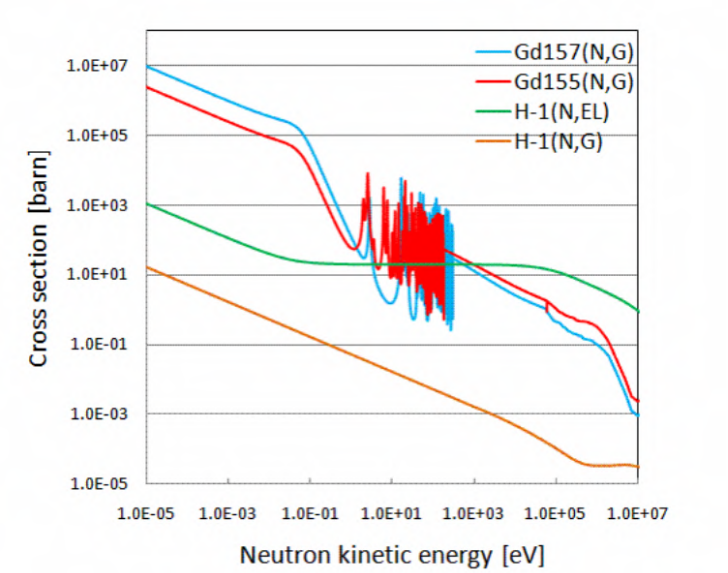

Figure 4.18: Trend of various cross section of the process involving neutrons and $^1H/\ ^{155}Gd/^{157}$ with respect to the neutron kinetic energy. The neutron-H interaction can occur as elastic scattering (green line) or as (n, γ) (yellow line). On the other hand the dominant process with the Gd isotopes is the (n, γ) (blue and red lines). The cross section for the Gd decreases with the energy but for values O(eV) presents some resonant states.

or 0.6% wt gadolinium sulfate octahydrate ($Gd_2(SO_4)_3 \cdot 8H_2O$) as an actual chemical compound. Typical gamma-ray emissions from the n-capture on Gd gives about 8 MeV in total with a multiplicity of ~ 6 (see [250]). Characteristics of 0.6% weight $Gd_2(SO_4)_3 \cdot 8H_2O$ solution planned for SK-Gd are summarized in Tab. 4.5.
It was used the official XENONnT simulation package (nVetoDevelopment) for the experimental geometry, where the Okayama-model implemented for the Gd-related physics. The Cherenkov photons were simulated with G4 Optical Physics built in GEANT4.10.3.
The final configuration of the nVeto, called "whole tank Gd-Water configuration", includes the following components: gadolinium loaded water, nVeto PMTs (typically 1208" PMTs), Gd-water circulation system including appropriate purification filters and tanks for Gd capture. The masses of water, $Gd_2(SO_4)_3 \cdot 8H_2O$ and gadolinium are 700 tons, 4.2 tons and 1.4 tons, respectively. It's important to underline that the amount of Gd would impact also on the total cost for the water system and for process/disposal of Gd-loaded water at the discharge.

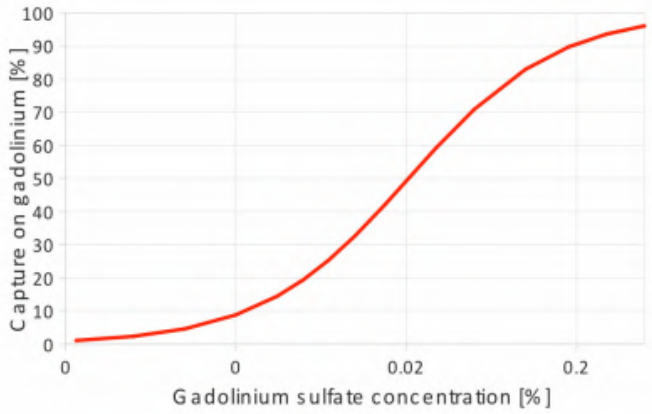

Figure 4.19: Fraction of neutron capture on Gd as a function of the $Gd_2(SO_4)_3$ concentration. With a 0.2% concentration, which correspond to a $\approx 0.1\%$ in mass of Gd, the $\approx 90\%$ of neutrons are captured by the Gd, while of the remaining 10%, the 6.5% are captured by protons of hydrogen in water, while the 3.5% are not detected. To reach the required neutron tagging efficiency in the nVeto, this concentration of Gd has to be loaded in water.

Regarding the problem of radioactive background produced by the Gadolinium salt, Super-Kamiokande group has developed low-radioactive $Gd_2(SO_4)_3$ powders. Fig. 4.22 shows the state-of-the-art materials available. On the other hand, one of the candidates for the nVeto PMTs is Doble-Chooz PMT (R7081); there are two results on the background measurement of R7081. The results are shown in Fig. 4.23. Discrepancies, especially the ^{238}U activity, are seen and further investigations are on-going.

4.5.3 Whole tank Gd-Water configuration

In this final configuration, nVeto replaces the pure water for the Muon Veto with Gd-loaded water. The main advantage is simplicity and high efficiency, thanks to an almost 4-pi coverage of TPC with no water-displacer.
As mentioned before, the total mass of the water loaded with gadolinium is 700 ton with 4.2 ton of $Gd_2(SO4)_3 \cdot 8H_2O$ and 1.4 ton of Gd. The largest risk is corrosion of materials directly exposed to the Gd-loaded water, which might be managed by "covering" target materials. Another potential but critical risk is 1.4 ton of Gd which should be appropriately managed for water circulation and discharge. Relatively low yields of Cherenkov photon can be manageable thanks to an enough photo-coverage ($\sim$ 8%) and high

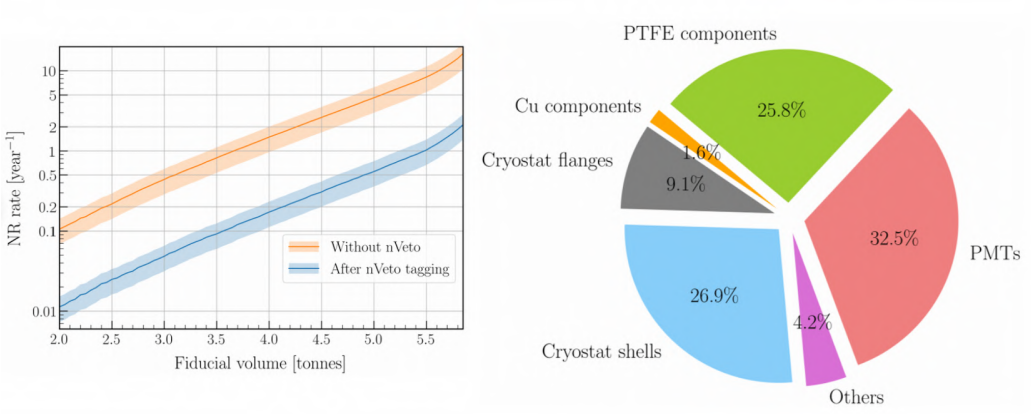

Figure 4.20: (Left) Nuclear recoil background reduction that will be achieved in XENONnT with the Neutron Veto in operation (blue line). Considering a 4 t fiducial volume, the reduction factor is about 6. (Right) Diagram of the contributions to the NR background due to the detector materials. These are dangerous source since the emitted neutrons can give a WIMP-like signal inside the TPC [258]

reflectivity of reflectors ($> 90\%$).
Another interesting feature of this configuration is that it is possible to start with pure water without gadolinium which still show a moderate neutron tagging efficiency. It is possible to move into Gd-loaded water phase after the confirmation that the system is working as designed.
It should be noted that this configuration brings minimal interference with the outer calibration source delivery system, as the sources are moved from top to position them next to the TPC. A slit in the Tyvek roof of the optical separator between nVeto and Muon Veto will allow these sources to pass in and out of the nVeto region without significant loss of light. In particular, this configuration does not need a gap for neutron calibration system in the azimuthal nVeto coverage around the TPC. This configuration also keeps the potential to perform calibrations at various positions in the water volume.

Installation, maintenance, and calibration

As mentioned before, Neutron Veto System is equipped with 120 PMTs . They are water-proof and equipped with support structures. A highly reflective optical separator between nVeto and Muon Veto (Tyvek or Gore-Texa's) is used to shield the nVeto from light induced by external gammas and neutrons entering the Muon Veto from the outside. This allow for a

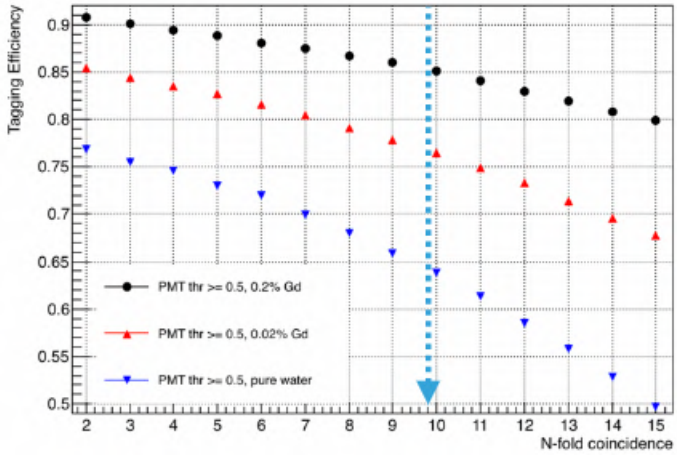

Figure 4.21: Neutron tagging efficiency as a function of the PMT coincidence for several nVeto configurations: (blue triangles) pure water nVeto, (red triangles) 0.02%Gd loaded nVeto and (black dots) 0.2% Gd loaded nVeto. With a 10-fold coincidence in the third configuration, the efficiency stands at $\approx 85\%$ which is the requirement for the XENONnT purposes. In all the cases simulated the PMT threshold for the signal is at 0.5 photoelectrons. Thus it is important to study the characteristics of the PMTs such as the dark rate with this threshold.

further efficiency boost as it allows to relax the coincidence requirement for nVeto triggering. Being made of Tyvek sheets stitched together with stainless steel staples as in SK this optical barrier is easy to remove and to re-install. Support structure for optical $reflector/separator$ behind the nVeto PMTs (is the PMT holding structure itself). nVeto PMTs background level requirements are discussed later.
An optical reflector for the outside of the cryostat has been first installed. Then the PMT holding structures has been built. These structures were wrapped with reflectors in advance. Additional reflectors have been installed after the structures was built. PMTs and optical separator have been also installed. The tank will be filled with water. We can dissolve gadolinium when things are ready and increase the tagging efficiency. Water quality needs to be monitored continuously and the water should be filtered properly. At the scheduled drain or emergency discharge, the tank is drained and the Gd-water needs to go through the Gd-capture resin and the gadolinium should be removed from the water.
As for calibration, it comes naturally with the neutron generator or ^{241}Am Be as a source as it is deployed inside this nVeto volume.

Very Preliminary — unit [mBq/kg $(Gd_2SO_4)_3$]

Chain	238U			232Th			235U	
Isotope	238U		226Ra	232Th	228Ra	228Th	235U	227Ac /227Th
Goal*	< 5		< 0.5	< 0.05	< 0.05	< 0.05	< 3	< 3
Detector	Ge	ICPMS	Ge	ICPMS	Ge	Ge	Ge	Ge
Company A*	< 8.8	3.0±0.1	< 8.8	2.4±0.2	< 5.9	< 5.9	< 35	< 35
Company B	< 25	2.7±0.2	< 0.6	1.2±0.1	< 0.7	0.9±0.3	< 3.1	< 6.1
Company C	< 13	2.1±0.4	< 0.3	1.0±0.1	< 0.3	< 0.4	< 0.6	< 1.9

Figure 4.22: Radioactivities in $Gd_2(SO_4)_3$ (from [248])

	^{232}Th	^{238}U	^{40}K	
Japanese group	114	909	676	[mBq/kg]
Manfred	250	160	910	[mBq/kg]

	^{232}Th	^{238}U	^{40}K	
From Japanese group	17	131	96	[Bq/120PMT]
From Manfred	42	27	129	[Bq/120PMT]
(XENON1T R5912	132	211	620	[Bq/120PMT])

Figure 4.23: Radioactivities in the PMT glass. The data refer to PMT samples from two different companies. A decision will be made considering the respective advantages and disadvantages

The transparency of Gd loaded water is a key point for efficient operation of Neutron Veto (and Muon Veto), consequently the water recirculation/filtration system plays a key role [247]. A specific system has been implemented in the EGADS experiment (200 tons of water, $\approx$ 240 PMTs and 0.2% $Gd_2(SO_4)_3$ to keep Gd-water clean, it is based on a molecular band pass filtering system, where the water first passes through an Ultrafilter which retains and drain impurities larger than $Gd_2(SO_4)_3$, then through a Nanofilter which separates the $Gd_2(SO_4)_3$ and allow it to bypass the deionization (DI) resin, while singly charged ions are allowed to pass. These ions are then absorbed in a DI resin bed and finally the clean water is reunited with the bypass stream and the Gd2(SO4)3 again. This delicate and technologically sophisticated system will also be implemented in XENONnT for nVeto operation. Given the complexity, it puts high demand on the Slow Control to monitor pumps, temperature sensors, flow meters and other devices. Radiopurity of the Gd salt needs to be measured in order not to add background that hampers the detector performance.

4.5.4 MC study - Method 1: request of n-fold coincidences with a window of 300 ns

A MC study shows a reasonable tagging efficiency of 85% for neutrons from the outer cryostat (the so called "sneaky neutrons" or "dangerous neutrons") with 7-fold coincidence as shown in Fig.4.24 (See details in [251]).
The average number of generated Cherenkov photons per event is $\sim$ 720 photons, and $\sim$ 40 photoelectrons are generated in the nVeto PMT arrays, corresponding to a light collection efficiency of $\sim$ 5.6 %. For each events, typically $\sim$ 30 PMTs can see at least one photoelectron as shown in Fig.4.25.
Inefficiencies of this design basically originats from following reasons;
• Neutrons are captured in LXe below the bottom PMT array PTFE, shaper rings, or inner/outer cryostat (See Fig.4.26)
• Then, all the emitted gamma-rays lose energy somewhere in the inactive volume (See Fig.4.27).
• Preliminary study shows that it might be possible to recover $3-4$ % efficiency by introducing E_{tot} below PMTs cut, which requires additional PMTs there.
Pure-water results are compared with Gd-loaded results in Fig. 4.28 and 4.29. A moderate tagging efficiency of 74 % is expected with pure water case. Time difference between the TPC events and nVeto PMT hits are investigated. The mean times are 19 μs and 33 μs for the Gd-water and pure water case, respectively (Fig. 4.30). Background rate from the inner-PMT glass was evaluated and results are shown in Fig. 4.31; at least 7-fold coincidence is needed to suppress the background rate below 100 Hz.Here 42 Bq/120 PMT from ^{232}Th, 131 Bq/120 PMT from ^{238}U, 129 Bq/120 PMT from ^{40}K are assumed. Finally, background rate from $Gd_2(SO_4)_3$ was evaluated; it was expected to be between 2.9 Hz and 1.4 Hz for 2.1 mBq/kg of ^{238}U and 1.0 m Bq/kg of ^{232}Th, respectively.

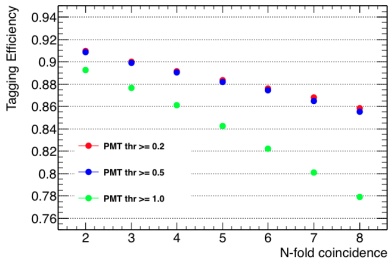

Figure 4.24: Tagging efficiency as a function of N-fold coincidence

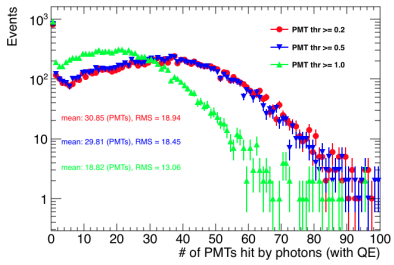

Figure 4.25: Histogram of the number of PMTs with hits

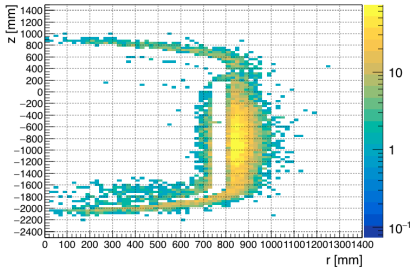

Figure 4.26: Neutron capture position in r-z plane for "dangerous neutron" events

4.5.5 MC study - Method 2: comparison of the spatial and time distribution of the nVETO Cherenkov photons between background and "sneaky neutrons"

In the MC studies discussed in previous Subection, the detection efficiency of the nVeto, or the ability to identify "sneaky neutrons", was given by an x-fold coincidence between the nVeto PMTs. Using this method, even a request of 10-fold coincidence with a window of 300 ns results at present unsatisfactory because of an high amount of "false positives", or coincidences of 10 PMTs that do not correspond to any signal (neither "sneaky neutrons" nor background), in relation with neutron tagging efficiency. However, spatial and temporal information are thought to help lower the level of coincidence. This innovative MC study [253] has two objectives: show that the spatial time distribution is different for background events from nVeto PMTs and "sneaky neutron" capture events and find a method to reduce the background detection efficiency while leaving the tagging efficiency of neutrons .
One possible idea is to build "probability maps" for background events and "sneaky neutrons" events. It was set a threshold of 0.5 p.e. for all simulated hits and the arrival time of Cherenkov photons was calculated starting from

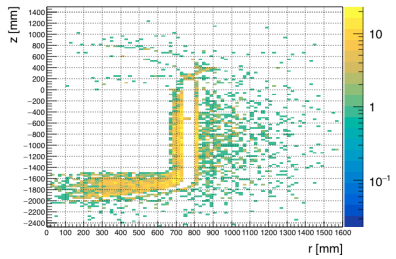

Figure 4.27: Gamma-ray interaction position in r-z plane for non-tagged events

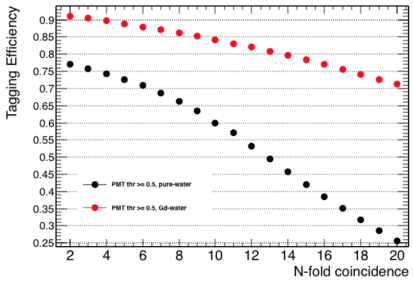

Figure 4.28: Comparison of the neutron tagging efficiency between pure water and Gd+water as a function of N-fold coincidence. (Black: pure-water design. Red: Gd-water design. 0.5 p.e. threshold is considered for both cases.)

the arrival time of the first Cherenkov photon detected. Probability maps are used to build log-likelihood ratio maps. Each simulated event is compared with the log-likelihood ratios map and a ratio value R is obtained as:

$$R = \sum_{s,t} log_{10} | \frac{\mathcal{L}_n^{s,t}}{\mathcal{L}_b^{s,t}} | \tag{4.4}$$

where $\mathcal{L}_n^{s,t}$ and $\mathcal{L}_b^{s,t}$ are the likelihood functions for the event being analyzed in relation to the probability distributions in the case of a sneaky neutron and background event respectively, for each PMT position s and for each arrival time t of the Cherenkov photon. Since the 120 PMTs are placed in 15 columns and 8 rows, it was set set $s = 0$ for the columns in which the arrival of the first photon occurs, $s < 0$ for the 7 columns placed on the left of this, $s > 0$ for the 7 columns placed on the right. It was considered arrival times t from 0 to 30 ns with a binning of 2 ns, corresponding to the time resolution of the PMTs.
It is clear that if $R < 0$ the event in question is "more background alike", if

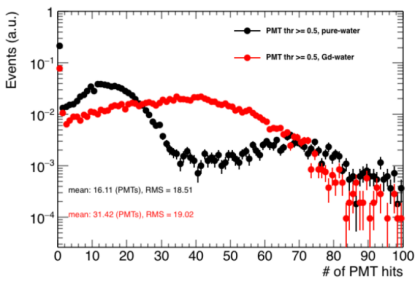

Figure 4.29: Number of PMT that exceed the 0.5 p.e. threshold for a neutron capture event. (Black: Whole-tank pure-water design. Red: Whole-tank Gd-water design. 0.5p.e. threshold is considered for both cases.)

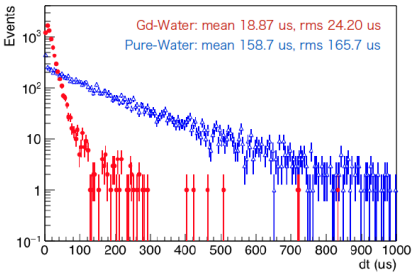

Figure 4.30: Timing distribution of the neutron veto events. Time difference from the TPC events are shown. Red and blue histograms show Gd-water and pure water options, respectively.

$R > 0$ the event in question is "more sneaky neutron alike", while if $R \approx 0$ is difficult to identify the event as a sneaky neutron event or as a background one. In this way, by simulating a large number of events, it is possible to determine the efficiency of this method for identifying "sneaky neutrons". An exemple of "probability maps" for an event, summed over all the 8 rows of PMTs, is illustrated in Fig. 4.32, Fig. 4.33 and Fig. 4.34. In Fig. 4.32 is illustrated the "probability map" of the event in relation to sneaky neutrons, or the map of $\mathcal{L}_n^{s,t}$; in Fig. 4.33 is illustrated the "probability map" of the event in relation to background, or the map of $\mathcal{L}_b^{s,t}$; finally in Fig. 4.34 is illustrated the "ratio map" of the event, or the map of R. As you can see, in this case, by adding the values of R on all the PMTs and on all the possible arrival times, a total value of $R < 0$ is obtained, in conclusion this event must be considered "more background alike", precisely "more gamma alike", where a "gamma" are a particular type of bakground events which will be discussed in the next Subsection.

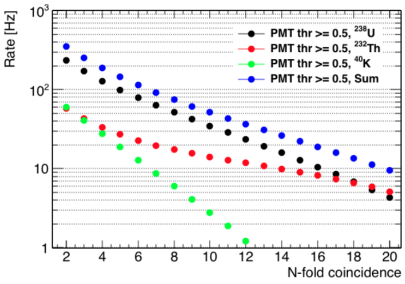

Figure 4.31: Background rate from the inner-PMT glass. (Whole-tank Gd-water design)

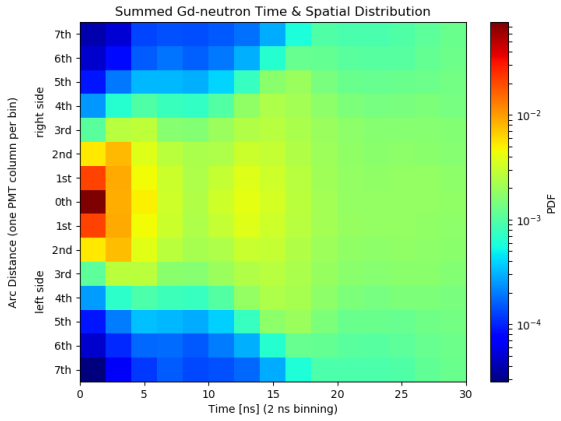

Figure 4.32: Example for probability maps summed over all PMT rows - Summed hit pattern neutrons

Production of MC simulated neutron events

Event Selecting: 250k sneaky neutrons, originating from the cryostat and internal and external TPC, were simulated. All events were selected requiring their capture in the water on the lateral side of the tank, or beteween -1700 mm $<$ z $<$ 500 mm (see Fig, 4.35).
Background events, or events originated by the PMTs of the Neutron Veto (the amount of this events is illustrated in Fig. 4.23), were also simulated. There are two types of background events from PMTs: the so called "gammas", i.e. monoenergetic photons of 2.6 MeV originated from the last decay of ^{232}Th chain, that can produce more electrons above the Cherenkov threshold, and the so called "betas", i.e. electrons originated by ^{40}K decay with a pseudo-beta energy spectrum (see Fig. 4.36)

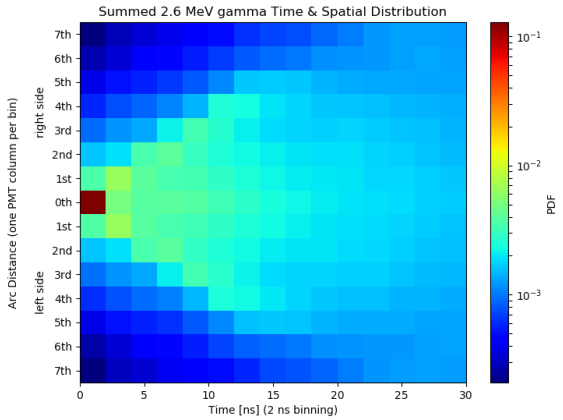

Figure 4.33: Example for probability maps summed over all PMT rows - Summed hit pattern gammas background

Ratio map gammas and beats: The map of the ratio R was defined for each row of PMT, with a 2 ns binning. Since the measured p.e. value could not be implemented, a PMT is considered "on" if at least one photon arrives, so each hit was counted. The maps show a clear pattern. In Fig. 4.37 and Fig. 4.38 are illustrated ratio maps for an event, considering gamma and beta as background, respectively, separately for all the 8 rows of PMTs.

Discriminate with R value: Before calculating R for each individual hit two more requirements are checked:
1) classical X-fold coincidence level
2) tight level threshold (m photons within 30 ns).
Values which do not satisfy the condition 1) were never detected, hence $R = -10$ is assigned. Instead, if the condition 2) is not fulfilled $R = 10$ is assigned.
In Fig. 4.39 the distribution of R for sneaky neutrons events is shown in comparison with the distribution of R for gammas background events, with the condition 1) = 4 and 2) = 3. These distributions show that R can then be used to discriminate between sneaky neutron and background signals, in this case gammas. Above a certain threshold R value, which depends on the conditions 1) and 2) set, the signal can be identified as a sneaky neutron event, while below this value it can be considered as a background event.
It was also defined a "detection efficiency" τ for backgrounds and neutrons.

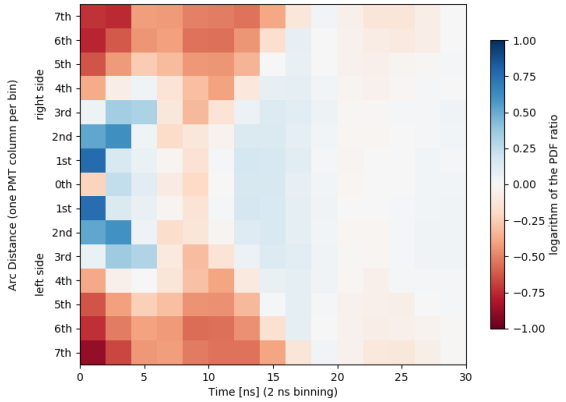

Figure 4.34: Example for probability maps summed over all PMT rows - Ratio map

This "detection efficiency" is not directly comparable to "tagging" efficiency defined previously for the method 1. It was defined as "surviving number of events divided by all events which had at least 1 nVETO PMT hit", where "surviving number of events" is the number of events that satisfy the conditions 1) and 2).

Results of the study and conclusions

By adopting the method just described, a lot of information in the space-time distribution of the Cherenkov photons was obtained. Time and space distribution of the Cherenkov photons can help to improve the discrimination power. The information is encoded in the very first 10 to 20 ns; thanks to this method, it was obtained a detection efficiency for sneaky neutrons up to 90% with 7-fold coincidence, a reduction of background from "betas" (at least for ^{40}K) up to 95% while for "gammas" it is more difficult to give a satisfying judgment.

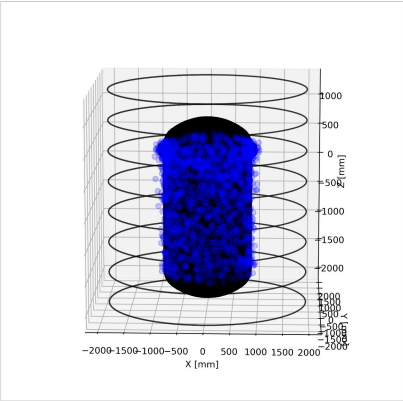

Figure 4.35: Lateral neutron capture events

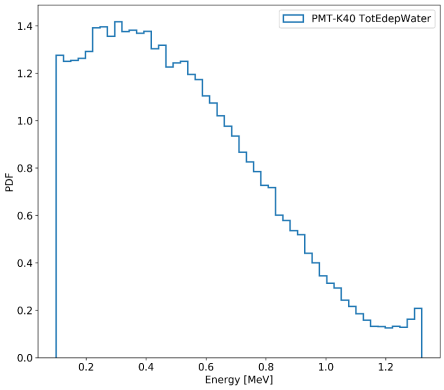

Figure 4.36: Pseudo ^{40}K Beta spectrum

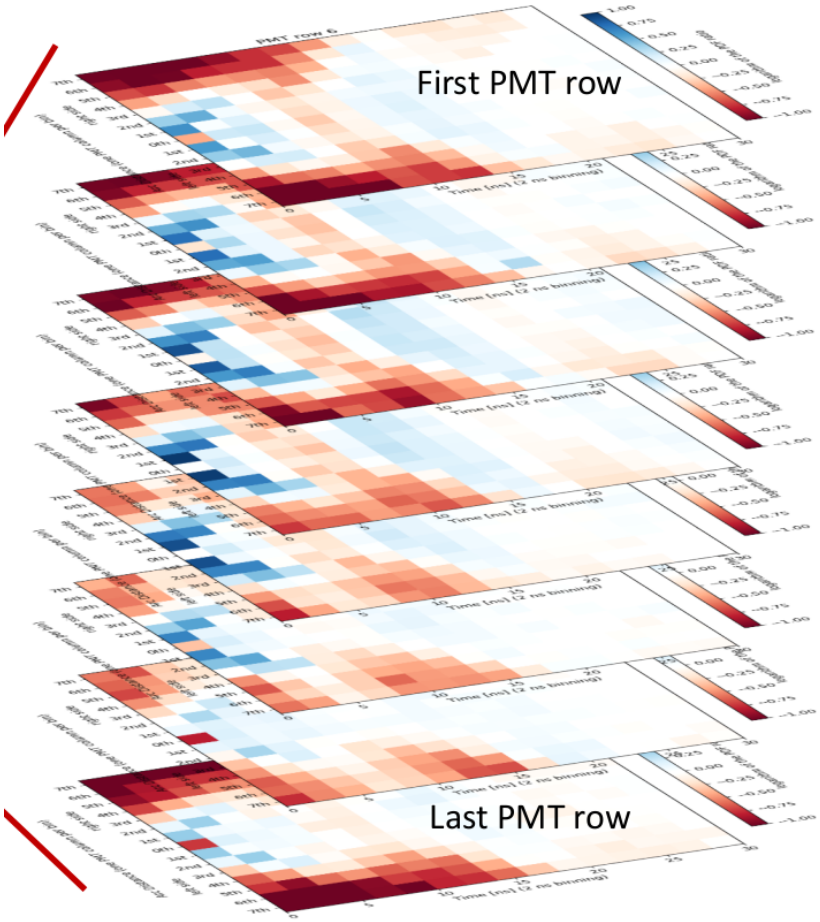

Figure 4.37: Implementation Ratio Map Gammas. All the 8 rows of PMTs

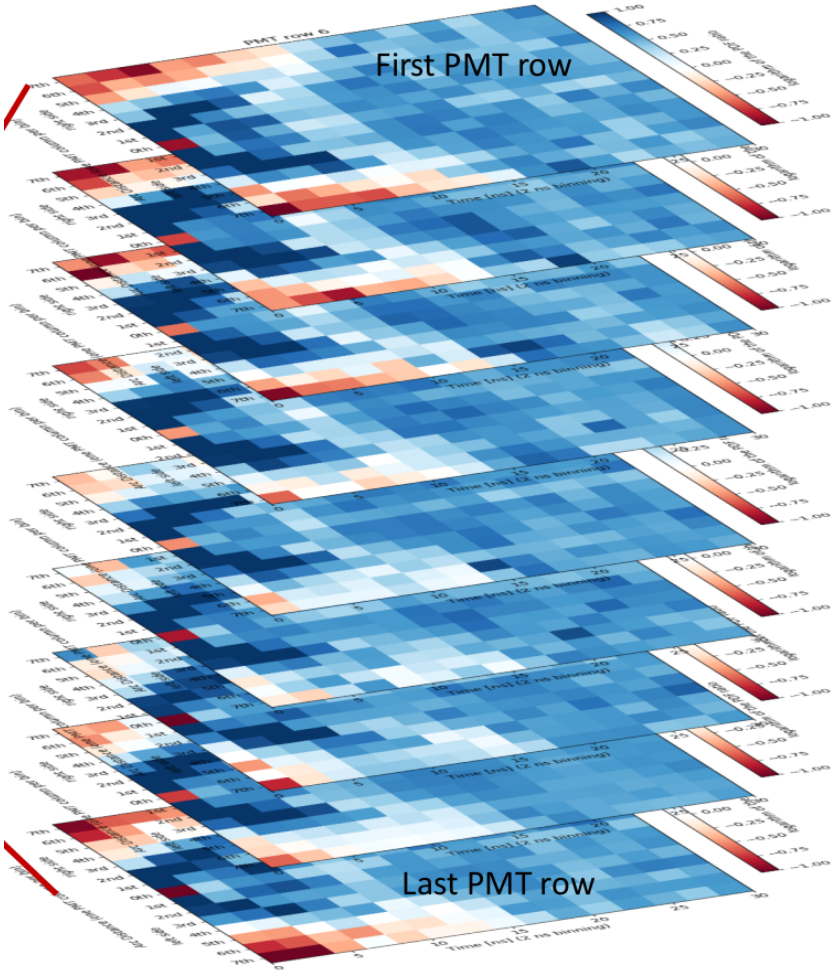

Figure 4.38: Implementation Ratio Map Beats. All the 8 rows of PMTs

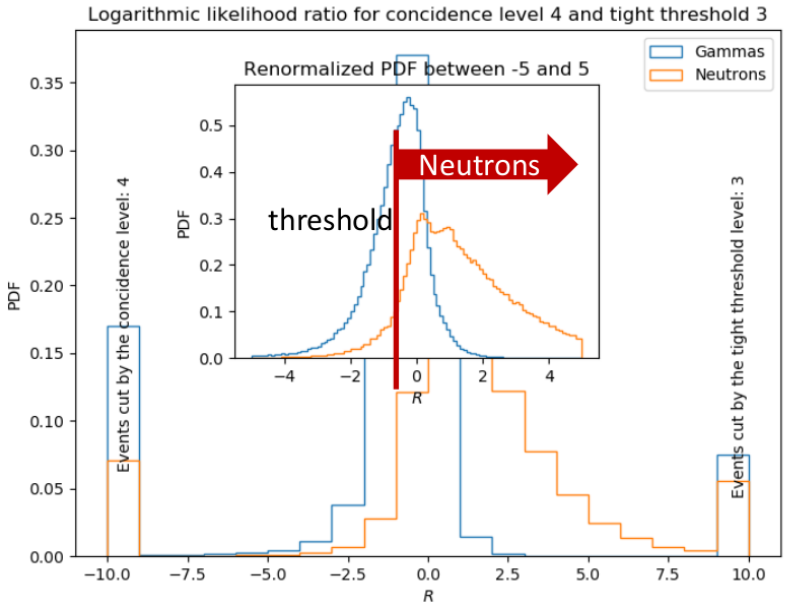

Figure 4.39: Example of the gammas background and neutron R distribution, with condition 1) = 4 and 2) = 3

Chapter 5

Data analysis

This chapter describes the tests carried out on the nVeto PMTs and the results obtained from the relative data analysis. Firstly, the working principle and the structure of the PMTs are discussed, then the quantities that characterize these instruments are illustrated; secondly the PMTs used in the Neutron Veto are described in more detail, and finally the tests carried out on the latter are illustrated.

5.1 The physics of photomultipliers

Photomultipliers (PMTs) are devices that convert a light signal into a measurable electric current. They are extremely sensitive and are often associated with scintillation detectors in nuclear and high energy physics [190]. A photomultiplier captures a flare of light, even a single photon, converting it into electrons, which are accelerated into a suitable electric field and then collide with metal electrodes and multiply. This last process is repeated many times thus producing an important electric current, that is an electric signal, which is collected on a suitable electrode. The working principle of PMTs is based on two physical phenomena: the photoelectric effect and the secondary emission. The first consists in the emission of electrons from a surface of a material when this is reached by light radiation. The second is the phenomenon observed when an electron hits an electrode causing the emission of other electrons. Such an electrode, where therefore a multiplication of electrons takes place, is called a dinode [191].
In this section the main characteristics of PMTs will be discussed, while in the next their use in the XENONnT Neutron Veto system will be discussed.

5.1.1 Photoemission

The phenomenon of photoemission, or photoelectric effect, can be divided into three phases (Fig. 5.1):

a) the absorbed photons transfer energy to the electrons in the material

b) the electrons diffuse into the material and lose part of their energy

c) some electrons reach the surface with energy enough to leave the material.

A photon of frequency ν and wavelength λ, which hits a material having extraction potential Λ, emits an electron with energy given by Einstein's formula:

$$E_c = h\nu - \Lambda \tag{5.1}$$

Not all photons incident on the photoemissive material cause photoelectric effect; the probability (or efficiency) of photoelectric conversion varies with the wavelength (λ) of the incident light and depends on the composition and thickness of the photoemissive material. The ratio:

$$n(\lambda) = \frac{n_e}{n_\gamma} \tag{5.2}$$

where n_e is the number of electron released and n_γ is the number of photons incident of the cathode, is called Quantum Efficiency (QE) and represents a fundamental parameter for photomultipliers. Since when the photon loses energy its frequency decreases, after a certain time it can no longer have a photoelectric effect. So, QE in always < 1.

Absorption of photons

When light hits a layer of photoemissive material, only a fraction of photons transfers energy to the electrons of the material; the remaining are reflected by the plate and do not contribute to the photoemission process. Metal surfaces are highly reflective in the visible region of the spectrum, while semiconductors have a low reflection coefficient.
In the study of the rate of absorbed photons, both the reflection coefficient of the material and the absorption coefficient must be considered; the latter, in addition to being dependent on the energy of photons, shows a dependence on the band structure of the material. In metals (Fig. 5.2) the conduction band, at low temperatures, is filled up to the Fermi level E_F while the higher

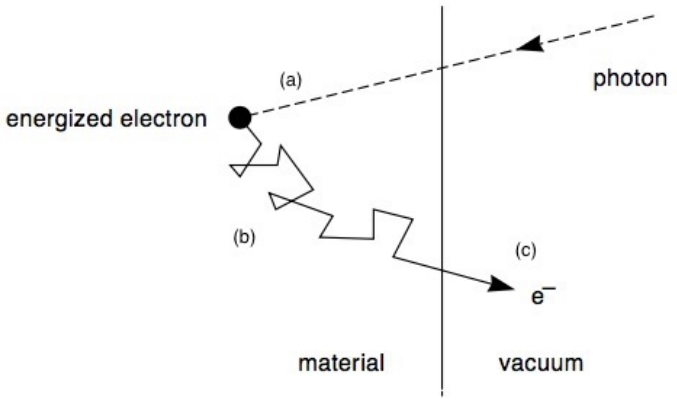

Figure 5.1: Photoemission

energy levels are mostly empty. In this case it is possible that the electrons of the conduction band are excited by the photons and then emitted in a vacuum; this phenomena is possible if the energy of the photons is greater than the energy separation between the Fermi level and the vacuum energy E_V.
In semiconductors and insulators, the Fermi level is in the prohibited band and the occupation of the conduction band, even at room temperature, is still too low to guarantee an appreciable photoelectric effect. Electrons can only be emitted from the upper levels of the valence band.
In a layer of thickness dx, the number of electrons n_e excited by the transfer of energy is proportional to the rate of absorbed photons $\Phi_p(\nu, x)$ as a function of the distance from the surface of the plate and the energy of the photons:

$$\frac{dn}{dx} = -\alpha_e \cdot \frac{d\Phi_p(\nu, x)}{dx} \tag{5.3}$$

Where α_e represents the fraction of absorbed photons that excite electrons; tipically for visible light $\alpha_e = 1$

Diffusion of electrons

The diffusion of electrons within the material differs if it is a metal or a semiconductor. The probability that an excited electron is emitted depends mainly on the processes that cause a loss of energy and characterizes the passage to the surface. In metals the conduction band is partially occupied by free electrons, in thermal equilibrium with the crystal lattice; excited electrons lose energy through collisions with other free electrons and return

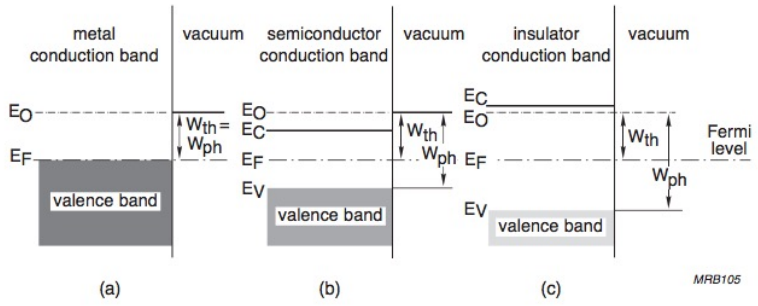

Figure 5.2: Energy bands in: (a) metals, (b) semiconductors, (c) insulators

to a state of equilibrium after traveling a relatively short distance. Since electrons require some energy to be able to leave the surface, only those that are excited near it can contribute to the photoemission process. The spatial region occuped by these electrons is called escape depth and is of the order of a few nanometers.
In semiconductors the conduction band is almost empty and the probability that excited electrons collide with other free electrons, during diffusion in the conduction band, is negligible. The loss of energy is mainly due to the interaction with the crystal lattice (with the creation of phonons) and is negligible due to the mass difference. Therefore excited electrons can travel long distances through the material before returning to thermal equilibrium. Once in thermal equilibrium, they travel equally long distances before recombining with the gaps and returning to the valence band.
The existence of the energy barrier on the surface makes the emission of electrons at equilibrium impossible, as in metals. Only electrons with excess of energy can escape. Since the energy loss through electron-phonon collisions is about 0.05 eV and the average free path between two collisions varies between 2.5 and 5.0 nm, the escape depth is a few tens of nanometers. It is possible to modify the energy barrier of certain semiconductors in order to achieve a negative electronic affinity and allow even electrons at thermal equilibrium (therefore having energy of a few kT beyond the lowest level of the conduction band) to be emitted. In this way, the escape depth becomes equal to the electron diffusion length at thermal equilibrium, reaching a size of a few micrometers.

Potential gap

To understand the mechanism by which electrons are emitted in vacuum, we can first consider the case of metals. In the conduction band all energy levels above the Fermi level are mostly empty (Fig. 5.3). The potential energy E_0 of an electron in vacuum exceeds the Fermi level E_F by a value W_{th} (thermoionic work function):

$$W_{th} = E_0 - E_F \tag{5.4}$$

To make the emission possible, an electron occupying the highest energy level in the metal must gain enough energy to overcome the potential barrier. The excess of energy can come from a temperature rise or from a photon. In the second case, the function W_{th} must be equal to the threshold energy of the photoelectric effect W_{th}. In a metal, therefore, photoemission occurs only if:

$$h\nu \geq W_{th} \tag{5.5}$$

For most metals W_{th} is greater than 3 eV; only for alkali metals it is sufficiently low to allow photoemission in response to visible light.
Let us now consider the case of semiconductors. The valence band, having upper limit E_ν, is completely full while the conduction band, having lower limit E_c, is empty. Therefore, a high emission efficiency can only be achieved by imparting sufficient energy to the electrons of the valence band to overcome the gap between the bands E_g and the electronic affinity E_A of the conduction band:

$$E_g = E_c - E_v \tag{5.6}$$

$$E_A = E_0 - E_c \tag{5.7}$$

Therefore in a semiconductor the reaction threshold is:

$$W_{pg} = E_g + E_A \tag{5.8}$$

always greater than $W_{th} = E_0 + E_F$.
The semiconductors generally have W_{th} between 5-6 eV being therefore sensitive to wavelengths of the order of 300 nm. It is also possible to reduce the work function by appropriately treating the surface of the semiconductor: for example, it is possible to absorb alkaline metals. In fact, there is a local change in the occupation of the energy levels due to the absorption which causes a "curvature" of the bands especially in the lower levels (Fig. 5.3). In case the semiconductor is also doped, the level minimum conduction can be

brought above the vacuum energy: we speak of apparent negative electronic affinity. It is therefore possible to excite the electrons to thermal equilibrium and cause their emission, since the threshold energy coincides with the energy of the gap ($W_{ph} = E_{th}$). By appropriately choosing the semiconductor and the surface treatment, it is possible to produce photosensitive materials even at multiple wavelengths and have an efficiency of higher emission. The Schottky effect is also often exploited whereby an external electric field reduces the potential barrier thus influencing the photoemission efficiency.

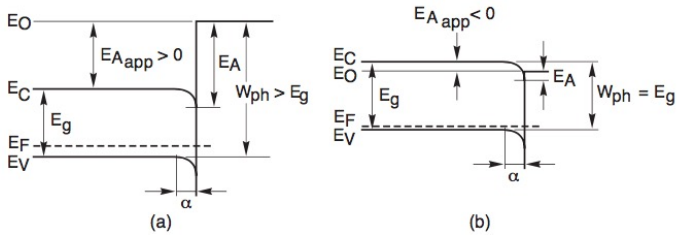

Figure 5.3: Energy bands for materials with (a) positive and (b) negative electronic affinity

5.1.2 Secondary emission

Secondary emission is a process that occurs following the absorption of electrons. Just as in the case of photoemission we can distinguish the three steps of absorption, diffusion and emission. The energy range of interest in this case is a few hundred eV. Primary electrons can lose energy according to three different processes:

• ionization of atoms in the lower energy levels: these are all the elastic and inelastic collisions between atoms and electrons

• X-ray emission in the filling of the internal shell; these can partly be emitted and partly excite other electrons

• excitation of electrons of the levels of the valence band.

The depth of penetration R into the material is given by:

$$R = \int_{E_0}^{E_p} \frac{dE}{|dE/dx|} \tag{5.9}$$

The energy loss of the primary electrons of energy E_p (for low energy electrons) can be roughly described by:

$$\frac{dE}{dx} = -\frac{E_p}{R} \tag{5.10}$$

Instead, the density of free electrons can be assumed proportional to the energy loss of the incident photon, according to:

$$\frac{dn}{dx} = \frac{1}{\epsilon}|\frac{dE}{dx}| \tag{5.11}$$

where n is the number of free electrons and ϵ is the average energy required to generate the electron-hole pair.
The released electrons then migrate to the surface. When doing so, they lose some of their excess energy by collisions with other electrons and by interactions with the lattice. Only the electrons that reach the surface with energy greater than the potential barrier contribute to the secondary emission. The closer the excited electrons are to the surface, the greater is their possibility to escape. In addition, the number of total excited electrons increases proportionally to the initial energy of the primary electrons. The ratio between the number of secondary electrons emitted and the number of primary electrons is called "secondary emission coefficient" δ.
The characteristics of the metals for photoemission are also found in the secondary emission mechanism: they have a low escape depth (3 nm) and an equally low secondary emission coefficient.
Semiconductors and non-conductors, which have low potential barriers, are instead good secondary emitters.

5.2 Outline of PMTs structure and functioning

Figure 5.4 shows the most important elements that make up a photomultiplier [190]. Among them we note:

• a photocathode made of a photosensitive material which converts a photon flow into an electron flow

• an electron collection system that focuses and accelerates electrons

• an anode that collects electrons and produces the output signal

When a photon, coming for example from a scintillation phenomenon, hits

the photocathode, an electron is emitted by photoelectric effect. At the ends of the phototube there is a potential difference distributed between the various dinodes (Fig. 5.5); for this reason, the emitted electrons goes to the first dinode after being focused and accelerated. Here, following the collision, the secondary emission takes place and the generated electrons are in turn accelerated towards the second dinode and so on. This generates a cascade of electrons that reaches the anode where it is collected to produce a current.

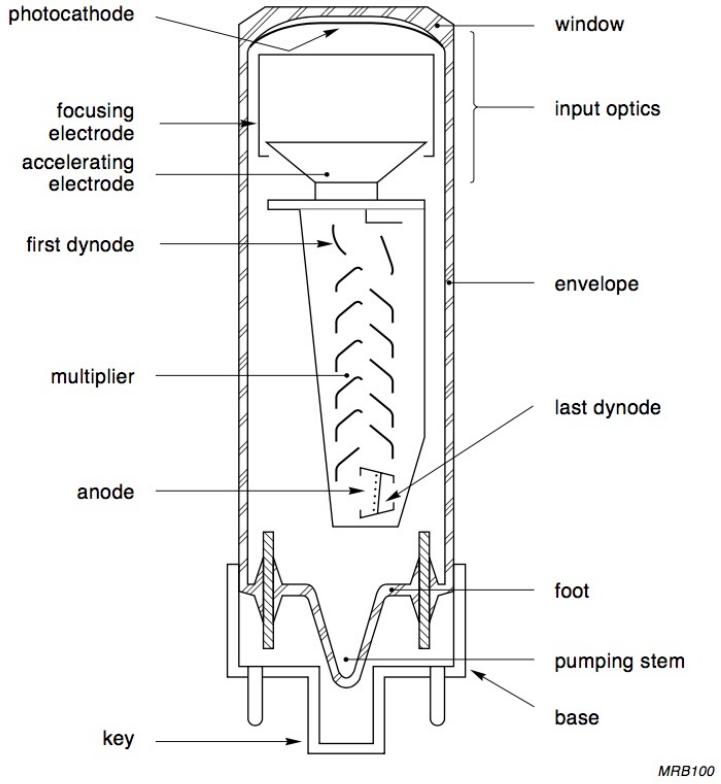

Figure 5.4: A schematic view of a photomultiplier tube (PMT)

5.3 PMTs operating parameters

In the use of photomultipliers, reference is often made to a series of parameters that summarize their efficiency and operation in the different lighting regimes. In this section the most common parameters will be defined [190].

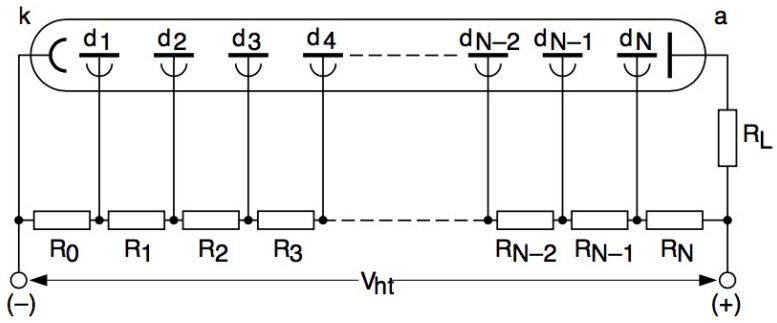

Figure 5.5: Voltage partitor in a PMT

5.3.1 Gain

In a photomultiplier, the ratio between the number of electrons collected at the anode and the number of photoelectrons emitted at the cathode is defined as "gain". The amplification factor of a dinode is also known as the secondary emission factor δ; the latter represents the number of secondary electrons emitted as a result of interaction with the primary electron from a previous dinode. The secondary emission factor is proportional to the voltage between the two dinodes according to:

$$\delta \propto (V_d)^{\alpha} \tag{5.12}$$

Where α is a corrective factor, typically $0.65 \leq \alpha \leq 0.75$

If the number of photoelectrons hitting the first dinode is n_k and the gain of the dinode is δ_1, then the number of secondary electrons will be $n_k\delta_1$; if the second dinode has a gain of δ_2 there will be $n_k\delta_1\delta_2$ electrons and so on up to the anode; if N is the number of dinodes then the number of electrons collected at the anode is

$$n_{anode} = n_k = \Pi_{i=1}^{N}\delta_i \tag{5.13}$$

The amplification factor is simply given by the ratio between n_{anode} and n_k, i.e. the product of the gains of the single dinodes:

$$G = \Pi_{i=1}^{N}\delta_i \tag{5.14}$$

Assuming that the emission factor is the same for all dinodes, we have:

$$G = \delta^N = [A(V_d)^\alpha]^N = \frac{A^N}{(N+1)^{\alpha N}} V^{\alpha N} \propto V^{\alpha N} \tag{5.15}$$

with A proportionality constant and V supply voltage of the phototube which, being distributed between the dinodes (Fig. 5.5), holds $V = (N+1)V_d$ Most PMTs contain 10 to 14 dinodes with an overall gain of the order of 10^7. It is now necessary to justify the assumption of uniformity of the secondary emission factors of the various dinodes in (5.14): ideally, the electron multiplier should provide a constant gain, fixed energy, for all electrons that enter in the dynode; in practice this does not happen due to the statistical nature of the secondary emission process. Electrons having the same energy and interacting with the dinodes will produce different numbers of secondary electrons and therefore a fluctuation in gain.
In order to estimate the intensity of the fluctuations, the single electron spectrum is used; this represents the spectrum of the output signal from the PMT in response to the entry of a single electron into the multiplier. It can be obtained by lighting up the PMT with weak light so that the probability of producing more than one photoelectron is negligible.
For each single electron event there will be different waveforms. By integrating each current pulse we obtain the total charge and therefore the gain of each event. Analytically the single electron spectra (Fig 5.6) are represented by the Polya distribution (also called negative binomial).

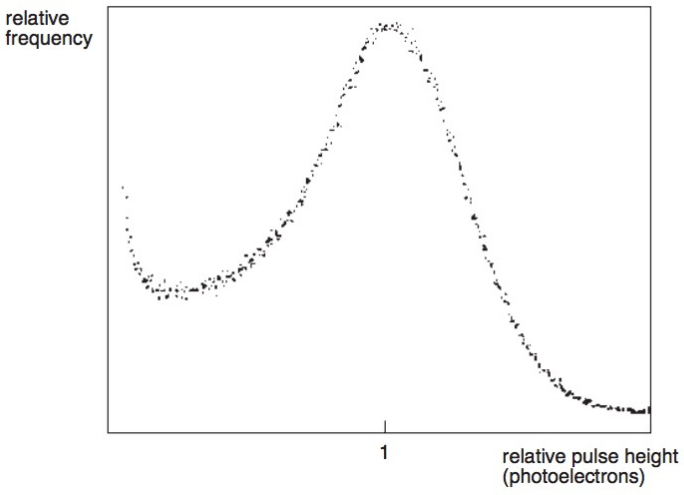

Figure 5.6: Single electron spectra

5.3.2 Linearity

The linearity of a PMT strongly depends on the configurations of the dinodes and on the current in the tube. In general, the electron flow of the previous step is required to be completely collected in the next one, in order to maintain a proportionality with respect to the initial cathode current. The collection of the flux also depends on the voltage between the various electrodes: the functional dependence of the anode and cathode currents as a function of the voltage for various illuminations is shown in Fig. 5.7).
The current grows as the voltage applied increases up to a saturation level, which is reached when all the current is collected. The initial dependence on the potential is due to the formation of a charge accumulation around the electrode; this electronic cloud tends to shield the field of the region and is attenuated only by increasing the applied voltage.
We can assume that the cathode, dinode and anode current is, in conditions of use of the device, in the saturation region of the characteristic curve. In keeping these voltages, however, attention must be paid to the trend of the current in the tube. The resistivity of the photocathode, for example, is a very important factor: it is normally high, in the order of a few tens of $M\Omega$; for this reason, the emission of small currents of photoelectrons can cause a large variation in the potential of the photoemissive membrane, changing the potential difference with the first dinode and altering the collection efficiency. Another problem is represented by the presence of the load resistance connected to the anode, which causes that the voltage decreases as the current increases; this would cause a variation in the potential difference between the last dinode and the anode. To prevent these phenomena it is necessary to work in certain current and voltage ranges.

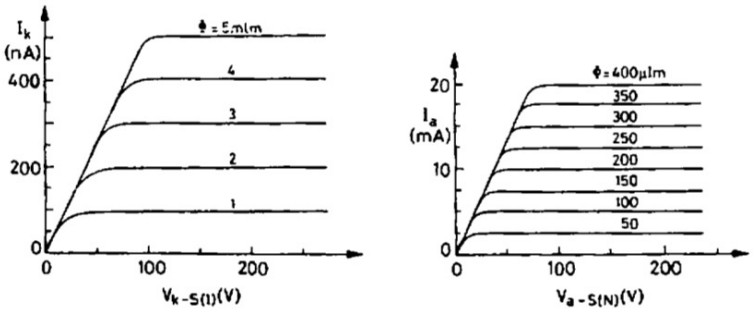

Figure 5.7: Current-voltage characteristics of the cathode and anode in a PMT under different illuminations

5.3.3 Response Time and Resolution

There are two main factors that influence the temporal resolution of photomultipliers:

- changes in the transit time of the electrons in the phototube
- fluctuations due to statistical noise

The first factor can arise from both the difference in the path that the photoelectrons make to reach the input system, and from the energies with which they are emitted.
The difference in the path is also enhanced by possible asymmetries of the dynode, so the difference in transit time is related to the geometry of the system.
One way to solve this phenomenon is the use of spherical cathodes in order to equalize the distances. Alternatively, you can think of applying a variable electric field that grows as the distance from the phototube axis increases. In addition to the geometric effects, variations depending on the energy and direction of the emitted electrons may occur. This effect, different from the previous one, is independent of the position in which the photoelectrons are emitted and depends only from the initial speed expressed as the sum of the two components in the directions perpendicular and parallel to the axis:

$$v_{\parallel} + v_{\perp} \tag{5.16}$$

The time difference can be expressed as:

$$\Delta t = \sqrt{\frac{2m_e W}{e^2 E^2}} \tag{5.17}$$

where $m_e = 9.1 \cdot 10^{-28} g$ is the mass of the electron, and $e = 1.6 \cdot 10^{-19} C$ is the charge of the electron, E is the modulus of the electric field [V/m] and finally W is the kinetic energy associated with the component of the normal speed at the photocathode, that is $v_{\perp}/2m_e$. For some typical values $E = 4$ kV/m, $W = 0.4$ eV, $\Delta t = 0.5$ ns.

5.4 PMTs noise

In this Section will be illustrated possible phenomena that could interfere with current and voltage mesaurement, limiting their accuracy. These phenomena are the Dark Current, the Afterpulses and the statistical noise [190].

5.4.1 Dark current

The Dark Current is the current that passes through the anode circuit when the voltage is applied to the photomultiplier, in the absence of light. It has two components: the first is continuous and is due to dispersion on the glass and non-conducting surface, the second is discontinuos and consists of pulses of a few nanoseconds. The Dark Current varies both according to external conditions (applied voltage, gain, temperature, humidity, etc.) and according to the past use of the PMT (past lighting conditions, etc.). In some cases these are temporary effects, while others may be permanent. The latter are:

- Leakage currents
- Thermoionic emission
- Radioactive contamination
- Light phenomena

of which thermal noise is the main component.

The contribution of the thermionic emission is described by the Richardson's equation:

$$I = AT^2 \cdot e^{\frac{-e\Phi}{kT}} \tag{5.18}$$

where A is a constant, T is the temperature, k is the Boltzmann constant and Φ is a constant that has the dimensions of an energy for unit of charge and is linked to the threshold energy of the photoelectric effect. Clearly the decrease in temperature involves a reduction of this component.
The radioactive materials of which the glass or the support are made can cause the emission of electrons in the photocathode or in the dinodes. The so produced radiation can either directly hit the electrodes or cause the fluorescence of the glass. In both cases a small current is measured. In general, when referring to the Dark Current, we refer to currents of the order of some nanoampere.

5.4.2 Afterpulses

Afterpulses, as the name suggests, are signals that appear in the wake of a real pulse. Afterpulses have two main causes:

• Light reactions

• Ionization of residual gases

which can be distinguished according to the time that separates the Afterpulse from the real signal.

Light reactions

An electrode hitted by electrons emits photons. Although the luminous efficiency of these phenomena is very low, in some tubes it is possible that the light emitted, even in the final steps of the multiplication chain, may go back reaching the photocathode and originating the Afterpulse signal. The latter will be delayed with respect to the real signal by the sum of the transit time of the electrons and the time of photoemission process (typically it is 20-100 ns).

Ionization of residual gases

To ensure that the cascade of electrons does not lose energy by interacting with air, a vacuum is maintained in the photomultiplier. However, it may happen that residual gases inside the phototube are ionized by electrons in their motion, causing an afterpulse signal. These traces are for example due to emissions of the materials that make up the structure. The ions generated (usually H_2^+, He^+ or CH_4^+) go to the cathode where they can cause the emission of other electrons. The time difference between the real signal and the afterpulse is given by the transit time of these ions; the latter depends both on their mass and on the electric field present within the PMTs).

5.4.3 Statistical noise

The statistical nature of the phenomena that chartacterizes the physics of the photomultipliers represents the main cause of noise, which cannot be reduced. For a given photon flux the number of emitted photoelectrons, as well as that of secondary electrons, fluctuates over time; as a direct consequence, the current to the anode will fluctuate around an average value (Fig. 5.8).
The intensity of the noise is measured by the variance of the fluctuations of the anode current around the average value.
Statistical fluctuations in a PMT can originate in the photocathode or dinode system. In the first case they are related to the statistical nature of the photoelectric effect; the fluctuations can then be calculated by assuming a

Poisson distribution for the number of photons hitting the photocathode in the time interval τ and a binomial distribution for the number of photoelectrons released. To this noise are added the fluctuations originated in the multiplier: these are not only due to the statistical nature of the secondary emission, but also to the differences in the transit time of the electrons and in the non-uniformity of the secondary emission factor. The intensities of these fluctuations can be estimated by taking into account the single photo-electron spectrum. In any case, the latter component is negligible, contributing only 10% to the statistical noise.

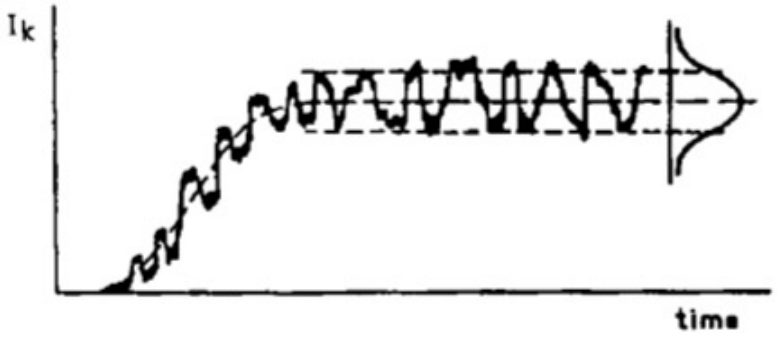

Figure 5.8: Fluctuations in the current signal

5.4.4 External factors

Some sources of external noise can be attenuated with a correct use of the photomultiplier in the right external conditions. In addition to exposure to external light, attention should also be paid to the presence of magnetic fields and external temperature.

5.5 Neutron Veto PMTs

The Neutron Veto photomultipliers are the key components of a part of the XENONnT experiment necessary to complete the radiogenic background mitigation. Indeed, the Neutron Veto will be instrumented with 120 high-QE low-radioactivity Photomultiplier tubes (PMTs) to detect the Cherenkov light emitted after the neutron capture on gadolinium and water. 125 PMTs were bought in order to have at least 5 spare PMTs [254]. So, PMTs used for the Neutron Veto are 120 in total. Of these, 115 are "standard" PMTs, while the remaining 5 are called "Reference PMTs" (we will see later why

they are called so). These PMTs were produced by the Hamamatsu company and they are 8" PMTs, R5912-100-10. PMTs used for the Neutron Veto are essentially the same PMTs also used for Muon Veto (MV), with the exception of some improvements: that is, it has been used as a low radioactivity and waterproof glass material, and in addiction there are two coaxial cables, one for signal and one for HV, each with its own shielding system even if they are connected together. Not only that: some modifications have also been made to the resistive chain: in fact, 100 Ω discharge resistors and a protection resistance of 10 $k\Omega$ have been used [260]. In Fig. 5.9 are reported the main sources of radioactivity for nVeto PMTs.

Unit: Bq/PMT

	Other than glass		Standard glass		Low rad. glass		Assembly parts	
	Hamamatsu	LNGS	Hamamatsu	LNGS	Hamamatsu	LNGS	Hamamatsu	LNGS
K-40	0.6	0.08	4.7	2.4	0.8	0.6	1.0	–
U-series	> 0.1	<0.05	2.4	2.26	0.4	<0.6	0.8	–
Th-series	> 0.1	0.008	2.0	1.58	0.3	0.425	1.3	–

Figure 5.9: Main sources of radioactivity for Neutron Veto PMTs

5.5.1 Small water tank

nVeto PMTs are are contained within the so-called Small Water Tank (SWT). The SWT is a cylindrical polypropylene light-tight tank of 1 m height and 1.7 m diameter (see Fig. 5.11) with the inner surface covered by a black PVC layer for the light absorption. On the lateral side of the SWT there were several feed-through (Fig. 5.11 on the right), used to pass both the 30 m PMTs' cables and the optical fibers for the LED calibration. In addition, in the middle of the tank cover, there was a feed-through for the diffuser ball (see section 5.2.2). The SWT was also supplied with a connection for the filling/emptying of ultra-pure water; the latter was stored in the blue tank visible in Fig. 5.11.

5.5.2 Calibration setup

The calibration setup for the measurements of the spectral response of the PMTs exploits a Diffuser Ball paired with a LED box (emitting blue light with $\lambda \approx 470$ nm). The diffuser ball is a 50 mm diameter PTFE hollow sphere filled with micro-glass bubbles (Fig. 5.12); this property allows for a homogeneous diffusion of light inside the Small Water Tank. To make the

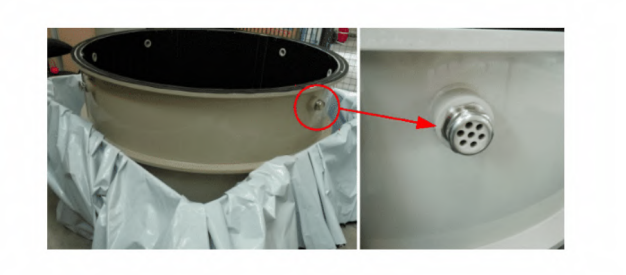

Figure 5.10: Photo of the Small Water Tank with the zoom on the feed-through (right) used to pass the PMTs cables.

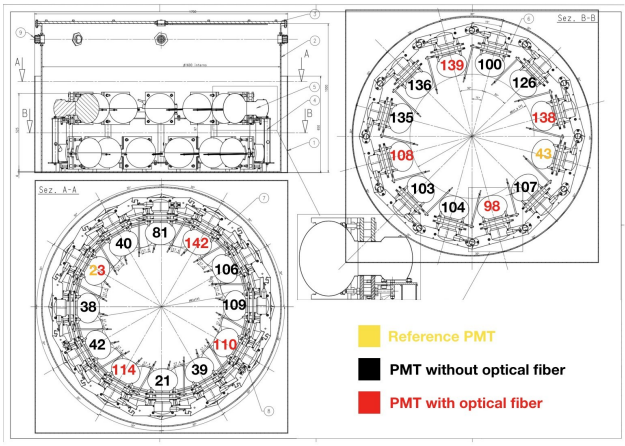

Figure 5.11: Drawings of the Small Water Tank with the PMT structure inside

PMTs to receive the same amount of light, the diffuser ball was hanging in the middle of the structure. For the sake of measurement redundancy, an optical fiber bundle was installed (see Fig. 5.13), consisting in 8 optical fibers installed on 8 PMTs using the interface shown in Fig. 5.14: a stainless steel (SS) rod holds the optical fiber and at the edge, a PTFE reflector focuses light toward the PMT photocathode.

5.5.3 Electronics and DAQ

The electronics system used for the tests, illustrated in Fig. 5.15, consisted of:

• Pulser BNC Model 588 which provided both the signal for the LED and the external trigger for the DAQ. It also sets the amplitude and width configurations for adjusting the light intensity of the LED

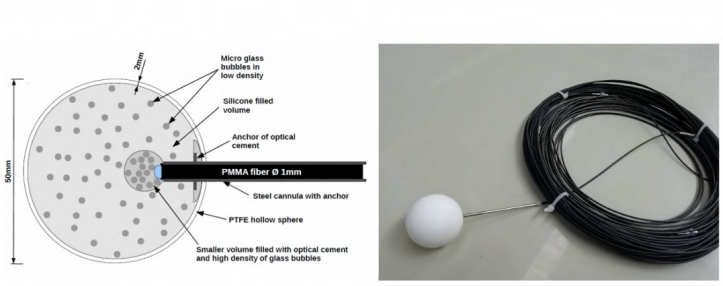

Figure 5.12: Scheme of the diffuser ball. A PMMA optical fiber goes inside the sphere and the light coming out from the fiber is diffused by micro-glass bubbles. It is possible to distinguish two areas of different bubble glass density

- 2 LED boxes (1 $k\Omega$ internal resistor, positive supply voltage)

• One Mainframe CAEN Power Supply SY4527
- One Board A1535SP which provided 24 SHV Channels

• HP PC Server with 2.2 TB storage disk

• VME Crate
- one VME Crate controller through optical link card CAEN mod. A3818
- Four 8-channels Digitizer CAEN mod. V1751

In Fig. 5.16 is summarized the electronic setup. The pulser (green on the top left) with its 8 programmable channels provided both the triggers to the LED boxes (connected to the two calibration systems) as well as the trigger for the DAQ. The TTL signal was first connected to a TTL-NIM converted module and the NIM output inserted in the TRG-IN channel of the first digitizer (Board 0 - Master Board). Thus the daisy chain of the TRG-OUT/TRG-IN distributed the trigger to the other boards. Even the internal clock of the Master Board is distributed through a daisy chain to the Slave Boards (board 1-3). Each board featured 8 channels; since we had 24 PMTs for each bunch, three board (0-2) would have been enough. However, in order to study the trigger delay/jitter between the boards, a fourth digitizer was employed. Its channels were filled with the trigger signal. All the boards were connected via an optical link (grey lines) to the PC server. It should be noted that, although this scheme was used for the main measurements, in some cases, e.g. the study of the PMTs' time characteristics, it was employed a slightly

Figure 5.13: The optical fiber bundle

different setup.

5.5.4 nVeto PMT tests

As already mentioned before, nVeto set consists of 125 PMT in total, divided into 6 groups, called bunches, of 24 PMT each used individually in different stages of the analysis, with the addition of 2 PMT used as a reference for the entire analysis period; in the last group we tested again some PMTs and installed a shield for the magnetic field. The sequence of operations was like the following:

• 1 week: unmounting/mounting + cabling, turning ON the DAQ. PMTs set at nominal HV

• 1.5 days: gain + DR + afterpulse + gain/DR with different HV (7 points). Measurements in air

• 0.5 day: filling SWT with water

• 1 day: gain + DR + afterpulse. Measurements in water

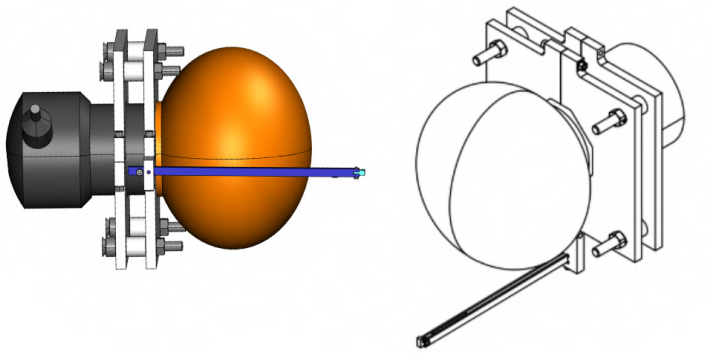

Figure 5.14: Drawings of the nVeto PMT with the polyethylene supports (white/grey) and the SS rod for the optical fiber (blue). At the end of the bar is located a small PTFE reflector (light blue) used to focus the light from the fiber on the PMT photocathode (orange)

• 2 days: gain + DR + afterpulse + gain/DR with different HV (7 points). Measurements in water with PMTs at same gain

• 2 days: gain monitoring and/or repeat some measurements

NV PMT test was finished in 3 months, from April to June 2019

5.6 Results of Data Analysis

In this Section are illustrated the results of the tests that have been carried out to characterize the R5912 Hamamatsu PMTs' response, in view of their future installation inside the Neutron Veto. By characterization of PMTs the main operating parameters (see Section 5.1) have been measured, such as:

• the gain and its stability over the time

• the dark counts rate at different thresholds

• the transit time difference between the PMTs and its spread

• the monitoring of the afterpulses

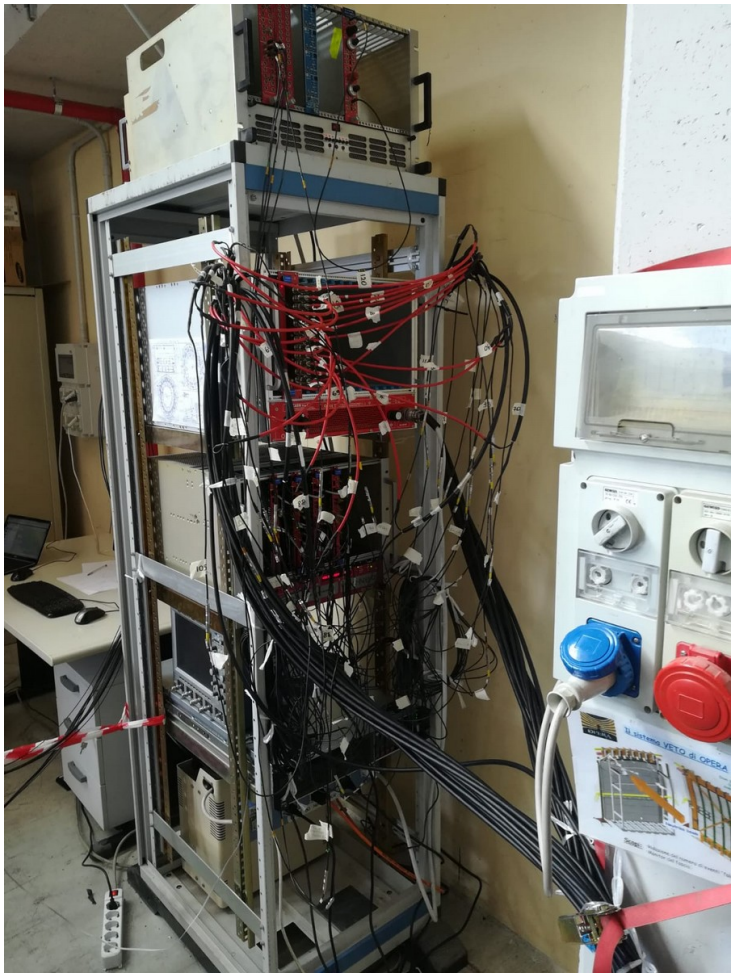

Figure 5.15: The Electronic System

As already mentioned before, the 125 Neutron Veto's PMTs are divided into 5 groups, called bunches, of 24 photomultipliers each. There are also 5 PMTs, called "reference PMTs", which are moved from one bunch to another in order to verify that the data external conditions do not change as the bunch changes. For each bunch, various "runs" of data taking were carried out, of different types, depending on the parameter measured. These runs were performed in different data-taking conditions, depending in particular from the voltage to which the PMTs are subjected and from the type of calibration used. In the data analysis discussed in this thesis only the runs with the type of calibration "with diffuser ball" have been considered, with two different ways of choosing the voltage of the PMT, or "nominal voltage" (NHV), that

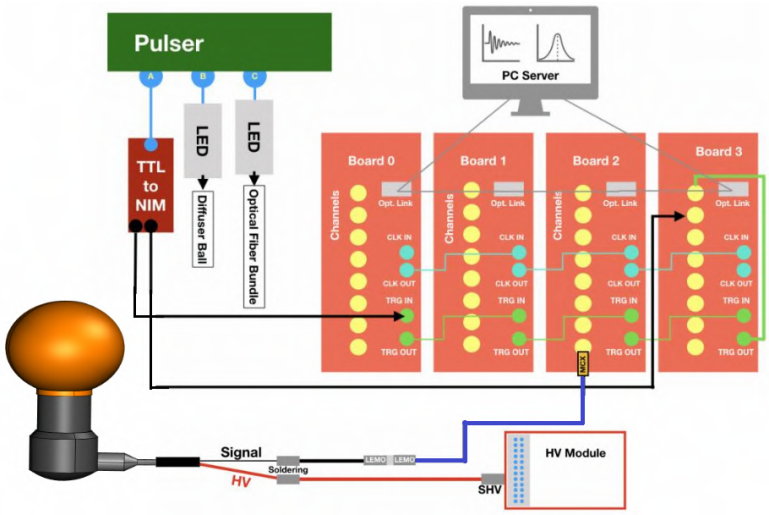

Figure 5.16: Schematic of the electronic setup employed for the main measurements in the SWT test

is the voltage that are on the data-sheet of PMTs, and "voltage at the same gain", that is for the latter choosing for each PMT the voltage applied in such a way that all the PMTs have the same gain, or $6.24 \cdot 10^6$. For each run and for each PMT some events were produced. Each event was produced as follows: a light pulse was generated with the LED, this pulse is sent to the PMT, then an acquisition window (of duration depending on the type of run considered), is opened, slightly ahead of the light pulse. The digitizers then digitize everything the PMT sees, or its signal.

5.6.1 Gain measurements

The gain is a key parameter for the characterization of the PMTs' behavior. The gain measurements for every PMT were oriented to monitor the stability of this parameter and to check possible variations in water, in view of the installation in the long term final configuration inside the Neutron Veto. The high voltage dependence of the gain was also studied and the calibration curves measured; the latter will be very useful during the PMT installation in the final setup [254].
The LED runs dedicated to the gain measurements was called "single photoelectron runs". These runs were characterized by an illumination such that only one photoelectron is emitted at the photocathode. The illumination was provided by the diffuser ball. The acquisition characteristics were the following:

• Acquisition window of 1 μs

• Trigger Rate of 1 kHz

• 100k Events

• No Zero Length Encoding suppression

For each event the waveform was produced; a typical single p.e. waveform is shown in Fig. 5.17. From the integration of the signal in the expected region, one obtains the charge of the event. The integration is made starting from the calculation of the baseline obtained averaging 100 samples before the signal integration region (red line in Fig. 5.17). In this way, we got rid of the low-frequency environmental noise that was constantly present in the Assembly Hall area. Since we knew the light pulse timing (from a check with the oscilloscope), it was easy to define a window for the peak finding algorithm: the peak was defined as the minimum value of the waveform inside a specially chosen range. Thus the integration window was defined as a specially chosen range starting from the minimum (from -10 ns to +64 ns). An exemple of distribution of the integrating charge for 100k events, i.e. a single p.e. spectrum is shown in Fig. 5.18. Every single p.e. spectrum was fitted by a proper function; it consists mainly of a gaussian noise, called pedestal, centered in 0 pC and of a second gaussian centered around the single p.e. charge value. With growing illumination, it is possible to distinguish also a third gaussian peak that takes into account the double photoelectrons contributions and whose parameters are constrained by the ones of the single pe function. Finally, the exponential function takes into account the sub-amplified electrons' contribution. Usually, it is associated with the photoelectron energy loss for the inelastic scattering on the first dynode; the electrons produced have low energy, causing a sub-amplified signal at the end of the chain. A similar effect is also caused by the photoelectrons that skip one dynode of the chain. The composed fit function reads:

$$f(x) = A_{ped} e^{\frac{-(x-\mu_{ped})^2}{2\sigma_{ped}^2}} + (e^{-p_0 x + p_1} + A_{spe} e^{\frac{-(x-\mu_{spe})^2}{2\sigma_{spe}^2}})\Theta(x) + A_{dpe} e^{\frac{-(x-\mu_{spe})^2}{2\sqrt{2}\sigma_{spe}^2}} \tag{5.19}$$

where:

• A_{ped} , μ_{ped} and σ_{ped} are the normalization constant, mean value and standard deviation of the pedestal

• A_{spe} , μ_{spe} and σ_{spe} are the normalization constant, mean value and standard deviation of the single p.e. peak

• p_0 and p_1 are the exponential parameters

• A_{dpe} , $2\mu_{spe}$ and $2\sigma_{spe}$ are the double p.e. parameters, of which only the first one is a free parameter

• $\Theta(x)$ is the Heavidse function

The gain values are obtained from the fit parameters, in particular from the μ_{spe} and the μ_{ped}:

$$G = \frac{\mu_{spe} - \mu_{ped}}{e} \tag{5.20}$$

where e is the electron charge. The error associated is given by the error propagation:

$$\Delta G = \sqrt{(\frac{\partial G}{\partial \mu_{spe}}\Delta\mu_{spe})^2 + (\frac{\partial G}{\partial \mu_{ped}}\Delta\mu_{ped})^2} \tag{5.21}$$

The distribution of the gain values for the 125 PMTs at their NHV is shown in Fig. 5.19
The PMT characterization in terms of gain foresaw also the measurement with a different HV value, i.e. the voltage for which the PMTs are expected to have the same gain. In particular, we wanted to check the settings to have a gain equal to $6.24 \cdot 10^6$, which is the value of a single p.e. centered in 1 pC. To obtain the high voltage values that fulfill this condition, the Gain-High Voltage curves were needful.
The relationship between Gain and HV was also studied from gain measurements with different applied voltages. Thus, 7 points starting from the NHV and subtracting/adding 150 V, 100 V, and 50 V, were collected. The Gain-HV curves for one bunch of PMTs are shown in Fig. 5.20; the trend is in correct agreement with the expected function:

$$ln(G) = ln(k) + \alpha ln(V) \tag{5.22}$$

thus, the trend was verified by a linear fit function. Instead, the HV values in order to have a gain of $6.24 \cdot 10^{equation}$ were calculated reversing the previous equation:

$$HV(SameGain) = exp(\frac{ln(G) - ln(k)}{\alpha}) \tag{5.23}$$

where ln K and α are the parameters of the linear fit function.
Another important feature that the PMTs must satisfy is their performance stability. The gain stability was checked with several runs (called "Gain monitoring" runs) automatically acquired during the night and the weekends when a regular data taking was not necessary scheduled. Each PMT was tested at least for 9 days; so for most of the PMTs only the short-terms stability was checked.

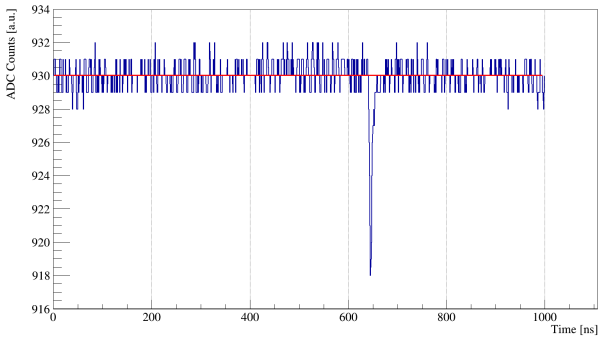

Figure 5.17: Typical signal waveform of one PMT recorded with a single p.e. run. The duration of each event was 1 μs. On the y-axis are reported the ADC counts but since we know that for the digitizer employed 1 ADC Count $\approx$ 1 mV it is easy to find the corresponding voltage value. On the x-axis instead should be reported the sample number, but since we had a time resolution of 1 ns, one sample corresponds to 1 ns; thus the time is reported. The red line indicates the mean baseline which is used for the integration algorithm

5.6.2 Dark rate measurements

Dark counts are the signals generated by the PMTs in the absence of light [254]. At room temperature, the thermionic emission of electrons is the major source of dark counts. In the experiments where the expected event rate is very small, knowing the dark counts rate is important to predict the fake coincidence rate. The dark rate (DR) depends on a threshold which in turn is expressed in a fraction of photoelectrons. During the SWT test we performed measurements of the dark rate on runs without illumination and with the following characteristics:

- Acquisition window of 10 μs

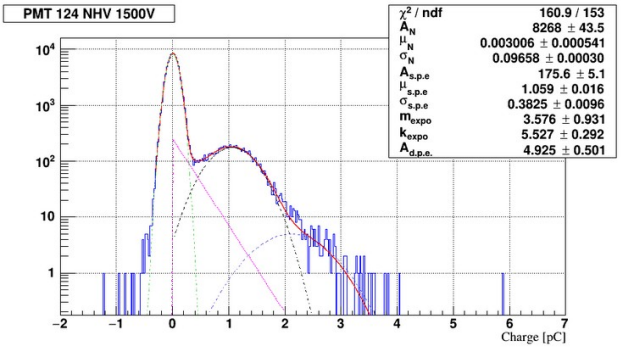

Figure 5.18: Fit of the charge spectrum of an spe run for a PMT shown as a reference. The red curve is the fit function, convolution of the function reported with the colored dashed lines. The distribution shows at least two peaks. These are the spe peak, fitted with the black gaussian function, and the pedestal (noise) peak which is linked to the integration of the events without signals. The pedestal is fitted with the green gaussian function. Sometimes a third peak appears; it is linked to events where two photoelectrons are emitted from the photocathode, instead of one. The fitting function is again a gaussian highlighted in blue. In addition, there is an exponential function (defined for Charge ≥ 0) colored in pink, to account for the sub-amplified electrons. All the fit parameters and the χ^2 are also reported

- Trigger Rate of 0.5 kHz
- 100k Events
- Zero Length Encoding ± 1 ADC count

The acquisition window was longer with respect to the one employed for the gain runs; this was decided in order to have enough statistics and thus a reasonable error from the counting ($\sim 10\%$). Another difference from the gain runs is the presence of the Zero Length Encoding suppression of all the samples of the waveforms inside the Baseline $\pm$ 1 ADC count threshold.
The usual way to measure the dark rate is just to count the waveform peaks over an ADC threshold and eventually with a Time-Over-Threshold (TOT). However due to a low resolution in terms of vertical axes of the waveforms (i.e. ADC Counts) it was decided to also exploit the charge spectra 3 rather than counting the peaks directly from the waveform. This idea is based on the fact that the dark rate pulses coming from thermionic emission are of

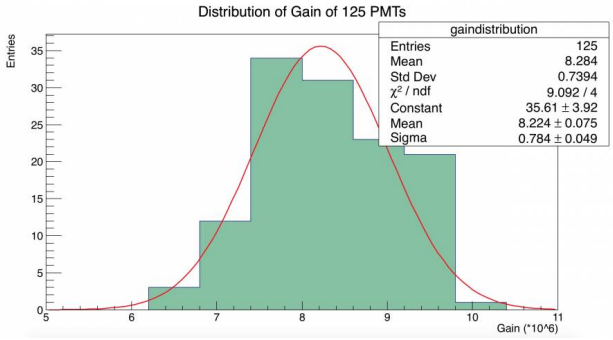

Figure 5.19: Distribution of the gain values at NHV for the 125 PMTs tested. The mean gain is $(8.22 \pm 0.07) \cdot 10^6$

single p.e. nature [259]. Thus the analysis procedure was divided in:

• setting a DAQ threshold for the peak finding (see Fig. 5.21)

• integration of the waveform peaks

• fit of the charge spectrum obtained with a single Gaussian function. The mean value represents the charge of 1 p.e.; thus the charge of its fractions are also known

• counting of the entries above the software threshold; the corresponding error is the square roots of the counts.

In particular, with DAQ threshold we refer to the ADC Count and TOT set as shown in Fig. 5.21, while we call software threshold the one of the single p.e. fractions to calculate the DR.
To carry out the dark rate measurement, a peak-finding algorithm was developed, using a DAQ threshold of 3 ADC counts, A TOT of 3 ns and an integration time from Uptime -10 ns (Uptime) to +64 ns (Downtime) and finally a software threshold of 0.5 p.e.. Furthermore, 128 ns were skipped after each peak. It was measured a mean DR over 125 PMTs of $\sim$ 2.5 kHz. In Fig. 5.22 is illustrated the Dark Count Rate measured for 25 PMT of Bunch 1, as a reference.
For each PMT, it was also studied the dark rate varying the software threshold. The dark rate values for each threshold for PMTs of bunch 1 are reported as reference in Fig. 5.23

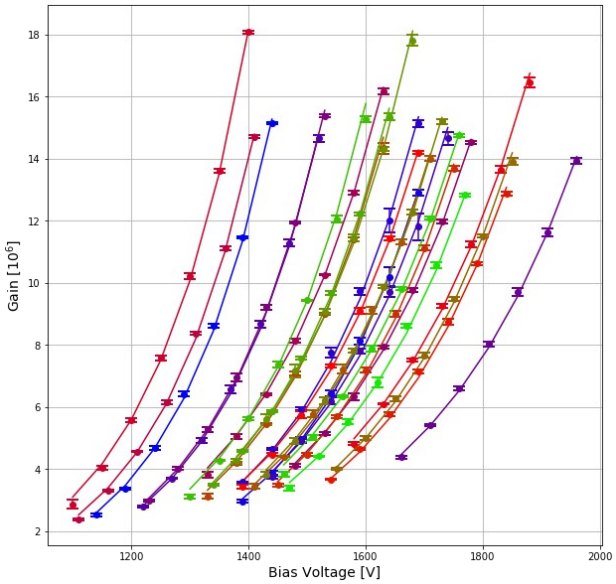

Figure 5.20: Plot of the Gain-HV characteristics of 24 PMTs of the first bunch, shown as a reference

5.6.3 TT/TTS measurements

Hits' timing information could be useful to discriminate between neutron capture signal and background in Neutron Veto. Thus, the relative timing difference among the PMTs needs to be taken into account [254] [260]. The availability of fast digitizers, as well as of a laser, allowed us to perform these kinds of measurement; in particular, we focused on the relative difference in Transit Time, its dependency on the HV and the Transit Time Spread of the 125 PMTs. First of all, before making any kind of timing measurements it was necessary to correct effects like the trigger jitter between the digitizers. In fact, the trigger signal inside the digitizer is generated synchronized to the 125 MHz internal clock. Thus, with respect to the trigger input, the response shows temporal fluctuations of ± 8 ns events by events, the so-called jitter. Since several digitizers were used, whose trigger was transferred from one digitizer to another in daisy chain, a trigger delay between the boards was also induced. Therefore, to obtain precise timing information these effects need to be corrected, according to the equation:

$$t' = t - T_{trigger} + 8ns \cdot \Delta_{chtd} + T_{delay} \tag{5.24}$$

where t' is the time after the correction, t is the time before the correction, $T_{trigger}$ is the threshold crossing time, Δ_{chtd} is the time difference between

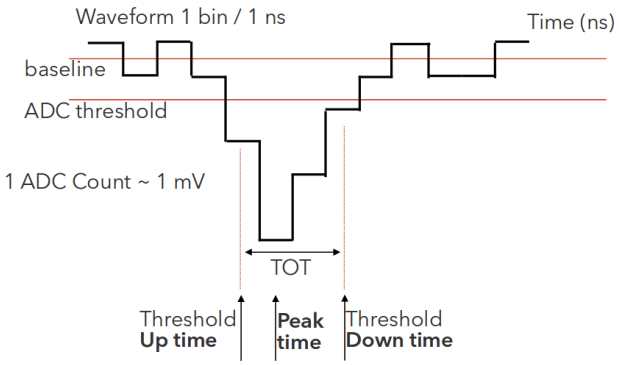

Figure 5.21: Schematic draw of the peak finding algorithm used to define a peak within the dark rate analysis. A peak is defined by giving an ADC threshold (for the analysis this was set equals to 3 ADC counts) and a TOT of 3 samples (3 ns)

two near digiters, and T_{delay} is the time difference between the digiters in question and the so-called "Master" digiter, or a reference digiter.
After making this correction, it was possible to analyze the timing characterization of the PMTs. It was therefore determined the the SPE pulse timing distributions and they were fitted by an asymmetric gaussian:

$$y = \frac{p_0}{\sqrt{2xp_2^2}} exp(-\frac{x - p_1^2}{2p_2^2}) \tag{5.25}$$

for $x \geq p_1$

$$y = \frac{p_0}{\sqrt{2xp_3^2}} exp(-\frac{x - p_1^2}{2p_3^2}) \tag{5.26}$$

for $x < p_1$

In Fig. 5.24 is illustrated an example of this distribution with the double gaussian fit curve.
It was also measured the so-called Transit Time Spread (TTS), that is linked to the FWHM of this distribution:

$$FWHM = \sqrt{2ln2} \cdot (p_2 - p_3) \tag{5.27}$$

The results of the analysis for TT and TTS for 8 PMTs taken as reference are illustrated in Fig. 5.25 and in Fig. 5.25. You can see that if the PMTs are set at the same HV (black line), the TT becomes the same within 1 ns,

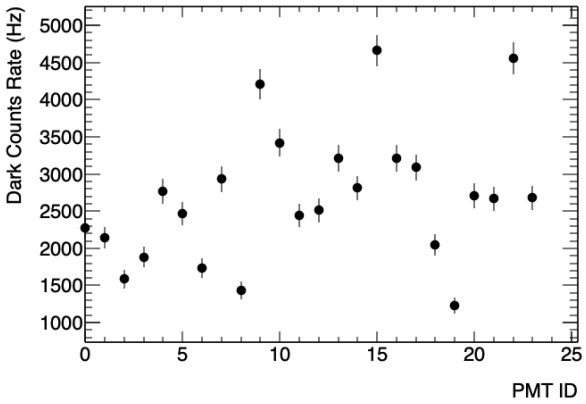

Figure 5.22: Dark counts rate for 25 PMTs of bunch 1, with ADC threshold = 3 counts and TOT = 3 ns

while if the PMTs are set at the same gain (yellow line), the difference in TT among the PMTs becomes ≈ 5 ns. On the other hand, you can also see that the mean TTS is ≈ 3.7 ns

5.6.4 Afterpulse measurements

As mentioned in previous Section, the so-called "afterpulses" are further pulses that can occur in addition to the Main Pulse, which identifies an event. Afterpulses are principally due to the impact of the photoelectrons produced by the Main Pulse with the molecules of the residual gas present in the photomultiplier (see also Subection 5.4.2). These pulses, although they are signals, do not identify any event but are linked to the previous event, that is the one that produced the Main Pulse. Therefore it is necessary to estimate their amount in relation to the Main Pulses, as well as their characteristics, so that they can be identified and treated as a background.
There are some runs specially dedicated to the study of this phenomenon. These runs, called "Afterpulse runs", are caracterized by an acquisition window of 10 μs; the Main Pulse occurs always within the first μs while in the following 9 μs other pulse, the "afterpulses", can occur, as illustrated in Fig. 5.27, relative to the first 1000 events of a PMT taken as reference.
For each run and for each PMT 100k "events" were produced and the pulses that occur in these "events" were statistically analyzed. The pulses produced are "negative" pulses and start from a non-zero adc signal value, called "baseline", which is different for each "event". In order to define the signal as positive and to have a physical comparison "at par" between all the pulses, the "baseline" was calculated for each event and the "amplitude" (positive)

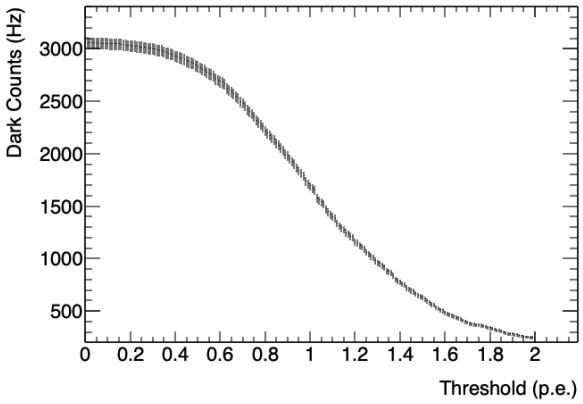

Figure 5.23: Dark counts as function of DAQ threshold for the PMTs of Bunch 1

was defined for each pulse as the difference between the baseline and the minimum value of the adc signal reached. Two "thresholds" were then defined, the "signal threshold" or the minimum difference between baseline and adc signal that the pulse must have in all its duration to be considered in the counting of pulses, and the "amplitude threshold", or the minimum size that the pulse must have to be considered in the count. The first was set at 3 mV while the second was made to vary. The representation of a pulse associated with the various quantities just mentioned is shown in Fig. 5.28. It is very important point out that when the amplitude threshold is too low within the first μs there are many pulses and not a single pulse as one would expect, this means that in addition to the "real" Main Pulse there are other pulses which constitute the "noise". If we consider the scatter plot "duration VS amplitude" Main Pulses and noise are separated quite well and therefore we thought of isolating the first by imposing the condition:

$$\Delta t > a \cdot \Delta V + b \tag{5.28}$$

where Δt is the "duration" (in seconds) of the pulse considered, ΔV is its amplitude (in mV), a and b are variables chosen appropriately for each PMT and for each run so as to obtain the "best separation" between Main Pulses and noise; in practice it is necessary that they in the scatter plot must stand above this "separation line"; then imposing this same condition also for the signals after 1 μs, the pulses were counted in the two cases and therefore, from their ratio the percentage of afterpulse with respect to the Main Pulses was obtained. Fig. 5.29 shows an example of this for a single PMT. In the tables from Tab. 5.1 to Tab. 5.10 it is therefore reported, for each PMT, for

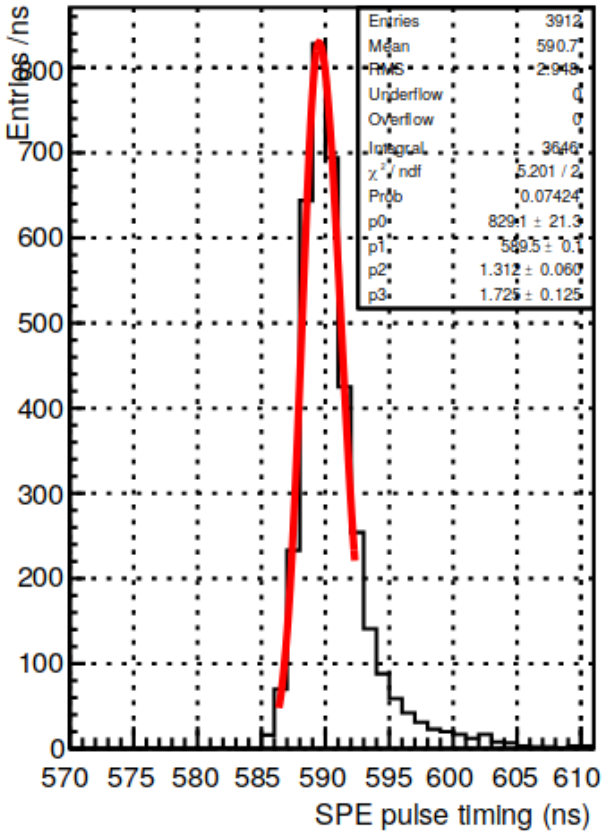

Figure 5.24: Example of SPE time distribution with the double gaussian fit

each run and in the two conditions considered (PMT at NHV and at the same gain): the "goodness" of the separation line, or how well the main pulses and noise are separated in the scatter plot, the number of Main Pulses (i.e. the number of signals within the first μs), the number of afterpulses (i.e. the number of signals in the remaining 9 μs) and the percentage of afterpulses in relation to the Main Pulses. Let us then discuss the results obtained by grouping the PMTs in the 5 bunches and for each bunch, in the two different data taking conditions (PMTs at NHV and PMTs at the same gain). The names of the respective PMTs and the voltages to which they are subjected are also shown in the tables.

BUNCH 1: for this first group of PMTs there is no run with PMTs at the same gain, so it was analyzed only a run with PMTs at NHV. For PMTs of this group the separation between Main Pulses and noise is at least good for all PMTs, and for many of them it is very good or even excellent. The

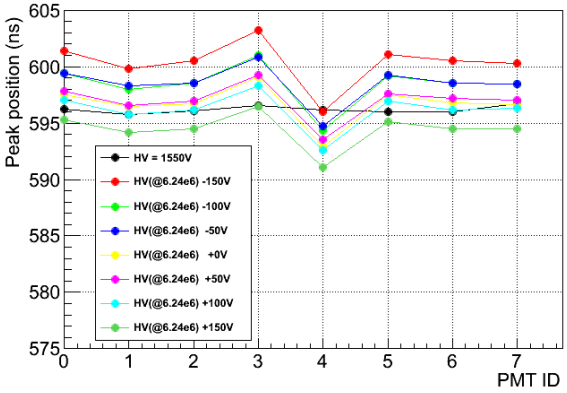

Figure 5.25: Transit time measured for 8 PMTs taken as reference

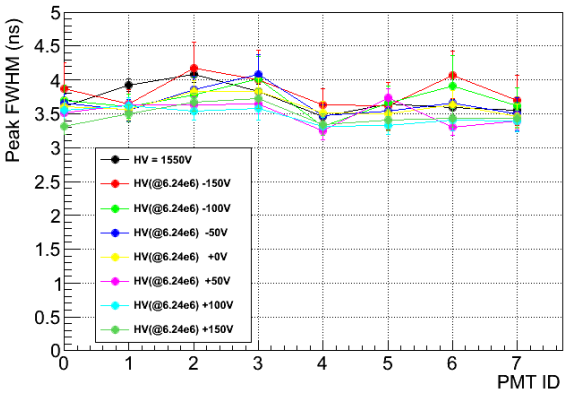

Figure 5.26: Transit time spread measured for 8 PMTs taken as reference

percentage of afterpulses varies from about 1% to about 7%.

BUNCH 2: even for this group of PMTs there are only runs with PMTs at NHV, so it was analyzed only one run of this type. Also for PMTs of this group the separation between Main Pulses and noise is good for all PMTs even if on average it is worse than for PMTs of BUNCH 1. The percentage of afterpulses varies from about 2% to about 8%.

BUNCH 3: for this group of PMTs both run with PMTs at NHV and run with PMTs at the same gain were available. It were then analyzed two runs, one for each type. In the first case, for most PMTs the separation between Main Pulses and noise was good, but in no case excellent, and the percentage of afterpulses varies between about 2% and about 8%. In the

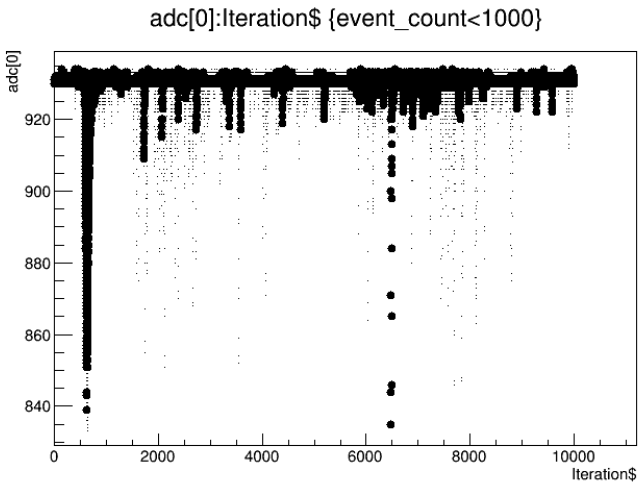

Figure 5.27: Temporal distribution of signal for 1000 "events" overlapping

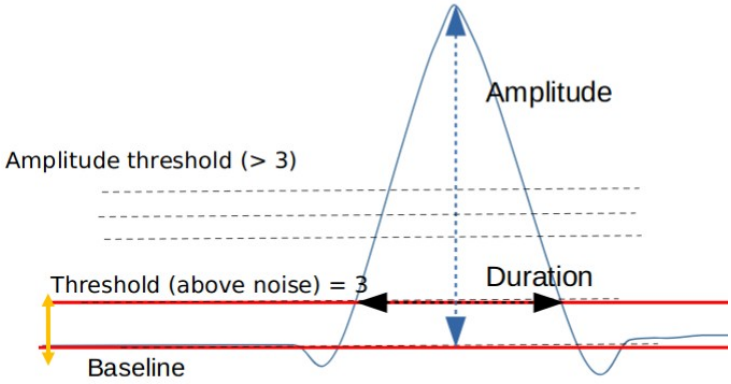

Figure 5.28: A pulse and its caracteristics

second case (PMT at the same gain) since the separation between Main Pulses and noise was always excellent, it was used a different separation method, that considers separatelly ΔV and Δt. Following this method, the Main Pulses were first isolated by imposing that must be satisfied at the same time the condition: $\Delta V > c$ and $\Delta t > d$, where c and d are variable parameters appropriately chosen for each PMT and for each of the two conditions (NHV and HV at same gain), and subsequently the afterpulses are separated from the noise by imposing that Signal Time must be greater than 1 μs (see appropriate tables and Fig. 5.30). The percentage of afterpulse in this case for some PMTs is very high; overall it varies from about 3% to about 21%.

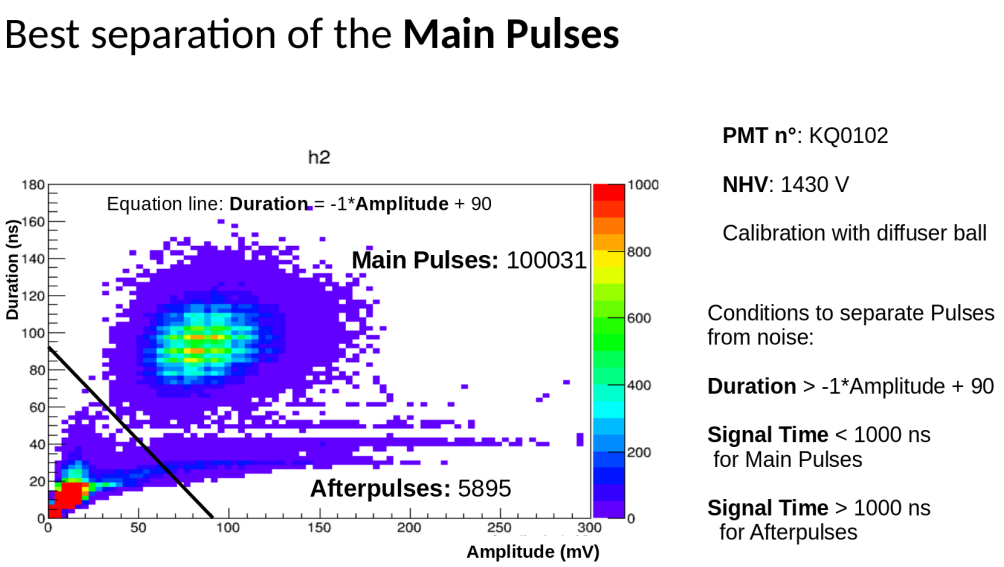

Figure 5.29: Duration as function of Amplitude for a single PMT taken as reference. Separation between Main Pulses, Afterpulses and noise

BUNCH 4: also for this group of PMTs two runs were analyzed, one with PMTs at NHV and another with PMTs at the same gain. In both cases the separation between Main Pulses and noise was not good for most PMTs. On the other hand, the percentage of afterpulses was rather low, varying in both cases from about 1% to about 6%.

BUNCH 5: for this last group there are only runs with PMTs at same gain, so it was analyzed only one run of this type. The separation between Main Pulses and noise was at least good for all PMTs, sometimes even very good or even excellent. The percentage of afterpulse was found to vary from about 1% to about 13%.

What just discussed is summarized in the histograms in Fig. 5.31 and in Fig 5.32, where the distributions of the afterpulse percentage in relation to the Main Pulses are shown separately for each bunch and in the two conditions, PMTs at NHV and PMTs at same gain.
It was also interesting to study the overall distribution of the quantity "Afterpulse percentage in relation to the Main Pulses". The result of this study is shown in Fig. 5.33, where this overall distribution is shown separately for the two conditions, PMTs at NHV and PMTs at same gain. In both cases we can

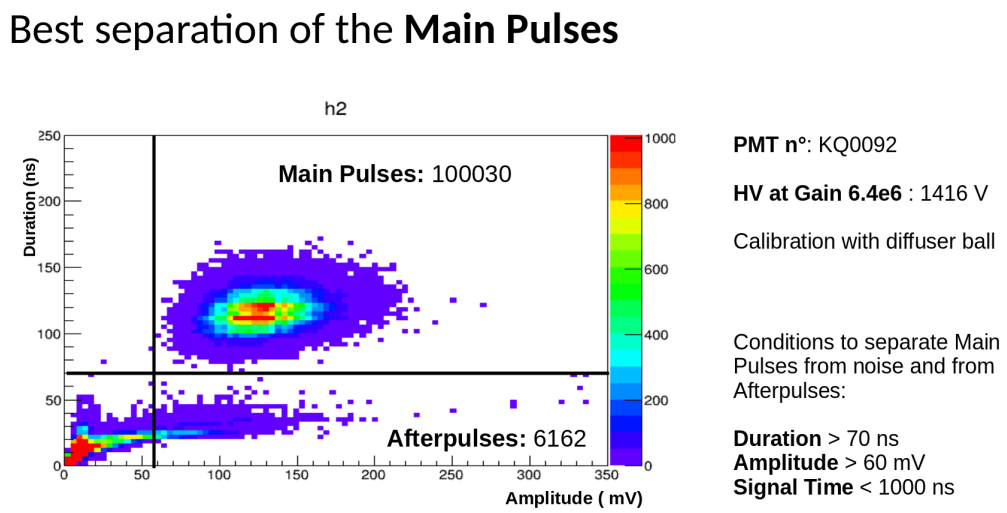

Figure 5.30: Duration as function of Amplitude for a single PMT taken as reference. Separation between Main Pulses, Afterpulses and noise (alternative method)

see a distribution quite similar to a Gaussian, but with a tail on the right. This distribution is centered on a lower value in the case of PMTs at NHV (historgam on the left), and also has a lower dispersion, compared to the case of PMTs at the same gain (histogram on the right).
Finally, the possible existence of a correlation between the quantity "Afterpulse percentage in relation to the Main Pulses" and the quality of the separation between Main Pulses and noise was investigated. The result of this study is shown in Fig. 5.34, in which is illustrated, for all the bunches and separately for the two conditions, PMTs at NHV and PMTs at same gain, the quantity "Afterpulse percentage in relation to the Main Pulses" as function of the quality of the separation, in which the latter was expressed with a numerical value. You can note that in the case of PMTs at Same Gain there is a slight tendency for the percentage of afterpulse to increase as the separation quality improves (graph on the right), while in the case of PMTs at NHV there is no evident correlation (graph on the left).

PMT	NHV	SEP. CONDITION	SEP. QUALITY	% AP/MP
KQ0032	1290	$\Delta t > -1 \cdot \Delta V + 130$	EXCELLENT	0.86
KQ0033	1540	$\Delta t > -1 \cdot \Delta V + 130$	EXCELLENT	3.21
KQ0036	1540	$\Delta t > -0.75 \cdot \Delta V + 150$	EXCELLENT	0.66
KQ0025	1590	$\Delta t > -0.75 \cdot \Delta V + 150$	EXCELLENT	1.64
KQ0029	1370	$\Delta t > -1 \cdot \Delta V + 120$	EXCELLENT	3.06
KQ0026	1810	$\Delta t > -1 \cdot \Delta V + 150$	EXCELLENT	4.48
KQ0031	1380	$\Delta t > -1 \cdot \Delta V + 130$	EXCELLENT	2.48
KQ0021	1630	$\Delta t > -0.75 \cdot \Delta V + 150$	EXCELLENT	6.39
KQ0024	1480	$\Delta t > -1 \cdot \Delta V + 130$	EXCELLENT	3.38
KQ0020	1260	$\Delta t > -1 \cdot \Delta V + 120$	EXCELLENT	2.35
KQ0023 (R)	1250	$\Delta t > -1 \cdot \Delta V + 120$	EXCELLENT	1.64
KQ0035	1730	$\Delta t > -1 \cdot \Delta V + 150$	VERY GOOD	2.81
KQ0011	1540	$\Delta t > -1.3 \cdot \Delta V + 80$	VERY GOOD	6-96
KQ0013	1690	$\Delta t > -1 \cdot \Delta V + 80$	VERY GOOD	7.78
KQ0041	1600	$\Delta t > -1 \cdot \Delta V + 90$	VERY GOOD	5.06
KQ0043 (R)	1480	$\Delta t > -1 \cdot \Delta V + 80$	VERY GOOD	4.31
KQ0042	1560	$\Delta t > -1 \cdot \Delta V + 90$	GOOD	4.22
KQ0040	1700	$\Delta t > -1 \cdot \Delta V + 80$	GOOD	6.46
KQ0038	1580	$\Delta t > -1 \cdot \Delta V + 80$	GOOD	5.28
KQ0039	1530	$\Delta t > -1 \cdot \Delta V + 90$	GOOD	5.35
KQ0046	1490	$\Delta t > -1.3 \cdot \Delta V + 80$	GOOD	4.43
KQ0044	1450	$\Delta t > -1.3 \cdot \Delta V + 80$	VERY GOOD	4.47
KQ0014	1610	$\Delta t > -1 \cdot \Delta V + 90$	GOOD	5.53
KQ0018	1620	$\Delta t > -1.3 \cdot \Delta V + 80$	GOOD	6.63

Table 5.1: Separation conditions, separation quality and afterpulse percentage at NHV for PMTs of Bunch 1

PMT	NHV	SEP. CONDITION	SEP. QUALITY	$\%AP/MP$
KQ0007	1630	$\Delta t > -1 \cdot \Delta V + 80$	VERY GOOD	7.26
KQ0001	1650	$\Delta t > -1 \cdot \Delta V + 80$	VERY GOOD	6.67
KQ0003	1670	$\Delta t > -1 \cdot \Delta V + 80$	GOOD	5.49
KQ0005	1660	$\Delta t > -1 \cdot \Delta V + 80$	FAIRLY GOOD	5.48
KQ0062	1480	$\Delta t > -1 \cdot \Delta V + 80$	VERY GOOD	2.53
KQ0065	1420	$\Delta t > -1 \cdot \Delta V + 90$	VERY GOOD	1.35
KQ0061	1500	$\Delta t > -1 \cdot \Delta V + 90$	VERY GOOD	3.42
KQ0064	1430	$\Delta t > -1 \cdot \Delta V + 100$	VERY GOOD	1.93
KQ0060	1710	$\Delta t > -1 \cdot \Delta V + 100$	VERY GOOD	5.58
KQ0057	1580	$\Delta t > -1 \cdot \Delta V + 80$	VERY GOOD	2.28
KQ0023 (R)	1250	$\Delta t > -1.3 \cdot \Delta V + 80$	VERY GOOD	2.32
KQ0004	1680	$\Delta t > -1.3 \cdot \Delta V + 80$	VERY GOOD	7.87
KQ0053	1680	$\Delta t > -1.3 \cdot \Delta V + 80$	GOOD	6
KQ0055	1520	$\Delta t > -1.3 \cdot \Delta V + 80$	GOOD	3.65
KQ0009	1660	$\Delta t > -1 \cdot \Delta V + 80$	GOOD	6.5
KQ0043 (R)	1480	$\Delta t > -1 \cdot \Delta V + 80$	GOOD	3.48
KQ0058	1530	$\Delta t > -1 \cdot \Delta V + 80$	VERY GOOD	2.38
KQ0056	1390	$\Delta t > -1 \cdot \Delta V + 80$	GOOD	2.12
KQ0052	1530	$\Delta t > -1 \cdot \Delta V + 90$	VERY GOOD	5.52
KQ0047	1660	$\Delta t > -1 \cdot \Delta V + 90$	GOOD	4.08
KQ0049	1500	$\Delta t > -1 \cdot \Delta V + 80$	GOOD	4.63
KQ0048	1590	$\Delta t > -1.3 \cdot \Delta V + 80$	VERY GOOD	3.58
KQ0051	1510	$\Delta t > -1 \cdot \Delta V + 80$	GOOD	7.58
KQ0054	1420	$\Delta t > -1.3 \cdot \Delta V + 80$	GOOD	4.13

Table 5.2: Separation conditions, separation quality and afterpulse percentage at NHV for PMTs of Bunch 2

PMT	NHV	HV Gain $6.24 \cdot 10^6$	$\%AP/MP$ at NHV	$\%AP/MP$ at same Gain
KQ0119	1450	1419	2.66	3.66
KQ0120	1480	1470	3.55	5.81
KQ0122	1500	1475	4.88	9.82
KQ0102	1430	1366	5.89	9.57
KQ0105	1770	1729	3.72	8.11
KQ0115	1470	1426	6	13.38
KQ0116	1530	1463	4.84	10.03
KQ0095	1570	1504	2.91	4.83
KQ0092	1480	1416	4.21	6.16
KQ0067	1400	1383	2.25	2.92
KQ0023 (R)	1250	1215	2.62	2.4
KQ0118	1540	1503	3.91	5.73
KQ0008	1570	1565	7.12	20.61
KQ0094	1570	1525	2.77	5.44
KQ0015	1320	1319	3.21	7.61
KQ0043 (R)	1480	1456	3.82	9.17
KQ0088	1480	1421	2.73	6.48
KQ0066	1320	1271	1.82	3.79
KQ0006	1720	1266	7.74	18.84
KQ0068	1380	1348	2.13	4.35
KQ0069	1570	1518	2.52	5.93
KQ0070	1520	1519	4.11	10.76
KQ0091	1500	1464	5.14	7.6
KQ0090	1480	1441	2.85	5.98

Table 5.3: Afterpulse percentage at NHV and at same gain ($6.24 \cdot 10^6$) for PMTs of Bunch 3

PMT	NHV	HV Gain $6.24 \cdot 10^6$	$\%AP/MP$ at NHV	$\%AP/MP$ at same Gain
KQ0074	1450	1403.5	1	2.52
KQ0087	1480	1435.5	3.25	2.99
KQ0085	1470	1441.5	3.26	3.23
KQ0086	1460	1421.5	2.69	2.33
KQ0073	1320	1273	2.61	2
KQ0101	1620	1531	6.06	4.34
KQ0132	1560	1513.5	2.48	4.09
KQ0001	1410	1358.5	3.06	2.52
KQ0099	1550	1494.5	4.2	3.54
KQ0082	1340	1314.5	1.41	1.41
KQ0023	1250	1216.5	4.33	3.68
KQ0071	1710	1661	6.2	5.72
KQ0123	1560	1523	5.34	4.32
KQ0080	1310	1262.5	1.64	1.14
KQ0129	1470	1442	6.31	4.86
KQ0043 (R)	1480	1435.5	4.65	3.42
KQ0081	1450	1366.5	1.28	0.9
KQ0079	1280	1261.5	1.63	1.55
KQ0078	1410	1348.5	2.64	1.82
KQ0077	1430	1382	1.61	1.26
KQ0128	1553	1553	4.54	3.86
KQ0127	1550	1503.5	5.72	4.66
KQ0072	1550	1509.5	4.09	4.12
KQ0131	1440	1403	3.32	2.86

Table 5.4: Afterpulse percentage at NHV and at same gain ($6.24 \cdot 10^6$) for PMTs of Bunch 4

PMT	HV S.Gain	SEP. CONDITIONS	SEP. QUALITY	$\%AP/MP$
KQ0081	1370	$\Delta t > -1.25 \cdot \Delta V + 100$	VERY GOOD	1.15
KQ0142	1570	$\Delta t > -1 \cdot \Delta V + 100$	EXCELLENT	3.93
KQ0106	1440	$\Delta t > -1 \cdot \Delta V + 100$	EXCELLENT	2.61
KQ0109	1500	$\Delta t > -1 \cdot \Delta V + 100$	EXCELLENT	4.94
KQ0110	1530	$\Delta t > -1 \cdot \Delta V + 100$	EXCELLENT	2.92
KQ0039	1530	$\Delta t > -1.25 \cdot \Delta V + 100$	VERY GOOD	6.01
KQ0021	1630	$\Delta t > -1.25 \cdot \Delta V + 100$	VERY GOOD	8.6
KQ0114	1380	$\Delta t > -1.4 \cdot \Delta V + 70$	VERY GOOD	1.89
KQ0042	1560	$\Delta t > -1 \cdot \Delta V + 80$	VERY GOOD	4.53
KQ0038	1580	$\Delta t > -1 \cdot \Delta V + 100$	GOOD	4.68
KQ0023 (R)	1250	$\Delta t > -1 \cdot \Delta V + 100$	VERY GOOD	3.51
KQ0040	1700	$\Delta t > -1 \cdot \Delta V + 100$	VERY GOOD	8.07
KQ0100	1580	$\Delta t > -1.25 \cdot \Delta V + 100$	GOOD	4.45
KQ0126	1400	$\Delta t > -1 \cdot \Delta V + 80$	FAIRLY GOOD	4.33
KQ0138	1520	$\Delta t > -1 \cdot \Delta V + 80$	GOOD	4.63
KQ0043 (R)	1480	$\Delta t > -1 \cdot \Delta V + 80$	GOOD	5.51
KQ0107	1480	$\Delta t > -1.4 \cdot \Delta V + 100$	GOOD	6.1
KQ0098	1600	$\Delta t > -1 \cdot \Delta V + 80$	GOOD	7.19
KQ0104	1500	$\Delta t > -1.3 \cdot \Delta V + 80$	GOOD	7.47
KQ0103	1520	$\Delta t > -1.3 \cdot \Delta V + 80$	FAIRLY GOOD	13.06
KQ0108	1510	$\Delta t > -1.3 \cdot \Delta V + 80$	FAIRLY GOOD	6.26
KQ0135	1420	$\Delta t > -1.3 \cdot \Delta V + 80$	FAIRLY GOOD	4.54
KQ0136	1620	$\Delta t > -1 \cdot \Delta V + 80$	GOOD	4.63
KQ0139	1510	$\Delta t > -1 \cdot \Delta V + 80$	FAIRLY GOOD	5.58

Table 5.5: Separation conditions, separation quality and afterpulse percentage at same gain ($6.24 \cdot 10^6$) for PMTs of Bunch 5

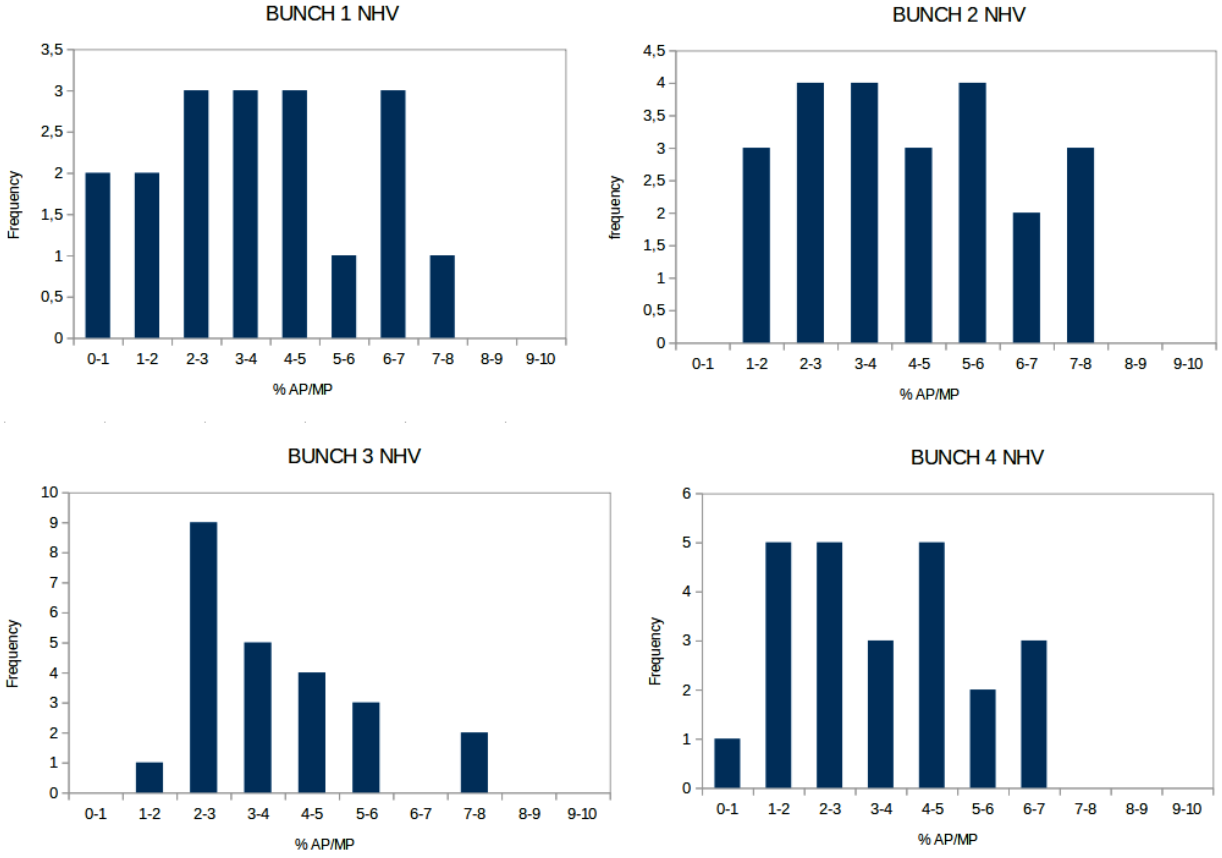

Figure 5.31: Distributions of the afterpulse percentage in relation to the Main Pulses for the PMTs of bunches 1,2,3 and 4, at NHV

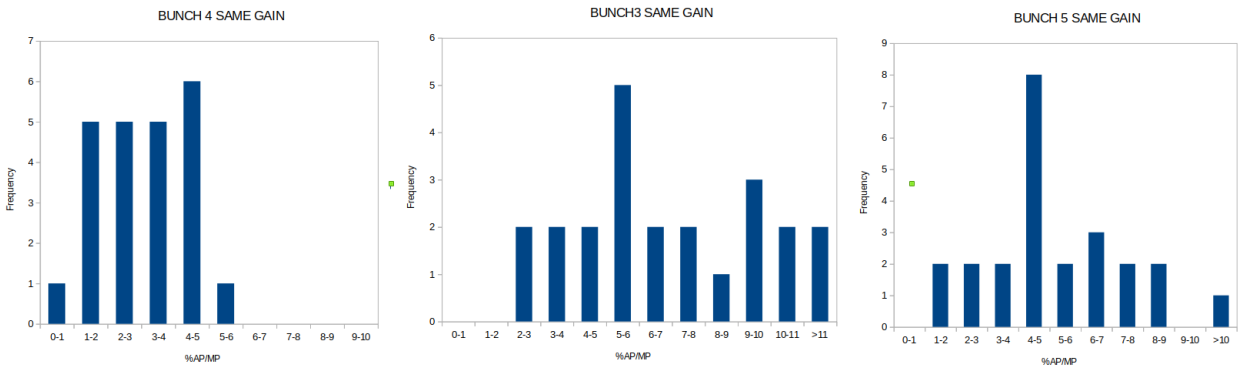

Figure 5.32: Distributions of the afterpulse percentage in relation to the Main Pulses for the PMTs of bunches 3,4 and 5, at Same Gain

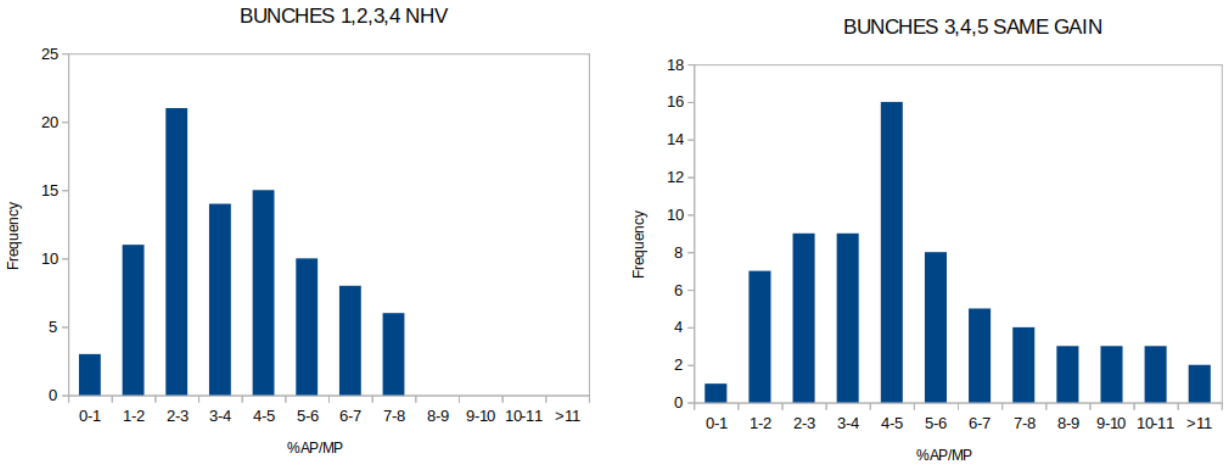

Figure 5.33: Overall distributions of the afterpulse percentage in relation to the Main Pulses for the PMTs of all the bunches analyzed (1,2,3,and 4 at NHV, 3,4 and 5 at Same Gain)

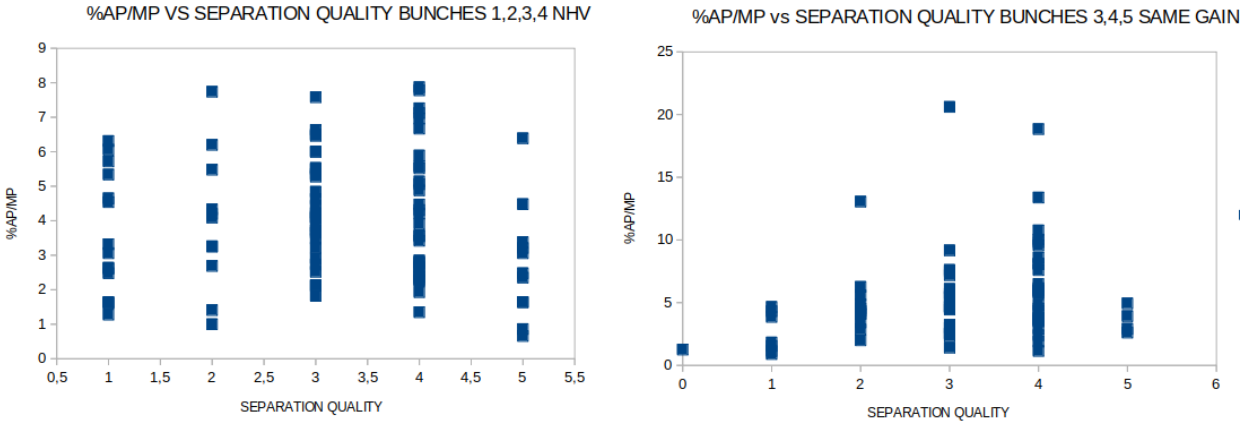

Figure 5.34: Afterpulse percentage in relation to the Main Pulses as function of Separation Quality (0=VERY BAD, 1=BAD, 2=FAILRLY GOOD, 3=GOOD, 4=VERY GOOD, 5=EXCELLENT) for the PMTs of all the bunches analyzed (1,2,3,and 4 at NHV, 3,4 and 5 at Same Gain)

Conclusions

In this thesis was discussed the problem of dark matter existence and its direct search with the XENON experiment at the Gran Sasso National Laboratories (LNGS), in its most recent upgrade, XENONnT. The existence of dark matter was hypothesized for the first time at the first decades of the last century to explain some astrophysical and cosmological phenomena that were observed: the anomalies in the rotation speed of galaxies, the gravitational lensing, the bullet cluster, the anisotropies in the Cosmic Microwave Background (CMB). The nature of dark matter is today still unknown, but all the observations made so far have led us to believe that it is made of particles with a big mass but which interact with ordinary matter only gravitationally and through weak interactions, and for this reason they are very difficult to be detected. These particles were then called WIMP (Weak Interacting Massive Particles). Dark matter search can be divided into three main categories: production at particle accelerators, indirect search and direct search. The latter, as in XENON experiment, is based on the scattering that WIMP do on the target nuclei. Cross sections of these processes are very small, for this reason it is necessary to use detectors of large mass and placed deep underground or underwater. The XENON experiment is located at the Gran Sasso National Laboratories (LNGS) below about 1400 meters of rock and uses Xenon as a detector medium, in a double phase, liquid (LXe) and gaseous (GXe). Xenon, like other noble gases, has numerous advantages for detecting dark matter. The XENON experiment had presented in the years upgrades caracterized by increasing of detector mass, by reduction of the background thanks to new techniques gradually developed and consequently progressive decrease of the minimum detectable limit for the cross section of WIMP-nuclei scattering. The penultimate upgrade, XENON1T, was operational from 2016 to 2018 and, with a target mass of 3.2 tons, set the limit for the spin-independent WIMP-nucleon elastic scattering cross section to $4.11 \cdot 10^{-47} cm^2$ at 90% of CL. The present upgrade, XENONnT, has almost finished its construction phase and it will be operational from the end of 2020. The mass of the detector has been increased to 8 tons, of which 6 tons represent the active

part, but the most important innovation was the construction of the Neutron Veto (absent in XENON1T), a new detector able to identify radiogenic neutrons originating from the detector materials and thus further reduce the background level. Among the various types of neutrons that can give a signal, the most difficult to identify are the so-called "sneaky neutrons", which are those that are generated in the TPC and scatter just once in the cryostat, simulating a signal identical to that produced by WIMPs. The Neutron Veto was specifically designed to identify this type of neutron; it uses water doped with Gadolinium (Gd) as a detector medium; Gadolinium is the material with the highest "neutron capture" cross section and, when a neutron is absorbed by Gd about 8 MeV of energy are released in a bunch of photons. Water also plays an important role in the neutron capture, first of all because it allows them to be thermalized in such a way that they can be captured by Gadolinium, moreover a small part of them is also captured by the hydrogen protons of the water. The Neutron Veto is equipped with 120 photomultipliers (PMTs), which detect and amplify the light signal produced by the neutron capture. To distinguish the "sneaky neutrons" from the other types of neutrons, i.e. the neutrons generated within Gd+water and the neutrons generated within the PMT materials, two methods, both based on Monte Carlo simulations, were also used, and thanks to this technique, a detection efficiency for "sneaky neutrons" of about 90% is obtained and therefore a significant reduction of this type of background was estimed to be obtained. Therefore, when the Neutron Veto will be put in operation in the new XENONnT detector, will be able to reach a limit for cross section of WIMP-nuclei interaction of an order of magnitude lower compared to XENON1T. This improvement in sensitivity will allow, moreover, to further investigate about the nature of some signals that have been detected by XENON1T and possibly identifiable as Axions.
Before carrying out the implementation of XENONnT detector and the Neutron Veto, it was necessary to carry out some tests to verify the correct functioning of Neutron Veto's PMTs. These tests essentially concerned in the analysis of four characteristic parameters of PMTs: the so-called "Gain", or the total number of electrons produced per incident photon, the stability of the latter over time was also evaluated; the so-called "Dark rate", that is the rate of signals generated by PMTs in the absence of light; the so-called "Transit Times", i.e. the differences between the transit times of photons in the various PMTs; finally, the phenomenon of so-called afterpulses, which are signals that occur in PMTs after the Main Pulse and are linked to the previous pulse; studying their amount in relation to the amount of Main Pulses and their characteristics was important for evaluating their background. The analysis of these quantities was carried out by various

research groups, including that of Naples, of which I am a member. So, I have contributed to this analysis. Once this analysis was completed, the entire structure was then assembled at the Gran Sasso National Laboratories (LNGS), and the full construction has been underway in recent months and most completed at present. The start of the XENONnT data taking is expected by the end of 2020.

Bibliography

[1] "The Dark Universe" - Catherine Heymans (2017)

[2] Ashley Ross and collaborators (???)

[3] Institute of Computational Cosmology, Duhram (???)

[4] https://www.asimmetrie.it/index.php/il-lato-oscuro-dell-universo

[5] https://www.euclid-ec.org/

[6] De Zotti et al. "Extragalactic Astrophysics With Next-Generation CMB Experiments" (2019) https://www.frontiersin.org/articles/10.3389/fspas.2019.00053/full

[7] Phd Physics thesis : "The XENON project: backgrounds and new results" - Federica Agostini (2017)

[8] F. Zwicky, Die Rotverschiebung von extragalaktischen Nebeln, (1933), Helvetica Physica Acta 6, 110

[9] K. G. Begeman, A. H. Broeils and R. H. Sanders, "Extended rotation curves of spiral galaxies - Dark haloes and modified dynamics", (1991), MNRAS (ISSN 0035-8711) 249, 523

[10] J. F. Navarro et al., A "Universal Density Profile from Hierarchical Clustering", 1997, Ap. J. 490, 493

[11] J. F. Navarro et al., "A Universal Density Profile from Hierarchical Clustering", (1997), Ap. J. 490, 493

[12] D. Walsh, R. F. Carswell, and R. J. Weymann, 0957 + 561 A, B - "Twin quasistellar objects or gravitational lens", (1979), Nature 279, 381

[13] J.U+2010]P. Kneib, R. S. Ellis and I. Smail, "Hubble Space Telescope Observations of the Lensing Cluster Abell" 2218, Astrophys. J. 471, 2

[14] D. Clowe, A. and M. Markevitch, Weak lensing mass reconstruction of the interacting cluster 1E0657-558: Direct evidence for the existence of dark matter, (2004), Astrophys. J. 604, 596

[15] P. A. R. Ade et al., Planck 2013 results. XV. CMB power spectra and likelihood, 2013, A.A 571, A15

[16] Stephen P. Martin, A Supersymmetry primer, (1998), Adv. Ser. Di- rect. High Energy Phys. 18, 1

[17] https://it.wikipedia.org/wiki/Xeno

[18] https://www.periodni.com/it/xe.html

[19] J. B. Albert et al., Improved measurement of the 2 $\nu\beta\beta$ half-life of with the EXO-200 detector, Phys. Rev. C89(1), 015502 (2014)

[20] P.Dehmer et al. "Photoelectron spectra of Xe_2* obtained by resonantly enhanced multiphoton ionization" (1986)

[21] V. Solovov et al., Measurement of the Refractive Index and Attenuation Length of Liquid Xenon for its Scintillation Light, Nucl. Instrum. Meth. Phys. Res., Sect. A 516, 462, (2004)

[22] https://xe1t-wiki.lngs.infn.it/doku.php?id=xenon:xenon1t:screening

[23] E. Aprile et al., Study of the electromagnetic background in the XE-NON100 experiment, Phys. Rev. D 83, 082001, (2011)

[24] "Dark matter direct-detection experiments" - Teresa Marrodán Undagoitia and Ludwig Rauch (2017)

[25] "Dark matter indirect detection" - Stefano Profumo (2020)

[26] Jonathan L. Ouellet et al. "First Results from ABRACADABRA-10 cm: A Search for Sub-?eV Axion Dark Matter" (2019)

[27] L. Zhong et al., "Results from phase 1 of the HAYSTAC microwave cavity axion experiment" (2018)

[28] A. De Angelis et al. "The e-ASTROGAM mission (exploring the extreme Universe with gamma rays in the MeV-GeV range)" (2017)

[29] A.A. Moisev et al. "Compton-Pair Production Space Telescope (ComPair) for MeV Gamma-ray Astronomy" (2015)

[30] A. Coogan et al. "Hazma: A Python Toolkit for Studying Indirect Detection of Sub-GeV Dark Matter" (2019)

[31] https://www.auger.org/index.php/observatory/heat

[32] Marcelli, N. et al. "Time Dependence Of The Helium Flux Measured By Pamela". EPJ Web Conf. 209 (2019): 01004

[33] Profumo et al. "Has AMS-02 Observed Two-Component Dark Matter ?" (2019)

[34] https://www.nasa.gov/hitomi

[35] https://fermi.gsfc.nasa.gov/science/

[36] https://www.hawc-observatory.org/

[37] https://www.ligo.org/

[38] http://www.virgo-gw.eu/

[39] M. Milgrom, "A Modification of the Newtonian dynamics as a possible alternative to the hidden mass hypothesis," Astrophys. J. 270 (1983) 365.

[40] J. D. Bekenstein, "Relativistic gravitation theory for the MOND paradigm," Phys. Rev. D70 (2004) 083509, arXiv:astro-ph/0403694.

[41] J. Felten, "Milgrom?s revision of Newton?s laws - Dynamical and cosmological consequences," ApJ 286 (Nov., 1984) 3

[42] M. D. Seifert, "Stability of spherically symmetric solutions in modified theories of gravity," Phys. Rev. D76 (2007) 064002, arXiv:gr-qc/0703060.

[43] N. E. Mavromatos, M. Sakellariadou, and M. F. Yusaf, "Can the relativistic field theory version of modified Newtonian dynamics avoid dark matter on galactic scales?," Phys. Rev. D 79 no. 8, (Apr., 2009) 081301, arXiv:0901.3932.

[44] B. Paczynski, "Gravitational microlensing by the galactic halo," Astrophys. J. 304 (1986) 1.

[45] MACHO Collaboration, C. Alcock et al., "The MACHO project: Microlensing results from 5.7 years of LMC observations," Astrophys. J. 542 (2000) 281, arXiv:astro-ph/0001272.

[46] F. Iocco, G. Mangano, G. Miele, O. Pisanti, and P.D. Serpico, "Primordial Nucleosynthesis: from precision cosmology to fundamental physics," Phys. Rept. 472 (2009) 1, arXiv:0809.0631.

[47] B. Carr, F. Kuhnel, and M. Sandstad, "Primordial Black Holes as Dark Matter," Phys. Rev. D94 no. 8, (2016) 083504, arXiv:1607.06077.

[48] B. J. Carr, K. Kohri, Y. Sendouda, and J. Yokoyama, "New cosmological constraints on primordial black holes," Phys. Rev. D81 (2010) 104019, arXiv:0912.5297.

[49] S. D. White, C. Frenk, and M. Davis, "Clustering in a Neutrino Dominated Universe," Astrophys. J. 274 (1983) L1

[50] S. Tremaine and J. E. Gunn, "Dynamical role of light neutral leptons in cosmology," Phys. Rev. Lett. 42 (1979) 407.

[51] K. N. Abazajian et al., "Light Sterile Neutrinos: A White Paper," arXiv:1204.5379.

[52] A. Kusenko, "Sterile neutrinos: The Dark side of the light fermions," Phys. Rept. 481 (2009) 1, arXiv:0906.2968.

[53] A. Boyarsky, O. Ruchayskiy, and M. Shaposhnikov, "The Role of sterile neutrinos in cosmology and astrophysics," Ann. Rev. Nucl. Part. Sci. 59 (2009) 191, arXiv:0901.0011.

[54] K. Abazajian, G. M. Fuller, and W. H. Tucker, "Direct detection of warm dark matter in the X-ray," Astrophys. J. 562 (2001) 593, arXiv:astro-ph/0106002.

[55] K. Abazajian, G. M. Fuller, and W. H. Tucker, "Direct detection of warm dark matter in the X-ray," Astrophys. J. 562 (2001) 593, arXiv:astro-ph/0106002

[56] G. Gelmini and P. Gondolo, "DM Production Mechanisms," arXiv:1009.3690

[57] M. Duerr, F. Kahlhoefer, K. Schmidt-Hoberg, T. Schwetz, and S. Vogl, "How to save the WIMP: global analysis of a dark matter model with two s-channel mediators," JHEP 09 (2016) 042, arXiv:1606.07609.

[58] G. Arcadi, M. Dutra, P. Ghosh, M. Lindner, Y. Mambrini, M. Pierre, S. Profumo, and F. S. Queiroz, "The Waning of the WIMP? A Review of Models, Searches, and Constraints," arXiv:1703.07364.

[59] G. Jungman, M. Kamionkowski, and K. Griest, "Supersymmetric dark matter," Phys. Rept. 267 (1996) 195, arXiv:hep-ph/9506380.

[60] T. Kaluza, "Zum Unitätsproblem in der Physik," Sitzungsber. Preuss. Akad. Wiss. Berlin. (Math. Phys.) (1921) 966.

[61] O. Klein, "Quantum Theory and Five-Dimensional Theory of Relativity," Z. Phys. 37 (1926) 895.

[62] V. Kuzmin and I. Tkachev, "Ultrahigh-energy cosmic rays, superheavy long living particles, and matter creation after inflation," JETP Lett. 68 (1998) 271, arXiv:hep-ph/9802304.

[63] K. Greisen, "End to the cosmic ray spectrum?," Phys. Rev. Lett. 16 (1966) 748.

[64] G. Zatsepin and V. Kuzmin, "Upper limit of the spectrum of cosmic rays," JETP Lett. 4 (1966) 78.

[65] D. J. Chung, E. W. Kolb, and A. Riotto, "Superheavy dark matter," Phys. Rev. D59 (1999) 023501, arXiv:hep-ph/9802238.

[66] C. Baker et al., "An Improved experimental limit on the electric dipole moment of the neutron," Phys. Rev. Lett. 97 (2006) 131801, arXiv:hep-ex/0602020.

[67] G. G. Raffelt, "Astrophysical axion bounds," Lect. Notes Phys. 741 (2008) 51, arXiv:hep-ph/0611350.

[68] R. Peccei and H. R. Quinn, "CP Conservation in the Presence of Instantons," Phys. Rev. Lett. 38 (1977) 1440.

[69] S. Weinberg, "A New Light Boson?," Phys. Rev. Lett. 40 (1978) 223.

[70] J. E. Kim, "Weak Interaction Singlet and Strong CP Invariance," Phys. Rev. Lett. 43 (1979) 103.

[71] M. A. Shifman, A. Vainshtein, and V. I. Zakharov, "Can Confinement Ensure Natural CP Invariance of Strong Interactions?," Nucl. Phys. B166 (1980) 493.

[72] A. Zhitnitsky, "On Possible Suppression of the Axion Hadron Interactions. (In Russian)," Sov. J. Nucl. Phys. 31 (1980) 260.

[73] M. Dine, W. Fischler, and M. Srednicki, ?A Simple Solution to the Strong CP Problem with a Harmless Axion,? Phys. Lett. B104 (1981) 199.

[74] P. Sikivie, "Experimental Tests of the Invisible Axion," Phys. Rev. Lett. 51 (1983) 1415.

[75] L. Abbott and P. Sikivie, "A Cosmological Bound on the Invisible Axion," Phys. Lett. B120 (1983) 133.

[76] L. Visinelli and P. Gondolo, "Dark Matter Axions Revisited," Phys. Rev. D80 (2009) 035024, arXiv:0903.4377.

[77] G. Bertone, ed., Particle dark matter. Cambridge University Press, 2010.

[78] CMS Collaboration, S. Chatrchyan et al., "The CMS experiment at the CERN LHC," JINST 3 (2008) S08004.

[79] ATLAS Collaboration, G. Aad et al., "The ATLAS Experiment at the CERN Large Hadron Collider," JINST 3 (2008) S08003.

[80] CMS Collaboration, S. Chatrchyan et al., "Observation of a new boson at a mass of 125 GeV with the CMS experiment at the LHC" Phys. Lett. B716 (2012) 30, arXiv:1207.7235.

[81] ATLAS Collaboration, G. Aad et al., "Observation of a new particle in the search for the Standard Model Higgs boson with the ATLAS detector at the LHC," Phys. Lett. B716 (2012) 1, arXiv:1207.7214.

[82] CMS Collaboration, A. M. Sirunyan et al., "Search for dark matter produced with an energetic jet or a hadronically decaying W or Z boson at sqrt(s) = 13 TeV" arXiv:1703.01651 [hep-ex] (???)

[83] ATLAS Collaboration, M. Aaboud et al., "Search for new phenomena in final states with an energetic jet and large missing transverse momentum in pp collisions at sqrt(s) = 13 TeV using the ATLAS detector" Phys. Rev. D94 no. 3, (2016) 032005, arXiv:1604.07773. (???)

[84] CMS Collaboration, A. M. Sirunyan et al., "Search for dijet resonances in proton-proton collisions at sqrt(s) = 13 TeV and constraints on dark matter and other models" Phys. Lett. B. , arXiv:1611.03568. (2016)

[85] L. E. Strigari, "Galactic Searches for Dark Matter, "Phys. Rept. 531" (2013) 1, arXiv:1211.7090.

[86] A. Ibarra, D. Tran, and C. Weniger, "Indirect Searches for Decaying Dark Matter," Int. J. Mod. Phys. A28 (2013) 1330040, arXiv:1307.6434.

[87] MAGIC Collaboration, J. Aleksi et al., "Optimized dark matter searches in deep observations of Segue 1 with MAGIC," JCAP 1402 (2014) 008, arXiv:1312.1535.

[88] Fermi-LAT, MAGIC Collaboration, M. L. Ahnen et al., "Limits to dark matter annihilation cross-section from a combined analysis of MAGIC and Fermi-LAT observations of dwarf satellite galaxies," JCAP 1602 no. 02, (2016) 039, arXiv:1601.06590.

[89] H.E.S.S. Collaboration, A. Abramowski et al., "Search for dark matter annihilation signatures in H.E.S.S. observations of Dwarf Spheroidal Galaxies," Phys. Rev. D90 (2014) 112012,n arXiv:1410.2589

[90] H.E.S.S. Collaboration, H. Abdallah et al., "Search for dark matter annihilations towards the inner Galactic halo from 10 years of observations with H.E.S.S," Phys. Rev. Lett. 117 no. 11, (2016) 111301, arXiv:1607.08142

[91] VERITAS Collaboration, T. Arlen et al., "Constraints on Cosmic Rays, Magnetic Fields, and Dark Matter from Gamma-Ray Observations of the Coma Cluster of Galaxies with VERITAS and Fermi," Astrophys. J. 757 (2012) 123, arXiv:1208.0676.

[92] VERITAS Collaboration, S. Archambault et al., ?Dark Matter Constraints from a Joint Analysis of Dwarf Spheroidal Galaxy Observations with VERITAS,? arXiv:1703.04937.

[93] J. Conrad, J. Cohen-Tanugi, and L. E. Strigari, ?WIMP searches with gamma rays in the Fermi era: challenges, methods and results,? JETP 148 (2015) 12, arXiv:1503.06348.

[94] Fermi-LAT Collaboration, M. Ackermann et al., "The Spectrum and Morphology of the Fermi Bubbles," Astrophys. J. 793 (2014) 64, arXiv:1407.7905.

[95] D. Hooper and L. Goodenough, ?Dark Matter Annihilation in The Galactic Center As Seen by the Fermi Gamma Ray Space Telescope,? Phys. Lett. B697 (2011) 412, arXiv:1010.2752.

[96] Fermi-LAT Collaboration, M. Ackermann et al., "Limits on Dark Matter Annihilation Signals from the Fermi LAT 4-year Measurement of the

Isotropic Gamma-Ray Background," JCAP 1509 no. 09, (2015) 008, arXiv:1501.05464

[97] Fermi-LAT Collaboration, M. Ackermann et al., "Updated search for spectral lines from Galactic dark matter interactions with pass 8 data from the Fermi Large Area Telescope," Phys. Rev. D91 no. 12, (2015) 122002, arXiv:1506.00013.

[98] Fermi-LAT Collaboration, M. Ackermann et al., "Searching for Dark Matter Annihilation from Milky Way Dwarf Spheroidal Galaxies with Six Years of Fermi Large Area Telescope Data," Phys. Rev. Lett. 115 no. 23, (2015) 231301, arXiv:1503.02641

[99] DES, Fermi-LAT Collaboration, A. Albert et al., ?Searching for Dark Matter Annihilation in Recently Discovered Milky Way Satellites with Fermi-LAT,? Astrophys. J. 834 no. 2. 110, arXiv:1611.03184 (2017)

[100] DES, Fermi-LAT Collaboration, A. Albert et al., "Searching for Dark Matter Annihilation in Recently Discovered Milky Way Satellites with Fermi-LAT" Astrophys. J. 834 no. 2, (2017) 110, arXiv:1611.03184

[101] E. Bulbul et al., "Detection of An Unidentified Emission Line in the Stacked X-ray spectrum of Galaxy Clusters" Astrophys. J. 789 (2014) 13, arXiv:1402.2301.

[102] A. Boyarsky, O. Ruchayskiy, D. Iakubovskyi, and J. Franse, ?Unidentified Line in X-Ray Spectra of the Andromeda Galaxy and Perseus Galaxy Cluster,? Phys. Rev. Lett. 113 (2014) 251301, arXiv:1402.4119

[103] K. N. Abazajian, "Resonantly Produced 7 keV Sterile Neutrino Dark Matter Models and the Properties of Milky Way Satellites," Phys. Rev. Lett. 112 no. 16, (2014) 161303, arXiv:1403.0954

[104] H. Ishida, K. S. Jeong, and F. Takahashi, "7 keV sterile neutrino dark matter from split flavor mechanism," Phys. Lett. B732 (2014) 196, arXiv:1402.5837

[105] T. Higaki, K. S. Jeong, and F. Takahashi, "The 7 keV axion dark matter and the X-ray line signal," Phys. Lett. B733 (2014) 25, arXiv:1402.6965.

[106] J. Jaeckel, J. Redondo, and A. Ringwald, "3.55 keV hint for decaying axionlike particle dark matter," Phys. Rev. D89 (2014) 103511, arXiv:1402.7335.

[107] T. E. Jeltema and S. Profumo, ?Discovery of a 3.5 keV line in the Galactic Center and a Critical Look at the Origin of the Line Across Astronomical Targets,? Mon. Not. Roy. Astron. Soc. 450 (2015) 2143, arXiv:1408.1699.

[108] E. Carlson, T. Jeltema, and S. Profumo, "Where do the 3.5 keV photons come from" A morphological study of the Galactic Center and of Perseus,? JCAP 1502 no. 02, (2015) 009, arXiv:1411.1758.

[109] E. Bulbul et al., "Comment on Dark matter searches going bananas: the contribution of Potassium (and Chlorine) to the 3.5 keV line", arXiv:1409.4143.

[110] C. Shah, S. Dobrodey, S. Bernitt, R. Steinbruegge, J. R. C. López-Urrutia, L. Gu, and J. Kaastra, "Laboratory measurements compellingly support charge-exchange mechanism for the dark matter ?3.5 keV X-ray line," Astrophys. J. 833 no. 1, (2016) 52, arXiv:1608.04751

[111] IceCube Collaboration, M. G. Aartsen et al., "Search for annihilating dark matter in the Sun with 3 years of IceCube data," Eur. Phys. J. C77 no. 3, (2017) 146, arXiv:1612.05949.

[112] ANTARES Collaboration, S. Adrian-Martinez et al., "Limits on Dark Matter Annihilation in the Sun using the ANTARES Neutrino Telescope," Phys. Lett. B759 (2016) 69, arXiv:1603.02228.

[113] Super-Kamiokande Collaboration, K. Choi et al., ?Search for neutrinos from annihilation of captured low-mass dark matter particles in the Sun by Super-Kamiokande,? Phys. Rev. Lett. 114 no. 14, (2015) 141301, arXiv:1503.04858.

[114] PAMELA Collaboration, O. Adriani et al., "An anomalous positron abundance in cosmic rays with energies 1.5-100 GeV," Nature 458 (2009) 607, arXiv:0810.4995.

[115] AMS Collaboration, M. Aguilar et al., ?First Result from the Alpha Magnetic Spectrometer on the International Space Station: Precision Measurement of the Positron Fraction in Primary Cosmic Rays of 0.5350 GeV,? Phys. Rev. Lett. 110 (2013) 141102.

[116] K. Blum, B. Katz, and E. Waxman, ?AMS-02 Results Support the Secondary Origin of Cosmic Ray Positrons,? Phys. Rev. Lett. 111 no. 21, (2013) 211101, arXiv:1305.1324.

[117] J. Lewin and P. Smith, "Review of mathematics, numerical factors, and corrections for dark matter experiments based on elastic nuclear recoil," Astropart. Phys. 6 (1996) 87.

[118] M. W. Goodman and E. Witten, "Detectability of Certain Dark Matter Candidates," Phys. Rev. D31 (1985) 3059.

[119] A. Drukier, K. Freese, and D. Spergel, ?Detecting Cold Dark Matter Candidates," Phys. Rev. D33 (1986) 3495.

[120] K. Freese, M. Lisanti, and C. Savage, "Colloquium: Annual modulation of dark matter," Rev. Mod. Phys. 85 (2013) 1561, arXiv:1209.3339.

[121] D. N. Spergel, "The Motion of the Earth and the Detection of Weakly interacting massive particles," Phys. Rev. D37 (1988) 1353.

[122] D. P. Snowden-Ifft, C. J. Martoff, and J. M. Burwell, "Low pressure negative ion drift chamber for dark matter search," Phys. Rev. D61 (2000) 101301, arXiv:astro-ph/9904064.

[123] C. E. Yaguna, ?Isospin-violating dark matter in the light of recent data,? arXiv:1610.08683.

[124] R. H. Helm, "Inelastic and Elastic Scattering of 187-MeV Electrons from Selected Even-Even Nuclei," Phys. Rev. 104 (1956) 1466.

[125] L. Vietze, P. Klos, J. Menndez, W. Haxton, and A. Schwenk, "Nuclear structure aspects of spin-independent WIMP scattering off xenon," Phys. Rev. D91 no. 4, (2015) 043520, arXiv:1412.6091.

[126] A. M. Green, "Astrophysical uncertainties on direct detection experiments," Mod. Phys. Lett. A27 (2012) 1230004, arXiv:1112.0524.

[127] J. Read, "The Local Dark Matter Density," J. Phys. G41 (2014) 063101, arXiv:1404.1938.

[128] F. J. Kerr and D. Lynden-Bell, "Review of galactic constants," Mon. Not. Roy. Astron. Soc. 221 (1986) 1023.

[129] M. C. Smith, G. Ruchti, A. Helmi, R. Wyse, J. Fulbright, et al., "The RAVE Survey: Constraining the Local Galactic Escape Speed," Mon. Not. Roy. Astron. Soc. 379 (2007) 755, arXiv:astro-ph/0611671

[130] A. M. Green, "Astrophysical uncertainties on the local dark matter distribution and direct detection experiments," arXiv:1703.10102.

[131] I. R. King, "The structure of star clusters. III. Some simple dynamical models," AJ 71 (1966) 64.

[132] S. Chaudhury, P. Bhattacharjee, and R. Cowsik, "Direct detection of WIMPs : Implications of a self-consistent truncated isothermal model of the Milky Way?s dark matter halo," JCAP 1009 (2010) 020, arXiv:1006.5588.

[133] N. W. Evans, C. M. Carollo, and P. T. de Zeeuw, "Triaxial haloes and particle dark matter detection," MNRAS 318 (2000) 1131?1143, astro-ph/0008156.

[134] M. Vogelsberger, A. Helmi, V. Springel, S. D. White, J. Wang, et al., "Phase-space structure in the local dark matter distribution and its signature in direct detection experiments," Mon. Not. Roy. Astron. Soc. 395 (2009) 797, arXiv:0812.0362.

[135] J. F. Navarro, C. S. Frenk, and S. D. White, "The Structure of cold dark matter halos," Astrophys. J. 462 (1996) 563, arXiv:astro-ph/9508025.

[136] V. Springel et al., "The Aquarius Project: the subhalos of galactic halos," Mon. Not. Roy. Astron. Soc. 391 (2008) 1685, arXiv:0809.0898

[137] J. Stadel, D. Potter, B. Moore, J. Diemand, P. Madau, et al., "Quantifying the heart of darkness with GHALO - a multi-billion particle simulation of our galactic halo," Mon. Not. Roy. Astron. Soc. 398 (2009) L21, arXiv:0808.2981.

[138] J. Diemand, M. Kuhlen, P. Madau, M. Zemp, B. Moore, et al., "Clumps and streams in the local dark matter distribution," Nature 454 (2008) 735, arXiv:0805.1244.

[139] D. H. Weinberg, J. S. Bullock, F. Governato, R. K. de Naray, and A. H. G. Peter, "Cold dark matter: controversies on small scales," in Sackler Colloquium: Dark Matter Universe: On the Threshhold of Discovery Irvine, USA, October 18-20, 2012. 2013. arXiv:1306.0913.

[140] D. N. Spergel and P. J. Steinhardt, "Observational evidence for selfinteracting cold dark matter," Phys. Rev. Lett. 84 (2000) 3760, arXiv:astro-ph/9909386.

[141] J. F. Navarro, V. R. Eke, and C. S. Frenk, "The cores of dwarf galaxy halos," Mon. Not. Roy. Astron. Soc. 283 (1996) L72, arXiv:astro-ph/9610187.

[142] W. R. Leo, Techniques for Nuclear and Particle Physics Experiments. Springer-Verlag, Berlin, Heidelberg, Second revised edition, 1994.

[143] G. Heusser, "Low level counting from meteorites to neutrinos," AIP Conf. Proc. 785 (2005) 39.

[144] EDELWEISS Collaboration, E. Armengaud et al., "Background studies for the EDELWEISS dark matter experiment," Astropart. Phys. 47 (2013) 1, arXiv:1305.3628.

[145] D. Mei and A. Hime, "Muon-induced background study for underground laboratories," Phys. Rev. D73 (2006) 053004, arXiv:astro-ph/0512125.

[146] S. Westerdale and P. D. Meyers, "Radiogenic Neutron Yield Calculations for Low-Background Experiments," arXiv:1702.02465.

[147] E.-I. Esch, T. Bowles, A. Hime, A. Pichlmaier, R. Reifarth, et al., "The Cosmic ray muon flux at WIPP," Nucl. Instrum. Meth. A538 (2005) 516?525, arXiv:astro-ph/0408486.

[148] G. Waysand et al., "First characterization of the ultrashielded chamber in the low noise underground laboratory (LSBB) of Rustrel Pays d?Apt," Nucl. Instrum. Meth. A444 (2000) 336, arXiv:astro-ph/9910192.

[149] KIMS Collaboration, S.-C. Kim, "The recent results from KIMS experiment," J. Phys. Conf. Ser. 384 (2012) 012020.

[150] FREJUS Collaboration, C. Berger et al., "Experimental Study of Muon Bundles Observed in the Frejus Detector," Phys. Rev. D40 (1989) 2163.

[151] W. Yu-Cheng et al., "Measurement of cosmic ray flux in the china jinping underground laboratory," Chin. Phys. C 37 no. 8, (2013) 086001.

[152] XENON100 Collaboration, E. Aprile et al., "The XENON100 Dark Matter Experiment," Astropart. Phys. 35 (2012) 573, arXiv:1107.2155.

[153] D. Akerib et al., "Installation and commissioning of the CDMSII experiment at Soudan," Nucl. Instrum. Meth. A520 (2004) 116.

[154] LUX Collaboration, D. Akerib et al., "The Large Underground Xenon (LUX) Experiment," Nucl. Instrum. Meth. A704 (2013) 111, arXiv:1211.3788.

[155] XENON1T Collaboration, E. Aprile et al., "Conceptual design and simulation of a water Cherenkov muon veto for the XENON1T experiment," JINST 9 (2014) 11006, arXiv:1406.2374.

[156] DarkSide Collaboration, M. Bossa et al., "DarkSide-50, a background free experiment for dark matter searches," JINST 9 (2014) C01034.

[157] B. Cabrera, L. M. Krauss, and F. Wilczek, "Bolometric Detection of Neutrinos," Phys. Rev. Lett. 55 (1985) 25.

[158] BOREXINO Collaboration, G. Bellini et al., "Neutrinos from the primary protonproton fusion process in the Sun," Nature 512 no. 7515, (2014) 383.

[159] D. Z. Freedman, "Coherent neutrino nucleus scattering as a probe of the weak neutral current," Phys. Rev. D9 (1974) 1389.

[160] L. E. Strigari, "Neutrino Coherent Scattering Rates at Direct Dark Matter Detectors," New J.Phys. 11 (2009) 105011, arXiv:0903.3630

[161] A. Gutlein et al., "Solar and atmospheric neutrinos: Background sources for the direct dark matter search," Astropart. Phys. 34 (2010) 90, arXiv:1003.5530.

[162] F. Ruppin, J. Billard, E. Figueroa-Feliciano, and L. Strigari, "Complementarity of dark matter detectors in light of the neutrino background," Phys. Rev. D90 no. 8, (2014) 083510, arXiv:1408.3581.

[163] IceCube Collaboration, M. Aartsen et al., "Seasonal variation of atmospheric neutrinos in IceCube," Procc. ICRC (2013) .

[164] A. Muenster, M. v. Sivers, et al., "Radiopurity of CaWO4 crystals for direct dark matter search with CRESST and EURECA," JCAP 1405 (2014) 018, arXiv:1403.5114.

[165] F. Danevich, I. Bailiff, et al., "Effect of recrystallisation on the radioactive contamination of cawo4 crystal scintillators," Nucl. Instrum. Meth. A 631 no. 1, (2011) 44.

[166] E. Shields, J. Xu, and F. Calaprice, "SABRE: A New NaI(Tl) Dark Matter Direct Detection Experiment," Phys. Procedia 61 (2015) 169.

[167] R. Bernabei, "Crystal scintillators for low background measurements," EPJ Web Conf. 65 (2014) 01001.

[168] SuperCDMS Collaboration, R. Agnese et al., "Demonstration of Surface Electron Rejection with Interleaved Germanium Detectors for Dark Matter Searches," Appl. Phys. Lett. 103 (2013) 164105, arXiv:1305.2405.

[169] A. Broniatowski, X. Defay, et al., "A new high-background-rejection dark matter Ge cryogenic detector," Phys. Lett. B681 (2009) 305, arXiv:0905.0753

[170] CRESST Collaboration, R. Strauss et al., "A detector module with highly efficient surface-alpha event rejection operated in CRESST-II Phase 2," arXiv:1410.1753.

[171] S. Cebrian et al., "Cosmogenic activation in germanium and copper for rare event searches," Astropart. Phys. 33 (2010) 316.

[172] C. Martoff and P. Lewin, "COSMO - a program to estimate spallation radioactivity produced in a pure substance by exposure to cosmic radiation on the earth," Comput. Phys. Commun. 72 no. 1, (1992) 96.

[173] J. Back and Y. A. Ramachers, "ACTIVIA: Calculation of Isotope Production Cross-sections and Yields," Nucl. Instrum. Meth. A586 (2008) 2864, arXiv:0709.3472.

[174] J. Amar, S. Cebrin, et al., "Cosmogenic radionuclide production in NaI(Tl) crystals," JCAP 1502 no. 02, (2015) 046, arXiv:1411.0106.

[175] C.E. Alaset et al., "Design and construction of a new detector to measure ultra-low radioactive-isotope contamination of argon" (2020)

[176] DarkSide Collaboration, P. Agnes et al., "Low Radioactivity Argon Dark Matter Search Results from the DarkSide-50 Experiment," arXiv:1510.00702.

[177] D. Akerib et al., "Radiogenic and Muon-Induced Backgrounds in the LUX Dark Matter Detector," Astropart. Phys. 62 (2015) 33, arXiv:1403.1299.

[178] EXO-200 Collaboration, J. Albert et al., "Improved measurement of the $2\nu\beta\beta$ half-life of ^{136}Xe with the EXO-200 detector," Phys. Rev. C89 (2014) 015502, arXiv:1306.6106.

[179] XMASS Collaboration, K. Abe et al., "Distillation of Liquid Xenon to Remove Krypton," Astropart. Phys. 31 (2009) 290, arXiv:0809.4413.

[180] K. Abe et al. "A measurement of the scintillation decay time constant of nuclear recoilsin liquid xenon with the XMASS-I detector" (2018)

[181] Constance Walter "LUX, the end of an era" (2016)

[182] S. Lindemann and H. Simgen, "Krypton assay in xenon at the ppq level using a gas chromatographic system combined with a mass spectrometer," Eur. Phys. J. C 74 no. 2, (2014) 1, arXiv:1308.4806.

[183] E. Aprile, T. Yoon, A. Loose, L. W. Goetzke, and T. Zelevinsky, "An atom trap trace analysis for measuring krypton contamination in xenon dark matter detectors," Rev. Sci. Instrum. 84 (2013) 093105, arXiv:1305.6510.

[184] G. Zuzel and H. Simgen, "High sensitivity radon emanation measurements," Appl. Rad. Isotop. 67 (2009) 889.

[185] J. Battat et al., "Radon in the DRIFT-II directional dark matter TPC: emanation, detectionm and mitigation," JINST 9 no. 11, (2014) P11004, arXiv:1407.3938

[186] XMASS Collaboration, K. Martens, "Radon Removal from Liquid Xenon," Nucl. Phys. Proc. Suppl. 229 (2012) 562.

[187] S. Lindemann, "Intrinsic 85Kr and ^{222}Rn backgrounds in the XENON dark matter search," PhD Thesis, University of Heidelberg (Germany) (2013)

[188] S. Bruenner, D. Cichon, S. Lindemann, T. Marrodn Undagoitia, and H. Simgen, "Radon depletion in xenon boil-off gas," Eur. Phys. J. C77 no. 3, (2017) 143, arXiv:1611.03737.

[189] G. Heusser, "Low-radioactivity background techniques," Ann. Rev. Nucl. Part. Sci. 45 (1995) 543.

[190] Andrea Mancuso - "Misure di guadagno di fotomoltiplicatori per il Sistema di Veto di neutroni dell'esperimento XENONnT" - Triennal Phisics thesis, University of Bologna (2017)

[191] https://www.gransassovideogame.it/fisica/026fotomoltiplicatore.html

[192] J. Angle et al. (XENON Collaboration) "First Results form the XENON10 Dark Matter Experiment at the Gran Sasso National Laboratory", Phys. Rev. Lett. 100, 021303, (2008)

[193] E. Aprile et al. "Dark Matter Results from 100 Live Days of XENON100 Data", [arXiv:1104.2549v3], (2011)

[194] E. Aprile et al. Firts Dark Matter Search Results from the XENON1T Experiment, [arXiv:1705.06655v2], (2017)

[195] E. Aprile et al. "The XENON1T Dark Matter Experiment" (2017)

[196] E. Aprile et al. (XENON100), Astropart. Phys. 35, 573 (2012)

[197] E. Aprile et al. (XENON), JCAP 04, 027 (2016)

[198] M. Yamashita et al., Nucl. Instr. Meth. A 535, 692 (2004)

[199] www.comsol.com

[200] F. Glück et al., New J. Phys. 15, 083025 (2013)

[201] P. Barrow et al., JINST 12, P01024 (2017)

[202] L. Baudis et al., JINST 8, P04026 (2013)

[203] K. Lung et al., Nucl. Instr. Meth. A 696, 32 (2012)

[204] E. Aprile et al. (XENON1T), Eur. Phys. J C 75, 546 (2015)

[205] E. Aprile et al. (XENON100), Astropart. Phys. 54, 11 (2014)

[206] G. Kessler, PhD thesis, University of Zürich (2016) , http://dx.doi.org/10.5167/uzh-127035

[207] M. v. Sivers et al., JINST 11, P12017 (2016)

[208] E. Aprile et al. (XENON1T), arXiv:1705.01828

[209] T. Haruyama et al., AIP Conf. Proc. 823, 1695 (2006)

[210] V. Pizzella, Master thesis, Università di Roma (2016) , hdl.handle.net/11858/00-001M-0000-002B-B3FD-C

[211] E. Aprile et al., JINST 7, P10001 (2012)

[212] J.B. Albert et al. (EXO-200), Phys. Rev. C 89, 015502 (2014)

[213] E. Aprile et al. "XENONnT at LNGS" (2017)

[214] https://lz.lbl.gov/

[215] Billard, J., Strigari, L., and Figueroa-Feliciano, E. (2014) "Implication of neutrino backgrounds on the reach of next generation dark matter direct detection experiments". Phys. Rev., D89(2):023524, 1307.5458 (2014)

[216] Ade, P. A. R. et al. "Planck 2015 results. XIII. Cosmological parameters". Astron. Astrophys., 594:A13, 1502.01589 (2016)

[217] Akerib, D. S. et al. (2015). "LUX-ZEPLIN (LZ) Conceptual Design Report" 1509.02910 (2015)

[218] Akerib, D. S. et al. "Results from a search for dark matter in the complete LUX exposure". 1608.07648. (2016)

[219] Angle, J. et al. "First Results from the XENON10 Dark Matter Experiment at the Gran Sasso National Laboratory". Phys.Rev.Lett., 100:021303, 0706.0039. (2008)

[220] A. Tan et al. "Dark Matter Results from First 98.7 Days of Data from the PandaX-II Experiment". Phys. Rev. Lett., 117(12):121303, 1607.07400. (2016)

[221] X. Cui et al. "Dark Matter Results From 54-Ton-Day Exposure of PandaX-II Experiment". 1708.06917 (2017)

[222] E. Aprile et al. "Dark Matter Results from 225 Live Days of XENON100 Data". Phys. Rev. Lett., 109:181301, 1207.5988. (2012)

[223] Aprile, E. et al. The XENON100 Dark Matter Experiment. Astropart.Phys., 35:573?590, 1107.2155. (2012)

[224] E. Aprile et al. "Low-mass dark matter search using ionization signals in XENON100". Phys. Rev., D94(9):092001, 1605.06262. (2016)

[225] Aprile, E. et al. Physics reach of the XENON1T dark matter experiment. JCAP, 1604(04):027, 1512.07501. (2016)

[226] Aprile, E. et al. First Dark Matter Search Results from the XENON1T Experiment. 1705.06655. (2017)

[227] Aprile, E. et al. Online ^{222}Rn removal by cryogenic distillation in the XENON100 experiment. Eur. Phys. J., C77(6):358, 1702.06942 (2017)

[228] Aprile, E. et al. "Removing krypton from xenon by cryogenic distillation to the ppq level." Eur. Phys. J., C77(5):275, 1612.04284. (2017)

[229] Aprile, E. et al. "Signal Yields of keV Electronic Recoils and their discrimination from Nuclear Recoils in Liquid Xenon. to be published" (2017)

[230] Aprile, E. et al.1708.07051. "The XENON1T Dark Matter Experiment". (2017)

[231] J.Dobson "Overview and status of lux-zeplin. Presented at Identification" (2016) of Dark Matter 2016 (iDM2016).

[232] http://technetics.com/bin/Helicoflex.pdf.

[233] Le Port F. et al. "A magnetically driven piston pump for ultra-clean applications. Review of Scientific Instruments" (2011)

[234] Barber-Nichols, I. "The company?s webplatform" (2016) ; http://www.barber-nichols.com/

[235] Antonello et al. "Experimental observation of an extremely high electron lifetime with the icarus-t600 lar-tpc. Journal of Instrumentation" 9(12):P12006. (2014)

[236] Mihara et al. "Development of a method for liquid xenon purification using a cryogenic centrifugal pump" Cryogenics, 46(9):688 ? 693. (2006)

[237] Cennini P. et al. "Argon purification in the liquid phase. Nuclear Instruments and Methods in Physics Research" Section A: Accelerators, Spectrometers, Detectors and Associated Equipment, 333(2-3):567?570. (1993)

[238] Badertscher, A., Laffranchi, M., Meregaglia, A., Mller, A., and Rubbia, A. "First results from a liquid argon time projection chamber in a magnetic field. Nuclear Instruments and Methods in Physics Research Section A: Accelerators, Spectrometers Detectors and Associated Equipment, 555(12):294 ? 309 (2005)

[239] Curioni, A., Fleming, B. T., Jaskierny, W., Kendziora, C., Krider, J., Pordes, S., Soderberg, M. P., Spitz, J., Tope, T., and Wongjirad, T. A Regenerable Filter for Liquid Argon Purification. Nucl. Instrum. Meth., A605:306?311, 0903.2066 (2009)

[240] Bruenner, S., Cichon, D., Lindemann, S., Undagoitia, T. M., and Simgen, H. "Radon depletion in xenon boil-off gas". 1611.03737. (2016)

[241] Paper: "Conceptual design and simulation of a water Cherenkov muon veto for the XENON1T experiment" - Elena Aprile et al. (???)

[242] Hamamatsu Photonics K.K., Hamamatsu Official Site.

[243] 3M Company, 3M Official Site

[244] M. Knapp et al., The GERDA muon veto Cherenkov detector, Nucl. Instr. Meth. A 610, (2009)

[245] S. Agostinelli et al., Geant4-a simulation toolkit, Nucl. Instr. Meth. A 506, (2003)

[246] Technical note for Gd-loaded water nVeto - XENONnT Japanese nVeto WG, Shigetaka Moriyama et al. (2018)

[247] M.Iacovacci, C.Martens - ??? (2020)

[248] http://www-sk.icrr.u-tokyo.ac.jp/ nakahata-s/tokusui/talk/nakajima-JPS-2017-spring.pdf

[249] Yong Liu - Gd-Water as XenonNT nVeto alternative: simulation status (2018)

[250] A. Takeda - Implement of GGarnet (2018)

[251] Shingo Kazama - Update on nVeto study for Gd+water plan (2018)

[252] F. Agostini - Neutron Veto efficiency in geometry version 5 (2018)

[253] "Comparison of the spatial and time distribution of the nVETO Cherenkov photons between background and neutron-capture" - Presentation, University of Maintz, Daniel Wenz (2019)

[254] Andrea Mancuso - "Neutron Veto of XENONnT: final construction design of the system and extensive study and calibration of the PMTs", Phisic thesis, University of Bologna (2019)

[255] Kaito Hagiwara et al. "Gamma Ray Spectrum from Thermal Neutron Capture on Gadolinium-157". In: PTEP 2019.2 (2019), p. 023D01. doi: 10.1093/ptep/ptz002. arXiv: 1809.02664 [nucl-ex].

[256] (PRL93,171101 (2004))

[257] H. Sekiya. "Supernova neutrinos in SK-Gd and other experiments". In: Journal of Physics: Conference Series 888 (Sept. 2017), p. 012041. doi: 10.1088/1742-6596/888/1/012041.

[258] D. Ramirez. "Radiogenic Background Simulations for XENONnT". In: Poster presented at TAUP conference, Toyama, Japan.

[259] Hamamatsu Photonics K. K. Photomultiplier Tubes: Basics and Applications.

[260] "Neutron Veto PMT test report" - Presentation, XENONnT Technical meeting (2019)